Unterschrift des Betreuers

TU WIEN

TECHNISCHE
UNIVERSITÄT
WIEN
Vienna University of Technology

D I P L O M A R B E I T

Monitoring Sensitivity Parameters for Improved AUSTRAL VLBI

Ausgeführt am

Department für Geodäsie und Geoinformation

Forschungsgruppe Höhere Geodäsie

der Technischen Universität Wien

unter der Anleitung von

Prof. Dr. Johannes Böhm und Dr. Lucia Plank

und unter Mitwirkung von

Dr. Matthias Madzak

durch

Jakob Gruber, BSc

MatrNr.: 0927484

Mürzsteg 12

8693 Neuberg - Österreich

Wien, November 2015   Jakob Gruber

The Mount Pleasant Antenna in Hobart, operated by the University of Tasmania
26 meter radio telescope
directed towards the blue sky to observe stars at the edge of the universe
a very high sensitivity is required to receive these extremely weak signals

photo: Jakob Gruber, April 2015

Abstract

Within this work a detailed investigation of the sensitivity by means of the system temperature (T_{sys}) and the system equivalent flux density (SEFD) is carried out. 130 AUSTRAL VLBI sessions of the AuScope VLBI array are analyzed and a significant elevation dependency of the sensitivity is found. To account for this systematics, mapping function coefficients are estimated for each station which can be implemented in the state-of-the-art VLBI scheduling packages. An increase in both the VLBI measurement precision and in schedule performance is expected. A method is presented to examine these expectations based on the re-estimation of the SEFD. The study of the past AUSTRAL sessions shows a strong scatter of the re-estimated SEFDs. This indicates the difficulties in the prediction of VLBI scheduling parameters. Comparing the T_{sys} measurements and the SEFD reveals that the absolute magnitudes of the T_{sys} measurements must be under critical examination, due to systematics in the calibration signal. The relative variations in the T_{sys} measurements show reliable values and can be applied for real-time sensitivity determination of the AuScope VLBI antennas. Only Yarragadee shows unexpected offsets in the time series of T_{sys} measurements and must be reviewed critically. Besides the elevation systematics, a daily and yearly signal of the sensitivity are found. This correlates with the atmospheric temperature signal at the site. An impact on the position accuracy level due to unconsidered variations of the VLBI antennas sensitivity can not be found. This work provides a better understanding of the AuScope VLBI scheduling characteristics based on the elaboration of the AuScope VLBI network sensitivity parameters. Additionally a software is developed to monitor these parameters.

Kurzfassung

Die vorliegende Arbeit befasst sich mit der Sensitivität von VLBI Radio-Teleskopen, welche sich durch die Parameter, System-Temperatur (T_{sys}) und Signal Equivalent Flux Density (SEFD), beschreiben lässt. Die Auswertung und Analyse von 130 AUSTRAL VLBI Beobachtungstagen des AuScope VLBI-Netzwerkes zeigt eine signifikante Elevationsabhängigkeit der Sensitivität. Die Koeffizienten einer Projektionsfunktion, welche in den state-of-the-art VLBI-Programmen zur Erstellung von Beobachtungsplänen (Schedules) verwendet werden können, werden bestimmt um diesen systematischen Einfluss zu modellieren. Eine Verbesserung in der VLBI-Messgenauigkeit und in der Schedule-Performance wird erwartet. Eine Methode welche auf der Schätzung von den SEFDs basiert wird präsentiert um diese Vorhersage zu prüfen. Die Analyse von den AUSTRAL Daten zeigt eine starke Streuung in den geschätzten SEFDs, was die Schwierigkeit in der Prädiktion von Schedules aufzeigt. Der Vergleich von System-Temperatur und SEFD zeigt, dass die absoluten Werte der T_{sys} Messungen kritisch Beurteilt werden müssen, da Fehler in der Kalibrierung dieses Messsystems auftreten. Hingegen die relativen Änderung der System-Temperatur zuverlässige Werte liefern und damit für die Bestimmung der Sensitivität der AuScope-Antennen in Echtzeit verwenden werden können. Nur an der Station Yarragadee zeigen sich weitere Systematiken in den T_{sys}-Messungen. Weiters kann eine signifikante Temperaturabhängigkeit der Sensitivität in täglicher und jährlicher Periode gefunden werden. Ein Einfluss von unberücksichtigten Systematiken in der Sensitivität auf die Positionsgenauigkeit kann nicht gezeigt werden. Durch die in dieser Arbeit gewonnen Erkenntnisse wird ein besseres Verständnis der AuScope VLBI-Senisitivitätsparameter und deren Einfluss im Scheduling hergestellt. Zusätzlich wird eine Software entwickelt, um diese Parameter zu überwachen und zu analysieren.

Acknowledgment

Contents

List of Figures

List of Tables

List of abbreviations

BBC	Base Band Converter
CMBR	Cosmic Microwave Background Radiation
CRF	Celestial Reference Frame
CoMo	Conditioning Modules
DBBC	Digital Baseband Converter
DORIS	Doppler Orbitography and Radiopositioning Integrated by Satellite
EOP	Earth Orientation Parameter
GNSS	Global Navigation Satellite System
GUI	Graphical User Interface
IF	Intermediate Frequency
ICRF	International Celestial Reference Frame
IERS	International Earth Rotation and Reference Systems Service
IVS	International VLBI Service
LNA	Low Noise Amplifier
NGS	National Geodetic Survey
MJD	Modified Julian Date
PC	Personal Computer
RFI	Radio Frequency Interference
RMS	Root Mean Square
SEFD	System Equivalent Flux Density
SLR	Satellite Lunar Ranging
SNR	Signal to Noise Ratio
TRF	Terrestrial Reference Frame
T_{sys}	System Temperature
VGOS	VLBI Global Observing System
VLBI	Very Long Baseline Interferometry
WLAN	Wireless Local Area Network
WV	Water Vapor
URL	Uniform Resource Locator

Units

m	meter
mm	millimeter
h	hour
s	sec
ms	millisekunde
ps	picosecond
Hz	hertz
MHz	megahertz
GHz	gigahertz
W	watts
Jy	janksy
st	steradiant
K	kelvin
J	joule
A	ampere
hPa	hectopascal

1 Introduction and background

1.1 Introduction

Very Long Baseline Interferometry (VLBI) is a space geodetic technique which observes extragalactic radio sources called quasars. Precise coordinates on the Earth can be determined through the geometric relation between the baselines of a network of VLBI telescopes, their observing direction and the time delays in signal arrival between the antennas. The AuScope VLBI network consists of three new 12 m radio telescopes. An important part of the VLBI sessions performance plays the creation of schedules, where the schedule strategy, the observing direction and the on source observing time is specified. The latter strongly depends on the sensitivity of the telescopes, because the signals received are very weak in comparison to the ambient noise contribution of the atmosphere and the receiver. The increasing requirements on the station position accuracy in order to provide highly accurate reference frames, e.g., sea level rise, calls for professional research and a deeper understanding of all session performance influencing parts of VLBI, such as the creation of efficient schedules for a VLBI network. Within this work, the sensitivity of the AuScope antennas is investigated by analyzing more than 100 AuScope VLBI sessions since Dec. 2013. The influence on the creation of schedules is discussed and the impact on station position accuracy is examined.

1.2 Motivation

Originally, VLBI was developed by astronomers to determine accurate positions and spatial structures of radio sources. Nowadays, VLBI plays a very important role in geodesy as well. Geodesy can be defined as the science that determines the geometry, gravity field, and rotation of the Earth, and their evolution in time (Plag & Pearlman [2009]). Its results have made unique contributions to the study of the Earth system, its inherent dynamics, and its
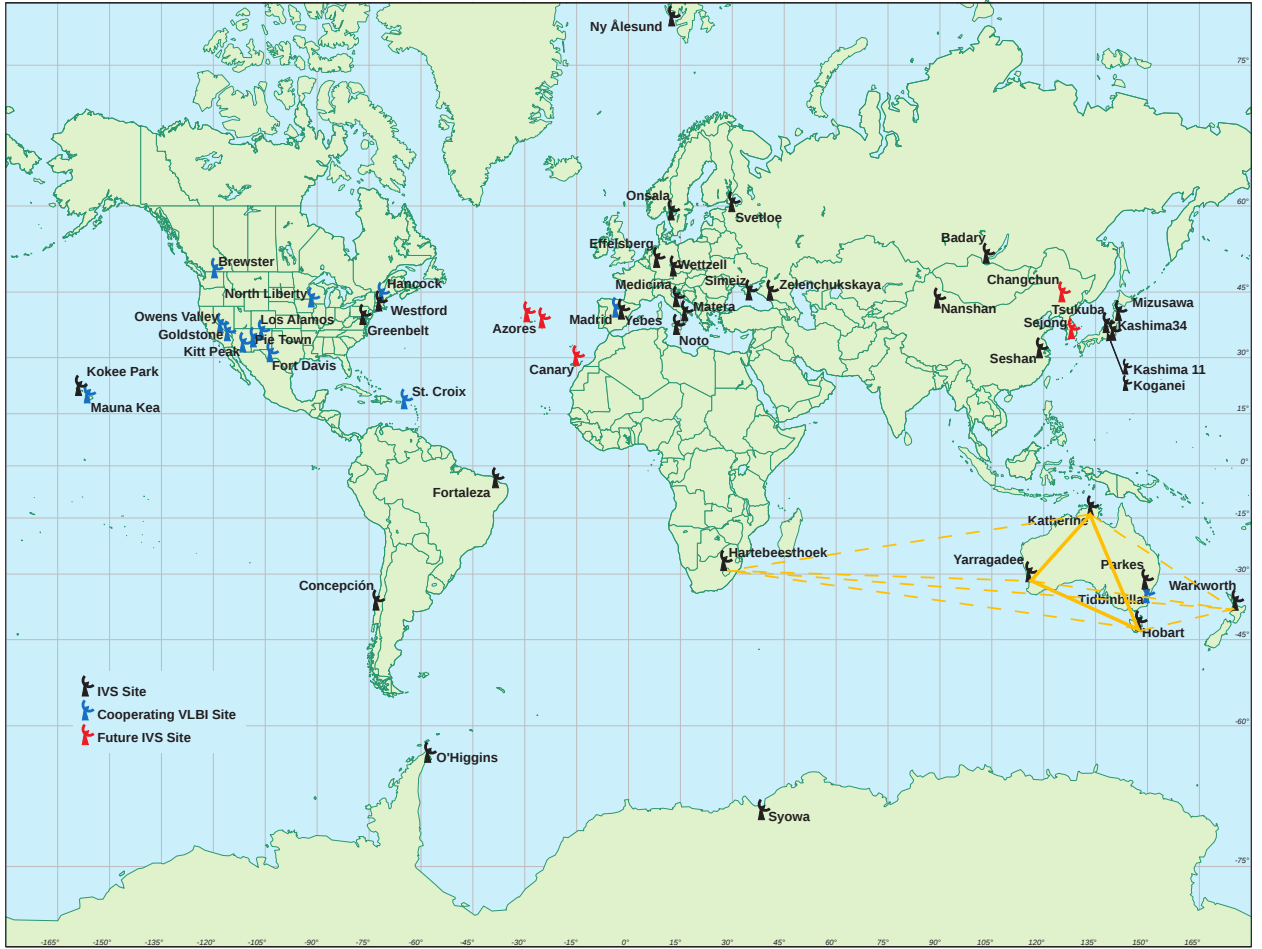
Fig. 1.1: Map of IVS VLBI sites and the AuScope network (IVS [2016]).

response to climate change. VLBI is an important part of this science and observing system. Some of the roles of VLBI in science are (Schuh, H. & Behrend, D. [2012]):

- Sea level change (Terrestrial Reference Frame TRF)

- GNSS application (orientation of the Earth in space and UT1)

- Solar system exploration (deep space tracking)

- Earth mass exchanges (orientation of the Earth in space)

- Astrometry and astrophysics (Celestial Reference Frame CRF)

In more detail, VLBI has the capability of measuring all five Earth orientation parameters (EOPs) with highest precision and is unique in its ability to obtain the nutation angles and UT1. VLBI provides an important linkage to astronomy through, for instance, the determination of very precise coordinates of extragalactic radio sources. Due to the lack

of sites in the southern hemisphere (see Fig. 1.1), the AuScope array especially plays an important role in the densification of the global VLBI network and improves significantly southern hemisphere reference frames (Plank et al. [2015]). The design of the new AuScope VLBI telescopes represents one of the VLBI2010 requirements of fast slewing antennas, to achieve the ultimate goal, on scales up to the size of the Earth, of an accuracy of 1 mm in position and of 0.1 mm/year in velocity.

1.3   VGOS requirements

To improve VLBI data in order to meet increasingly demanding requirements, investigations are being carried out within the International VLBI Service for Geodesy and Astrometry (IVS, Schlüter, W. & Behrend, D. [2007]) to design the next generation VLBI system, called VLBI Global Observing System (VGOS, formerly VLBI2010, Petrachenko et al. [2009]). The key requirements are (Niell et al. [2006]):

- 1 mm accuracy of station position on a global scale

- 0.1 mm/year accuracy of station velocity

- continuous observations of Earth Orientation Parameters (EOP) and station position time series

- geodetic results obtained within less than 24 h after observations

Strategies are carried out to achieve these challenging goals, some of them are:

- Broadband signal acquisition chain (2-14 GHz)

- Fast and small antennas

- Increasing number of antennas and improvement of their global distribution

Dynamic observing in the VGOS era will require a high level of automation and good connections between telescope, correlator, schedulers and operation centers. Furthermore, a high communication network capacity is required to allow stations to transfer data to the correlators in real time (Lovell et al. [2014]).

1.4   Terminology

In this work, the term sensitivity refers to all kind of parameters which characterize the amount of noise which is received by an antenna. In astrophysics, the noise is represented by the system temperature (T_{sys}) and by the system equivalent flux density (SEFD). Additionally, the signal to noise ratio (SNR) can be used to describe the sensitivity. In this work, the term sensitivity is used synonymously for T_{sys}, SEFD and SNR. Generally speaking, all of those parameters characterize the health of an antenna and represent a figure of merit of the whole receiving system.

This work analyses a huge amount of sensitivity observations. The expected value μ of observations x_i is estimated with $\mu = \frac{\sum x_i}{n}$. n is the number of observations. The terms average value and mean value are used synonymously for μ.

Data from the 12 m radio telescopes of Hobart, Katherine and Yarragadee will be analyzed. Their VLBI station codes are HOBART12, KATH12M and YARRA12M, respectively. In the correlation report they are specified as Hb, Ke and Yg, respectively. All of the specifiers are used synonymously to refer to the three 12 m ratio telescopes of the AuSope VLBI array.

From a historical perspective, VLBI is a type of astronomical interferometry used in radio astronomy. The fundamental relation of angular resolution θ, wavelength λ and baseline length b ($\theta = \frac{\lambda}{b}$) makes it possible to accurately resolve even stars at the edge of the universe. In this work, geodetic VLBI is considered, which uses the time delays in signal arrival between antennas to estimate baselines precisely (see Sec. 2).

1.5   Outline of the thesis

The title of this thesis is "Monitoring sensitivity parameters for improved AUSTRAL VLBI". Sensitivity parameters tell us something about the ability of a VLBI receiving system to separate the highly unwanted noise from the very weak signals of the quasars we are actually interested in. The theory of this ability is discussed in Sec. 3, where we will obtain two parameters which are optimal to describe the amount of disturbing noise and perfectly characterize the sensitivity of VLBI receivers. The parameters are called: System Temperature (T_{sys}) and System Equivalent Flux Density (SEFD). Before that the fundamental VLBI principle and the important relation between sensitivity and VLBI measurement precision is presented in Sec. 2. This is actually the first link between the sensitivity and the VLBI performance.

The studies in this work are based on the data of the AUSTRAL VLBI program which is described in Sec. 4. This data is used to monitor the sensitivity parameters. First a detail investigation of the T_{sys} is carried out, where we find significant atmospheric contributions and unexpected receiver impacts (Sec. 5.4 & Sec. 5.5). A software is developed to monitor this sensitivity parameter and to estimate station specific quality parameters (Sec. 5.1.3). Second the SEFD of the AUSTRAL VLBI programm is investigated in Sec. 6. In this section a new approach is presented which enables the estimation of the SEFD on a reliable basis. Additionally this method is implemented to monitor this sensitivity parameter (see Sec. 6.1.1). Finally this chapter compares the SEFD and the T_{sys} (Sec. 6.3), discusses their advantages and disadvantages and confronts their characteristics and capabilities (Sec. 6.4). The main result of this work is presented in the next section (sec. 7). It shows the impact of the sensitivity in the creation of VLBI schedules, which is the second link between sensitivity and VLBI session performance. In section 8 the impact of the sensitivity on the final geodetic products are investigated. Section 9 concludes the entire work and shows future work and perspectives.

2 VLBI fundamentals

The time delays in signal arrival between antennas is the fundamental measurement of geodetic VLBI. Eq. 2.1 represents the straight forward geometric relation between the baseline b, the delay τ_g and the direction of the unit vector s_0 to the radio source (Schuh, H. & Behrend, D. [2012]) and is visualized in Fig. 2.1.
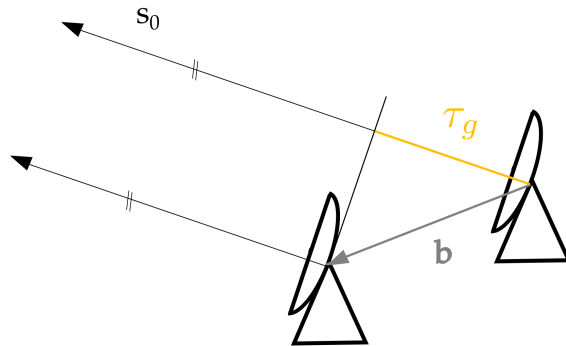
Fig. 2.1: A sketch of the principle of VLBI.

$$\tau_g = -\frac{b\,s_0}{c} \tag{2.1}$$

with c . . . speed of light $[\text{ms}^{-1}]$

In order to account for nuisance terms, which corrupt τ_g, Eq. 2.1 has to be refined by adding correction terms. This yields the fundamental observation equation for VLBI (Eq. 2.2,

Cannon [1999]).

$$\tau = \tau_g + \tau_{ab} + \tau_{clk} + \tau_{inst} + \tau_{trop} + \tau_{iono} + \tau_{rel} \tag{2.2}$$

with τ_g . . . geometric delay
              τ_{ab} . . . contribution due to diurnal abberation
              τ_{clk} . . . delay due to missynchronization of the reference clocks at each site
              τ_{inst} . . . delay due to propagation through receiver system
              τ_{trop} . . . contribution of the troposphere
              τ_{iono} . . . contribution of the ionosphere
              τ_{rel} . . . special and general relativistc correction

The measurement error σ_τ is determined with Eq. 2.3. This relation shows that the measurement error depends on the effective bandwidth B_{eff} and on the required SNR. The higher B_{eff}, the lower (better) is the measurement error. In the same way a higher SNR improves the measurement precision. Eq. 2.3 is fundamental in VLBI, because it relates the measurement precision with the SNR and B_{eff}. This means that we have to choose the SNR and B_{eff} appropriately to obtain the required measurement precision. The SNR plays an important role in this work, because it characterizes sensitivity.

$$\sigma_\tau = \frac{1}{2\pi} \frac{1}{\text{SNR } B_{eff}} \tag{2.3}$$

with B_{eff} . . . effective bandwidth $[\text{s}^{-1}]$
            SNR   . . . required signal to noise ratio

3 Theory of the system temperature and the system equivalent flux density

There is a temperature proportional to the power received of the antenna (Sec. 3.1). The power received is the sum of the power received of the quasar and a variety of sources of noise. The power load of all these components is the system temperature (Sec. 3.2). The flux equivalent is the system equivalent flux density (SEFD). The SEFD plays an important role in the estimation of the scan length and therefore it represents an important quantity in the creation of schedules in the VLBI (Sec. 3.4).

3.1 Some basic definitions

In this section, basic physical quantities are defined in order to provide a description of the system temperature (T_{sys}) and system equivalent flux density (SEFD). The following deviations are based on Wilson et al. [2009].

An antenna is a device for converting electromagnetic radiation in space into electric power in conductors. Considering an observation over the total solid angle subtended by the source, the received electrical power depends on the area of the radiation intercepting surface and on the observed bandwidth. By using Eq. 3.1 we get the flux density.

$$S = \frac{dP}{dA \, df} \tag{3.1}$$

with dP ... infinitesimal power in watts [W]
            dA ... infinitesimal area of surface [m^{-2}]
            df ... infinitesimal bandwidth in hertz [Hz]
            S_f ... flux density [W m^{-2} Hz^{-1}]

This parameter is independent of the area of the antenna and the bandwidth and it is used to describe the strength of radio sources in the realization of the international celestial reference frame (ICRF2, Ma et al. [2009]). Since the flux density of radio sources is usually very small, a special radio astronomical flux density unit, the Jansky (abbreviated Jy) has been introduced (see Eq. 3.2).

$$1 \text{ Jy} = 10^{-26} \text{ W m}^{-2} \text{ Hz}^{-1} \tag{3.2}$$

To refine the description of the received electrical power, the solid angle is considered.

$$I = \frac{dP}{dA \, df \, d\Omega} \tag{3.3}$$

with $d\Omega$ ... infinitesimal solid angle [st]
            I ... specific intensity [W m^{-2} Hz^{-1} st^{-1}]

Eq. 3.3 yields the specific intensity. If there is complete equilibrium of the radiation with its surroundings, specific intensity is equal to the brightness distribution described by the Planck function (Eq. 3.4), which depends only on the thermodynamic temperature. It is the temperature needed to produce the observed specific intensity.

$$I_f = \frac{2\ h\ f^3}{c^2}\ \frac{1}{e^{hf/kT} - 1} \tag{3.4}$$

with T ...temperature [K]
         h ...Planck constant = 6.63 10^{-34} [J s]
         k ...Boltzmann constant = 1.38 10^{-23} [J K^{-1}]
         f ...frequency [Hz]
         c ...velocity of light = 3 10^8 [ms^{-1}]

Using the Rayleigh-Jeans law for $hf/kT << 1$, Eq. 3.4 simplifies to

$$I_f = \frac{2\ f^2}{c^2}\ k\ T \tag{3.5}$$

Combining (Eq. 3.3) with (Eq. 3.5) and using the relation $dAd\Omega = \lambda^2$, known as the antenna theorem (Marr J. M. [2015]), we have

$$P_f = 2\ k\ T \tag{3.6}$$

Equation (3.6) shows the important relation of the temperature of the source and of the power received for a certain frequency.

3.2   System temperature

Radio astronomers find it convenient to refer to the power of various signals from radio telescope in terms of the proportional temperature (Eq. 3.6) (Crane & Napier [1988]). They pretend that the sources observed are thermal in nature (even though they usually are not!). Due to the fact that all matter radiates electromagnetic energy, not only radiation of the quasar is received. A breakdown of system noise components is shown in table 3.1. Eq. 3.7 shows the power received from radiation covered by the receiving pattern (RP) of the antenna. The corresponding temperature is also referred to as the antenna temperature T_A. Additionally the input of the electromagnetic radiation of the receiver system itself is received (T_{rec}). The temperature proportional to the total power received is called system temperature (T_{sys}), a figure of merit of the whole receiving system (Eq. 3.8).

$$T_A = \frac{1}{2\,k}\ \int_{\text{RP}} P_f(\theta, \phi)\, d\theta\, d\phi \tag{3.7}$$

$$T_{sys} = T_A + T_{rec} \tag{3.8}$$

Source of noise	[K]	major dependencies
Cosmic microwave background	3	
Milky Way Galaxy	0-1	frequency, direction
Ionosphere	0-1	time, frequency, elevation
Troposphere	3-30	elevation, weather
Antenna radome	0-10	
Antenna	0-5	
Ground spillover	0-30	elevation
Feed	5-30	
Cryogenic LNA	5-20	
Total	16-130	

Tab. 3.1: Sources of noise producing system temperature, Petrachenko [2013]

The famous cosmic microwave background radiation (CMBR) is an emission of uniform, black body thermal energy coming from all parts of the sky and is about 3 K (Penzias & Wilson [1965]). The radiation of the milky way galaxy (0-1 K) comes from a region surrounding the milky way's core, therefore depending on the observing direction. In the same range of magnitude lies the radiation of the ionosphere, but depending on temporal variations (seasonal variations, solar flares, etc.). The radiation of the troposphere is strongly dependent on elevation and weather. Observations at low elevations yield higher temperatures (Fig. 3.1), because of the increasing thickness of the troposphere at lower elevations. At very low elevation ($<10°$) ground spillover is noticed, where the side-lobes of the receiving pattern is directed downwards to the warm Earth (Fig. 3.2). It is the power from the feed, which is not intercepted by the reflecting elements. The effect of antenna radomes have to be considered if installed (not the case for AuScope antennas). The main component is the T_{rec}, which is made up of the feed, the linear noise amplifier (LNA) and the other components in the front end receiver section (antenna).

A 1 Jy source (typical for AUSTRAL sessions) observed by a 12 m antenna with 75% efficiency will produce an antenna temperature of 0.03 K. Using a typical system noise
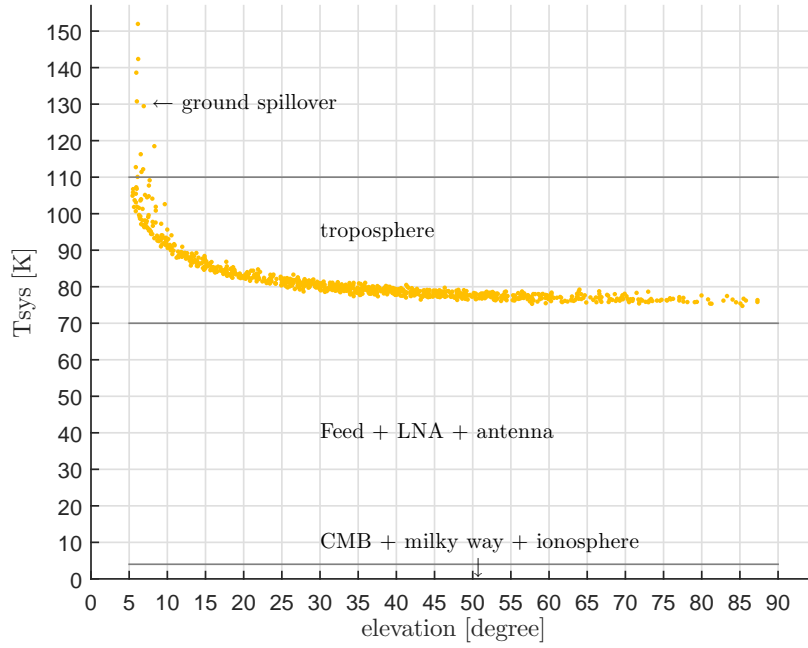
Fig. 3.1: System temperature measured per scan (orange dots) sorted by elevation of session 1516 in Hobart. In gray an assumed distribution of the noise components. CMB, milky way and ionosphere contribute with 4 K. Feed, LNA and the antenna contribute with 66 K. In zenith-direction the troposphere contributes with 5 K and up to 40 K at an elevation of 5°. The effect of ground spillover can be found at elevations lower than 10°.
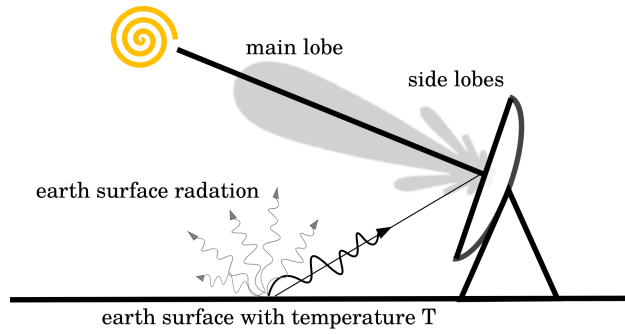
Fig. 3.2: In practice, the receiving pattern of an antenna is not a straight line. Of course, the main lobe is directed to the source of interest, but side lobes are formed as well. At low elevation <10°, that is present for geodetic experiments, the radiation of the warm Earth is received and contributes to the T_{sys}.

around 80 K (Fig. 3.1) yields a signal to noise ratio of $3 \cdot 10^{-4}$. To use this very weak signal, one has to stay (observe) on the source for a certain time (Sec. 3.4). This very weak signal can be resolved by the concept of VLBI.

3.2.1 Atmospheric contribution to the system temperature

The atmosphere is known to be transparent for frequencies in the radio region (Fig. 3.3a), also known as the radio window. However, the atmosphere attenuates and even emits radiation in the radio region and therefore contributes significantly to the T_{sys} (Tab. 3.1). The concept behind this process is described by the radiative-transfer equation (Chandrasekhar [1960]). If the radiation traverses the atmosphere and the intensity is reduced, we have extinction, and if the medium adds energy of its own, we have emission. For simplicity the atmosphere is considered to be a homogeneous layer of depth d, temperature t_{atm} and emissivity ϵ. ϵ is the ratio of the radiation of the atmosphere and the radiation of a black body (Eq. 3.5) at the same temperature as the atmosphere. With Eq. 3.9 the optical depth τ is introduced and can be used to describe the noise contribution of and the attenuation due to the atmosphere (Eq. 3.10).

$$\tau = \epsilon\, d \tag{3.9}$$

$$T_A = T_{cosmic}\, e^{-\tau} + t_{atm}\, (1 - e^{-\tau}) \tag{3.10}$$

The signal which penetrates the atmosphere (includes the signal of the quasar and other cosmic radiation) is attenuated with $e^{-\tau}$, but also radiation is added with $(1 - e^{-\tau})$. In other words, the signal we are interested in is attenuated and the unwanted noise received is amplified. The sensitivity in terms of the SNR of ground based radio observations is therefore degraded. Both processes are occurring simultaneously, the higher the attenuation (e.g. due to absorption) the more energy the atmosphere consists of, hence the higher is the emitted radiation). The level of attenuation and emission, respectively, is controlled by the consistence of atmosphere such as water vapor (WV) content (Fig. 3.3b) and the depth of the layer (d). To be more correct, it is the slant-path determined by the elevation angle of the radio antenna. The lower the elevation, the longer is the slant path. The noise contribution due to the atmosphere depends on signal path length in the atmosphere, which is a function of elevation. If the atmosphere is assumed to be a straight single layer, d has to be multiplied by $\frac{1}{sin(elev)}$. Due to linearity the atmospheric noise contribution is $t_{atm}\, (1 - e^{-\tau\ sin^{-1}(elev)})$. All the atmospheric components are driven by time dependent variation such as temperature changes between night and day and seasonal variations. Rainfalls highly influence the emissivity of the atmosphere (Feldman [1964]).
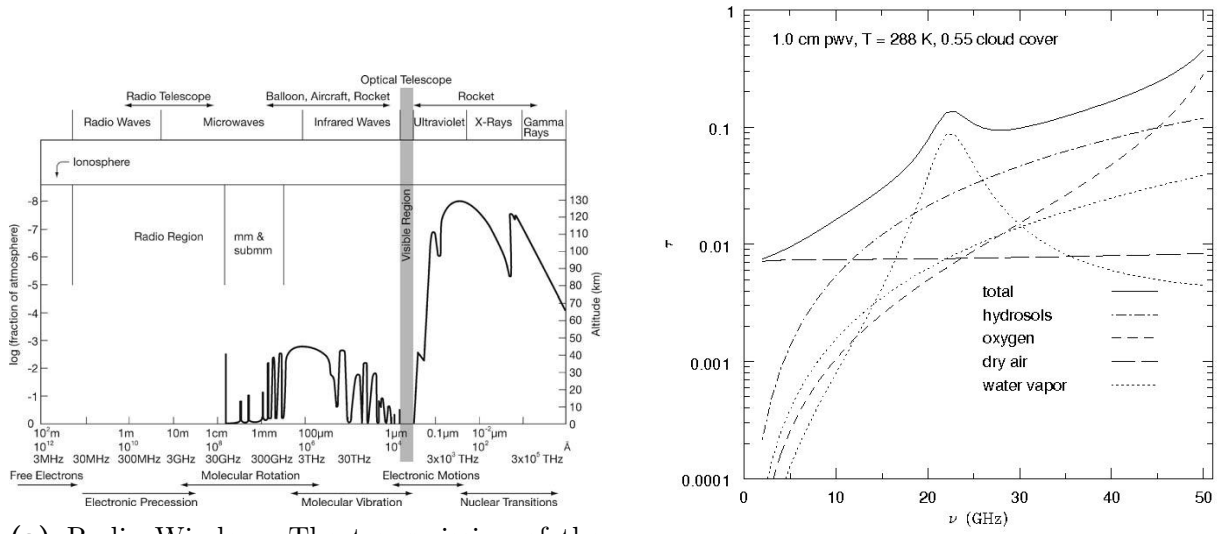
(a) Radio Window: The transmission of the Earth's atmosphere for electromagnetic radiation. Wilson et al. [2009]

(b) Zenith opacity versus frequency for a typical summer day in Green Bank, WV with precipitable water vapor (PWV) of 1.0 cm, a surface air temperature of 288 K, and 55% cloud cover (Balser et al. [2009]).

Fig. 3.3: Electromagnetic radiation in the radio region can transmit the atmosphere but is attenuated.

3.2.2 Receiver noise

Eq. 3.6 shows the relation between the temperature of the source and the power received. Another important relation is Eq. 3.11, which shows the relation between the power received due to the input of the receiver itself. Fig. 3.4 demonstrates this random input. It's an electrical noise by means of principles in thermodynamics and statistical mechanics (Nyquist H. [1928]), called Johnson–Nyquist noise and is produced by the random movement of electrons in any conductor with a temperature above absolute zero. The mean value of this current i will be zero. Since 3.11 represents a power (Wilson et al. [2009]), a random signal produces a nonzero power input (3.4).

$$P_f = \frac{1}{\tau} \int_\tau i^2(t) \, dt \qquad (3.11)$$

with i ... current [A]

        τ ... total integration time [s]
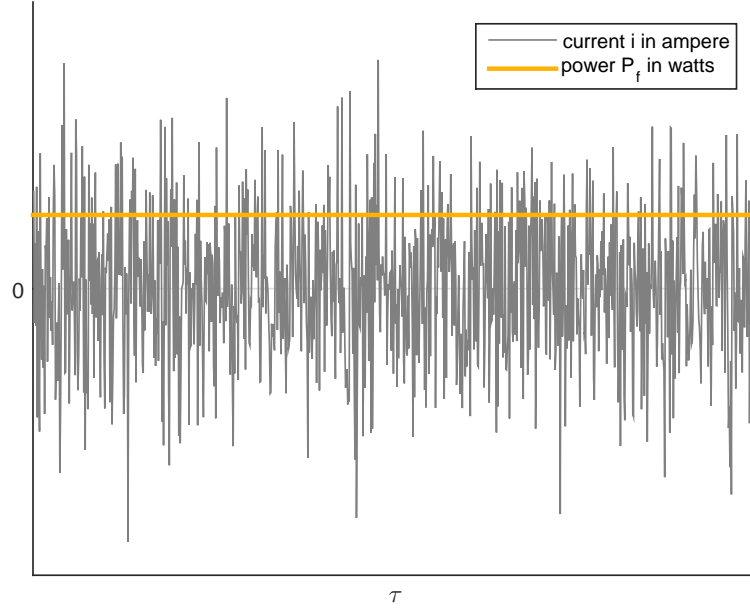
Fig. 3.4: Relation of current (Johnson–Nyquist noise, Nyquist H. [1928]) and power

3.3 System equivalent flux density (SEFD)

The sensitivity of a VLBI receiver is generally characterized by the system equivalent flux density (SEFD), an overall measurement of the antenna performance (Taylor et al. [1999]). This is basically the flux equivalent of the T_{sys}. The higher T_{sys}, the higher is the load of the power of the noise sources. In the same way the sensitivity is worse at higher SEFD values. Eq. 3.13 to 3.15 show the derivation of the SEFD. Because the T_{sys} depends on the area of the antenna, the flux density concept (Eq. 3.1) is used to obtain a parameter that is independent of the antenna characteristics, Eq. (3.13).

$$S_f = \frac{dP}{dA} = \frac{2\ k\ T}{A} \tag{3.12}$$

By use of the T_{sys} we yield the SEFD (Eq. 3.13).

$$S_{f,tsys} = \text{SEFD} = \frac{2\ k\ T_{sys}}{A} \tag{3.13}$$

Introducing the aperture efficiency η, we distinguish between the geometric and the effective collecting area.

15

$$A_{eff} = \eta \ A_{geo} \tag{3.14}$$

with A_{eff} . . . effective collecting area [m^2]
        A_{eff} . . . geometric area [m^2]

Eq. 3.13 becomes Eq. 3.15.

$$\text{SEFD} = \frac{2 \ k \ T_{sys}}{A_{eff}} \tag{3.15}$$

The SEFD is a useful way to compare the sensitivity of two different systems, since it folds in both the T_{sys} and the A_{eff}.

3.4   Scan length

The source strength of quasars used in VLBI depend on the experiment type, but can vary from several hundred mJy up to several Jy. The signal to noise ratio (SNR) is defined as the ratio of signal power to the noise power. In terms of flux densities, following Sun [2012] and Gipson [2012], the SNR is estimated in Eq. 3.16.

$$\text{SNR} = \frac{S_{f,quasar}}{\sqrt{SEFD_1 \ SEFD_2}} \ \frac{\sqrt{2 \ B \ N_{ch} \ scanlength}}{1.75} \tag{3.16}$$

with $S_{f,quasar}$ . . . flux density observed of the quasar [Jy]
        $SEFD_{1,2}$ . . . SEFD of antenna 1 and 2 [Jy]
        B . . . bandwidth [Hz]
        N_{ch} . . . number of channels [ ]
        1.75   . . . correction factor [ ]

Eq. 3.16 can be inverted to yield the scan length. The fundamental equation (3.17) is used in scheduling of VLBI sessions (Sun [2012] and Gipson [2012]). The scan length is the on source observing time to meet the minimum SNR (SNR$_{\text{min}}$) targets.

$$scanlength = (\frac{1.75 \ SNR_{min}}{S_{f,quasar}})^2 \ \frac{SEFD_1 \ SEFD_2}{2 \ B \ N_{ch}} \tag{3.17}$$

4 AuScope array and AUSTRAL sessions

4.1 The AuScope VLBI array

Fig. 4.1: The AuScope VLBI sites (Lovell [2015]).

The Australian AuScope VLBI array consists of three antennas, located in Hobart, Katherine and Yarragadee (Fig. 4.1 & 4.2). The array is operated by AuScope, which is the national provider of integrated research infrastructure of Australian Earth and geospatial science researchers (AuScope [2007]). An important part of AuScope tasks is the AuScope VLBI Project, which includes the acquisition and maintenance of the three radio telescopes and a data processing facility for geodesy. It is this array that ties Australian geodesy into the International Geospatial Reference Frame which is tied to the International Celestial Reference Frame.

Fig. 4.2b show the lateral distribution of the VLBI stations (orange dots), which are part of IVS sessions. Only 25% of the stations are located on the southern hemisphere of the Earth. The AuScope VLBI antennas are part of these stations and provide an increased number of observations to quasars in the south and improve significantly southern hemisphere reference frames (Plank et al. [2015]).
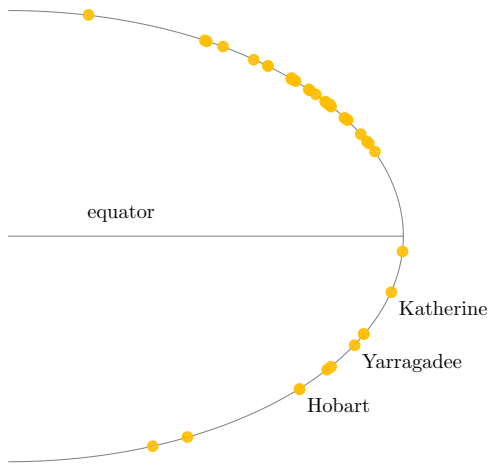
(a) Lateral distribution of IVS VLBI stations
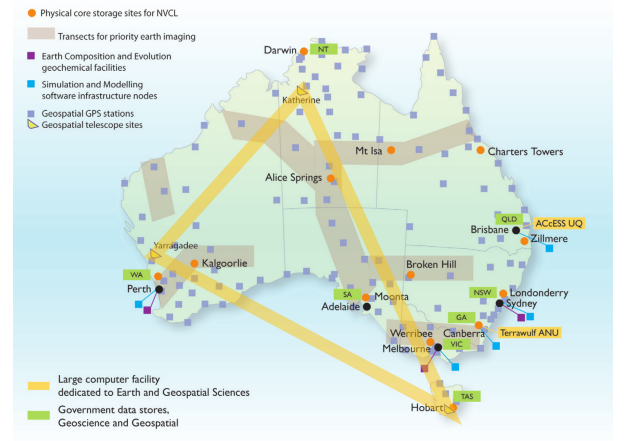
(b) Of course, the AuScope VLBI antennas are located in Australia. The baselines (orange lines) are of similar distance and form a triangle which covers the Australian state.

Fig. 4.2: Location of the AuScope VLBI array

The array is being operated for AuScope by the University of Tasmania in coordination with the International VLBI Service (IVS) with some data correlation supported by Curtin University of Technology. The VLBI telescopes are co-located with other space geodetic techniques including GNSS, gravity, and in the case of Yarragadee, SLR and DORIS facilities.

4.2   AUSTRAL sessions

The AUSTRAL network consists of the AuScope array, the Hartebeesthoek 15 m and the Warkworth 12 m telescope. In this work AUSTRAL sessions are analyzed, but only the AuScope network is included in the sensitivity analysis. The AUSTRAL observing program is divided into three streams focussed on high priority geodetic and astrometric aims in the southern hemisphere (Lovell et al. [2014]). Table 4.1 lists the session code and the scientific aim of the AUSTRAL sessions, which are used in this work.

experiment name	description
a1305 - a1315	CONT-like campaign in 2013
a1401 - a1415	CONT-like campaign in 2014
a1501 - a1515	CONT-like campaign in 2015
a1516 - a1522	CONT-like campaign in 2015
aug001 - aug019	Geodesy (baselines, station coordinates)
aust18 - aust74	Geodesy (baselines, station coordinates)
aua001 - aua008	Astronomy

Tab. 4.1: AUSTRAL experiments

CONT-like-campaigns are not exactly continuous because there are sessions in between (like R1/R4 sessions), but they are very timely and a identical schedule is used, therefore they are referred to as CONT-like-campaigns. The time series of the AUSTRAL sessions are shown in Fig. 4.3.
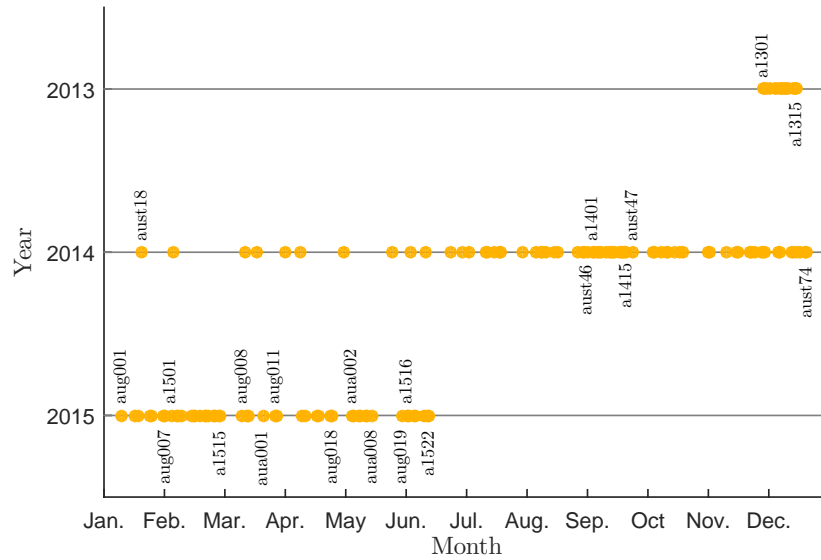
Fig. 4.3: AUSTRAL data overview

4.3 Used sky frequencies

The AUSTRAL experiments operate with 14 channels. Each channel refers to a section of a narrow bandpass (16 MHz). Figure 4.4 shows the used upper and lower sidebands of the sky frequency for each channel. The lower sideband is used only for channel number 1 and 8 (except for early AUSTRAL sessions). By use of the definition of the Institute for

19

(a) X-band   **(b)** S-band
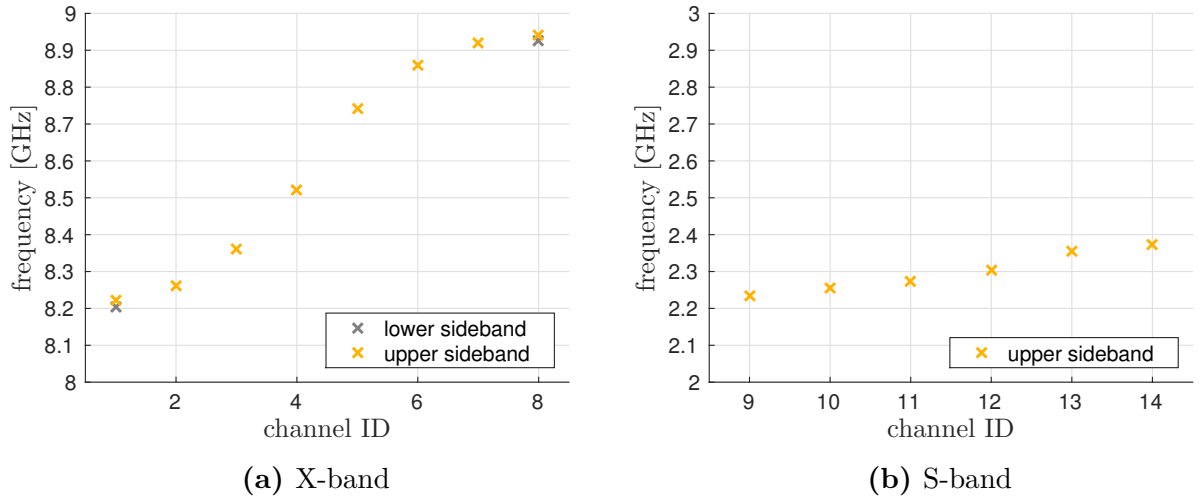
Fig. 4.4: AUSTRAL sky frequencies of each channel

Electrical and Electronic Engineers [1984] (IEEE), the channel numbers 1 to 8 refer to the X-band and the channel numbers 9 to 14 to the S-band. This means that ten observations (eight upper sidebands plus two lower side bands) cover the X-band and six observations (six upper side bands) cover the S-band. The S-band is only used as an "auxiliary" band to correct the X–band ionospheric delay. Porcas, R. [2010] quantified the contribution of the X-band to the final VLBI delay with $\frac{12}{13}$ and the contribution of the S-band with $\frac{1}{13}$, respectively.

X-band [MHz]	S-band [MHz]
8204.99	2156.00
8220.99	2233.99
8260.99	2253.99
8360.99	2273.99
8520.99	2303.99
8740.99	2353.99
8860.99	2373.99
8880.00	
8920.99	
8924.99	
8940.99	

Tab. 4.2: AUSTRAL sky frequencies for X- and S-band channels.

Widely spaced frequency bands between 2-14 GHz represent an important requirement of

VLBI2010. It is referred to as the broadband delay concept. A method that uses several widely spaced frequency bands to resolve the interferometer phase delay (Petrachenko [2009]). Lovell et al. [2013] pointed out that this is the most important upgrade required to the AuScope VLBI array, which is currently in the S/X VLBI system (legacy system).

5 The system temperature of the AUSTRAL VLBI sessions
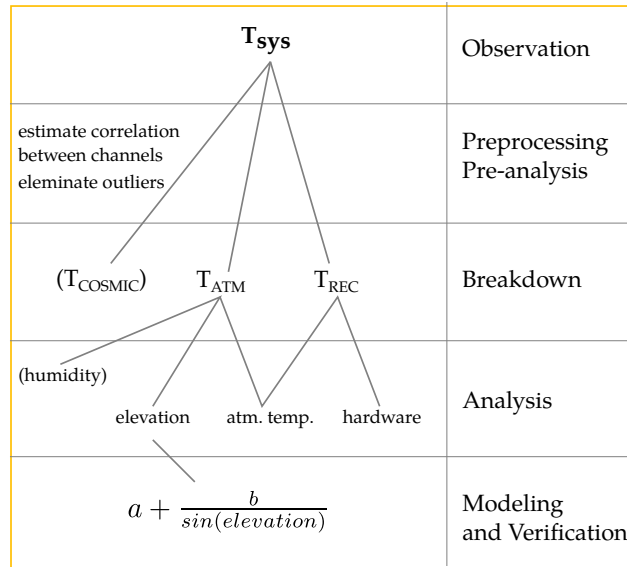
Fig. 5.1: Flowchart of the analysis of the system temperature of the AuScope array

In VLBI not only one delay is observed per scan. The delay observation is realized for each of the used sky frequencies (Sec. 4.3). Each sky frequency refers to a single channel and the system temperature (T_{sys}) of the AuScope array is measured at each site in all used sky frequencies (Sec. 4.3), channels respectively. This means the sensitivity information is obtained for each of the 14 channels for each of the three stations per scan (several hundreds) of all 130 sessions. This represents a huge amount of data. In order to appropriately analyze the T_{sys} of the AuScope array, a process strategy is set up, which can be seen in Fig. 5.1. First, the measured T_{sys} is preprocessed by eliminating outliers (Sec. 5.3). The correlation between the channels is estimated to start a pre-analysis. In this work, the T_{sys} is assumed to be a sum

of the cosmic noise sources (T_{COSMIC}), the atmospheric noise sources (T_{ATM}) and the receiver noise (T_{REC}). The cosmic component is neglected because the impact is very stable in time, whereas the atmospheric contribution of noise (Sec. 5.4) is strongly elevation dependent. This systematic will be modeled. In theory the humidity of the atmosphere influences the noise load, but it is not considered in this work. The atmospheric temperature plays an important role, because it is the driver of the radiation of the atmosphere, which finally leads to additional noise. Variations in the atmospheric temperature also heat and cool the receiver, which represents a further source of noise. This and other hardware components influence the T_{sys} as well and are discussed in Sec. 5.5.

5.1 Measuring and extracting the system temperature

In order to understand the magnitudes of the measured T_{sys} of the stations of the AuScope array, the way of measuring T_{sys} has to be clarified. This is done in detail in Sec. 5.1.1. Furthermore the way of how the T_{sys} measurements are stored in the log-files is shown (Sec. 5.1.2). Additionally, within this work a software is developed to analyze the measured T_{sys} (Sec. 5.1.3).

5.1.1 Measuring system temperature

The receiver allows an injection of calibration signals from noise diodes ahead of the low noise amplifier (LNA), which is a way of measuring T_{sys} (Fig. 5.1). Operationally, the T_{sys} is determined by measuring the power on (P_{on}) and off (P_{off}) a source with a calibrated system temperature T_{cal} (Eq. 5.1). The relation between T_{cal} and T_{sys} using the fraction of P_{on} and P_{off} is possible due to the direct proportionality of temperature and power (Eq. 3.6).
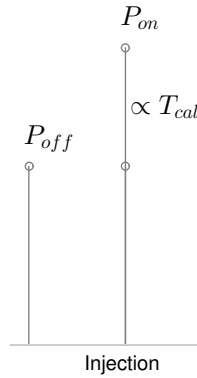
Fig. 5.2: The injection of the calibration signal T_{cal} increases the power measured. P_{off} is the power measured before the injection happens. It is the power of the default noise level. The fraction of P_{on} and P_{off} is proportional to the calibration signal T_{cal}.

$$T_{cal} = T_{sys} \, \frac{P_{on}}{P_{off}} - T_{sys} \quad , \qquad T_{sys} = \frac{T_{cal}}{\frac{P_{on}}{P_{off}} - 1} \tag{5.1}$$

In more detail, it is achieved by modulating a noise diode via a 80 Hz square-wave (non-sinusoidal periodic waveform) signal from the digital baseband converter (DBBC). The DBBC detects the return signal, demodulates it, and uses the on/off values (Eq. 5.1) to determine the T_{sys} (Lovell [2015]).

Even if the true value of the T_{cal} is unknown, the calculated T_{sys} values are useful as measures of the relative changes in sensitivity. It is important to note, that following conditions must be fulfilled to obtain reliable T_{sys} measurements (Petrachenko [2013]):

- T_{cal} must be stable (may require physical temperature control).

- The system gain ahead of the injection point must be stable.

5.1.2 Extracting system temperature

T_{sys} is measured per station and per scan and stored into PC field system log files, which are created for each session. They are kept on ops-serv2 in the directory /vlbobs/ivs/logs and the log file names follow the nomenclature $< experiment - name >< station - code >$.log. So the Hobart 12 m log for AUG014 is called aug014hb.log. Each line of the log file starts with a time code (year.day.hh:mm:ss.ss). The T_{sys} values are all logged with the string "$/tsys/$" after the time code and each T_{sys} record is 4 lines long. So, for example, the last T_{sys} log in aug014hb.log is:

```
2015.102.23:58:50.09/tsys/1l,91.1,1u,94.6,2u,110.4,3u,79.8,4u,83.8,ia,106.5
2015.102.23:58:50.09/tsys/5u,104.9,6u,80.5,7u,105.5,8l,106.9,8u,97.2,ib,63.5
2015.102.23:58:50.09/tsys/9u,113.9,au,109.3,bu,110.9,cu,134.5,ic,60.2
2015.102.23:58:50.09/tsys/du,238.6,eu,-38.0,id,19.4
```

Each T_{sys} entry is in a pair, where the first item is the channel ID and the second number is the T_{sys}. In the example above, channel "1l" had a T_{sys} of 91.1 K, channel "1u" was 94.6 K, etc.

The channel IDs refer to the section of bandpass that the T_{sys} was measured. To decode these, following has to be considered. The DBBC has 4 inputs (or Conditioning Modules,

or "CoMo"s) labeled A, B, C and D. Usually the down-converted X-band signal goes into A and B, and S-band into C and D. The CoMos send these on for filtering and digitization. If you search the log for "/bbc" you'll see that 14 frequencies are set, 4 each from CoMos A, B and C, and two from CoMo D:

```
2015.102.23:59:01.65/bbc01/ 612.990000,a,16, 1,agc, 42, 41,16261,15872
2015.102.23:59:01.65/bbc02/ 652.990000,a,16, 1,agc, 42, 43,15806,16345
2015.102.23:59:01.65/bbc03/ 752.990000,a,16, 1,agc, 65, 64,15875,15981
2015.102.23:59:01.65/bbc04/ 912.990000,a,16, 1,agc, 59, 54,16023,15922
2015.102.23:59:01.65/bbc05/1132.990000,b,16, 1,agc, 37, 36,15124,15347
2015.102.23:59:01.66/bbc06/1252.990000,b,16, 1,agc, 42, 45,15836,15933
2015.102.23:59:01.66/bbc07/1312.990000,b,16, 1,agc, 53, 45,15185,15179
2015.102.23:59:01.66/bbc08/1332.990000,b,16, 1,agc, 53, 54,15215,15262
2015.102.23:59:01.66/bbc09/ 325.990000,c,16, 1,agc, 34, 36,14331,14687
2015.102.23:59:01.66/bbc10/ 345.990000,c,16, 1,agc, 38, 35,14418,14431
2015.102.23:59:01.66/bbc11/ 365.990000,c,16, 1,agc, 39, 39,14477,14744
2015.102.23:59:01.66/bbc12/ 395.990000,c,16, 1,agc, 38, 38,14722,14189
2015.102.23:59:01.66/bbc13/ 445.990000,d,16, 1,agc, 66, 65,19846,17544
2015.102.23:59:01.66/bbc14/ 465.990000,d,16, 1,agc, 50, 52,12860,15026
```

In the above case bbc01 is set to 612.99 MHz, from CoMo A, and 16 MHz of bandwidth. Our first LO frequencies are 7600 MHz for X-band and 1900 MHz for S-band. Adding these to the above results in the actual observed frequencies. So bbc01 is actually a sky frequency of 7600+612.99 = 8212.99 MHz and bbc09 is 1900+325.99 = 2225.99 MHz.

The Channel IDs in the T_{sys} log entries refer to the BBC number and whether it's upper or lower sideband. So "1l" means BBC01, lower sideband (i.e. frequency range from (8212.99-16) to 8212.99 MHz, "5u" means BBC05, upper sideband, or 8732.99 to (8732.99 +16)=8748.99 MHz. In the T_{sys} entries, channel numbers (01 to 14) are labeled (0, 1, 2, 3, ..., 9, a, b, c, d, e).

5.1.3 Monitoring system temperature measurements

Sec. 5.1.2 shows the complex way how the T_{sys} values are stored in the log files. Within this work a MATLAB routine is developed to extract all necessary information from the log files. Each T_{sys} value is measured and stored per scan. This routine extracts each T_{sys} measurement and the following corresponding parameters, which are measured per scan as

well:

- scan name (e.g. 247-0436)

- source name (e.g. 0637-752)

- channel number + lower or upper sideband (e.g. 1l)

- temperature, pressure, relative humidity (e.g. 14.4 C°,1012.0 hPa, 59.0%)

- sky frequency in MHz (e.g. 8205 MHz)

- azimuth & elevation in degree

- time, MJD format

This means each T_{sys} value can be related to a certain scan, observed source, channel number, lower or upper sideband, meteorological parameters, sky frequency, elevation & azimuth and time.

data folder
log files

work folder
tsys.mat
tsysFreq.mat
chanNum.mat
LSB.mat
USB.mat
info.mat
source.mat
azi.mat
elev.mat
temperature.mat
pressure.mat
humidity.mat
mjd.mat

param folder
corr.mat
out.mat
meanTsys.mat
elevModel.mat

Extract (GUI): process selected data

Analysis (GUI): time series, correlate channels, adjustment, mean buttons
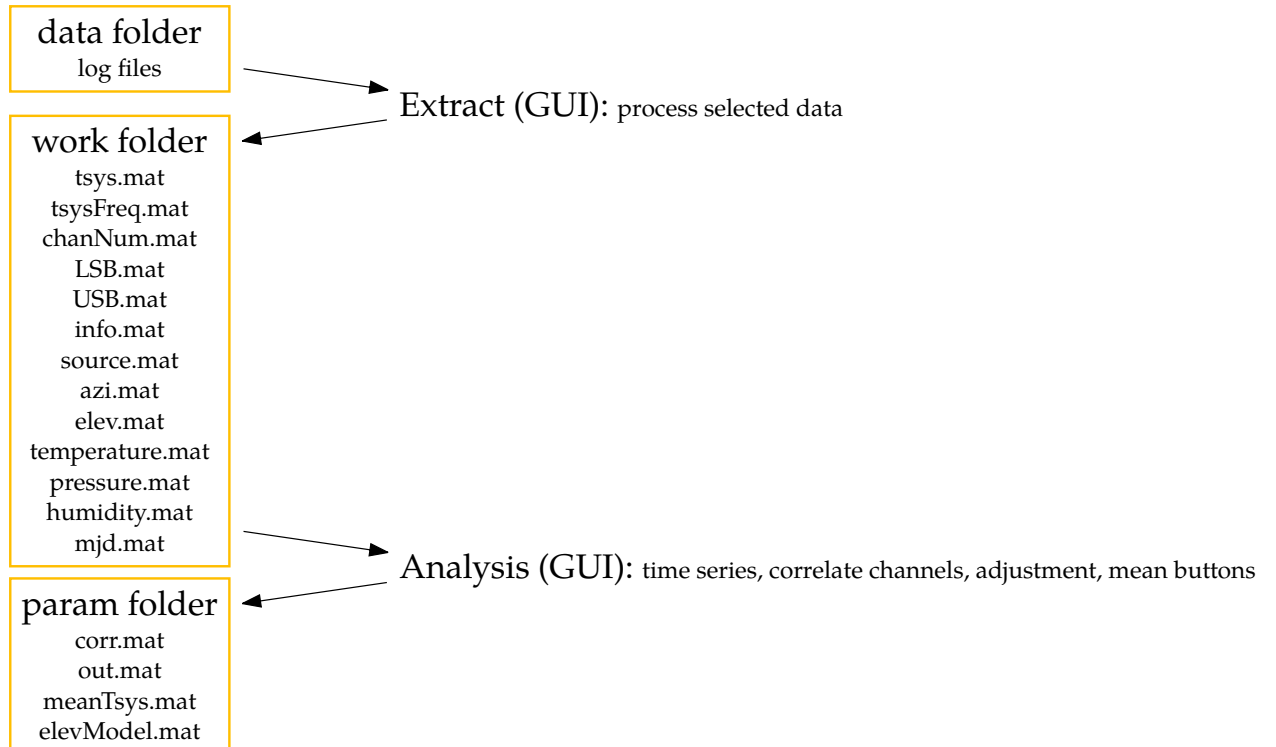
Fig. 5.3: Software architecture of extracting and analyzing T_{sys} measurements.

A Graphical User Interface (GUI) is developed to handle and to analyze the huge amount of data (Fig. 5.4). Fig. 5.3 shows the program structure of the MATLAB routine. The log files are stored in the folder data and are extracted appropriately. Then the extracted raw

data is processed. Each T_{sys} value and the corresponding parameters are stored in mat files separately. Each element of one of the mat files in the work folder corresponds to the equal element in another mat file in the work folder. This makes it easily possible to study several relations between the parameters, e.g. T_{sys} and elevation or T_{sys}, time and atmospheric temperature. Based on this data structure, MATLAB sub routines are developed to realize several calculations, such as: correlation coefficients, daily means of the T_{sys} and even model parameters for an elevation model. These estimations can be executed by using the GUI and pressing the labeled buttons. It is this GUI which enables studies of the T_{sys} measurements of AuScope VLBI array and is used in this work.
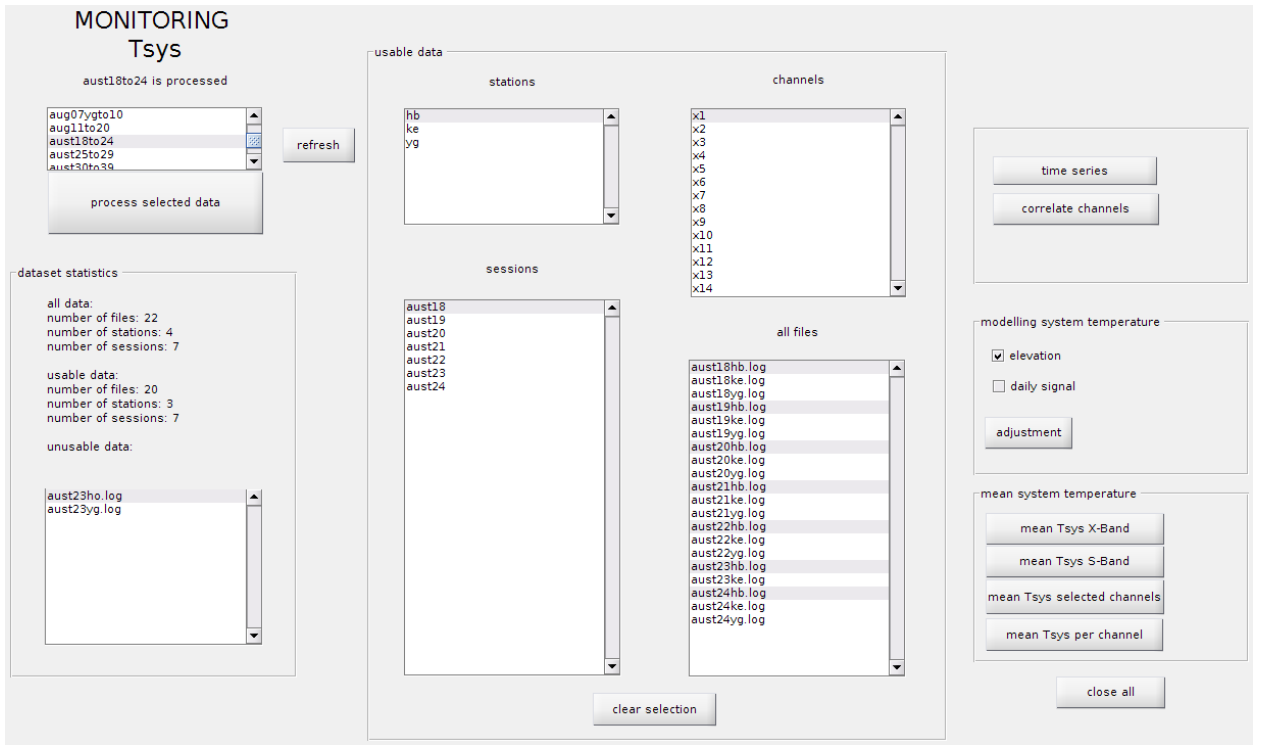
Fig. 5.4: Matlab GUI to analyze T_{sys} measurements.

Furthermore this monitor system represents a basis for other applications such a dynamic scheduling, because the log files can be scanned in real-time and a feedback of the sensitivity information can be provided.

5.2   Radio Frequency Interference (RFI)

Before the processing steps will be shown (see Sec. 5.3), a very important parameter which influences (degrades) the sensitivity has to be discussed: Radio Frequency Interference (RFI). RFI is one of the factors reducing sensitivity of radio telescopes. Petrachenko et al. [2009]

outline the impact of RFI on the VLBI2010 observing system. Some of the characteristics are:

- The broadband VLBI2010 receiving system (frequency range from 2 to 14 GHz) must function in the somewhat hostile RFI environment of fixed, mobile, marine, aeronautical, or space- based transmitters.

- It is expected that conditions will degrade over time through greater demand for the 2 to 14 GHz spectrum.

- The highly directional VLBI beams are comparatively robust against RFI.

- Due to the wide separation of VLBI antennas, the same interfering signal is rarely seen at both ends of a baseline and so do not correlate.

- RFI that is strong enough to saturate the receiving system can destroy the entire observation.

- The VLBI2010 broadband receiving system provides the freedom to shift selected bands to avoid RFI

RFI can be divided into two classes, external and internal RFI (Ilin [2008]). Tab. 5.1 lists the most common internal RFI sources.

Infrastructural RFIs	RFI from scientific instruments	others
Computers, Laptops, Screens, Wireless application, Bluetooth, Wireless Local Area Network (WLAN), Fluorescent lamp, Heating, Ventilation, Air conditioning (HVAC), Keyboard Video Mouse (KVM), Disk units	Hydrogen Maser, Antenna steering servo electronic, Scientific instruments, Signal generator, Spectrometers	Parking radars, Car engines (not diesel), Microwave ovens

Tab. 5.1: Internal radio interference sources inside some radio observatories. (Lopez-Perez [2010], Ilin [2008] and Grypstra & Keller [2009])

External RFIs can be divided into two classes, ground based- and aero- and spaceborn RFIs. Radio geodetic observations are done with elevation down to 5° and therefore they are subject to ground based RFI, which is often more harmful due to the high transmission power and closer localization. Increasing RFI, especially in the S-band, can be found at severals stations (Lopez-Perez [2010], Ilin [2008] and Grypstra & Keller [2009]). Most of external

RFIs are closely connected with human activities around the place of the VLBI observatories location. Radio telescopes were built in places remote from major settlements, but now this situation changed. As a result powerful RFI from mobile phone base station transmitters can occur near radio telescopes (Ilin [2008]).

The reduction of RFI is one of the goals of VLBI2010, which can be achieved by e.g. observing in different frequencies (Niell et al. [2006]). The receiving system (Sec. 4.3) of the AuScope array provides observations in different frequencies (2-3 and 8-9 GHz), but it does not represent a ultimate VLBI2010 broadband receiving and recording system (2-14 GHz). Detailed studies of the RFI for the AuScope array do not exist, but it is assumed that the AuScope array suffers from RFI, especially in the S-band (channel 13 and 14) of Hobart due to the radiation of mobile phone base station transmitters. RFI in Yarragadee can occur due to the co-located SLR aircraft avoidance radar.

5.3   Data preprocessing of the system temperature

Before the recorded T_{sys} measurements can be used, outliers have to be deleted 5.3.1. Furthermore the correlation between the channels is estimated in order to obtain knowledge about differences in the T_{sys} between channels.

5.3.1   Outliers

Effects such as ground spillover and RFI are present for the AuScope array and lead to a decrease or even in the case of RFI to a degradation and a stop of the system performance. To eliminate these effects in the further analyses the range for usable T_{sys} has been chosen from 0 to 200 K. In other words, scans with negative T_{sys} or T_{sys} above 200 K are not included in any further calculations. Figure 5.5 show the relative loss of scans due to this limitation for the S-band of Hobart.

The X-band for Hobart, Katherine and Yarragadee shows a very low loss of measurements (the ratio of used to total number of scans for all sessions are above 95%). Only Yarragadee shows in the period of Feb. to Apr. 2015 a small number of sessions where a high number of scans per sessions were lost. The S-band shows for Hobart (Fig. 5.5) only for channel 13 and 14 a high loss of scans (approximately 50% scans are not in the range of [0, 200 K]). Katherines S-band shows a high number of sessions above 90%. The S-band for Yarragadee has 60 sessions where at least one channel is lower than 90%, starting in Feb. 2015 the loss
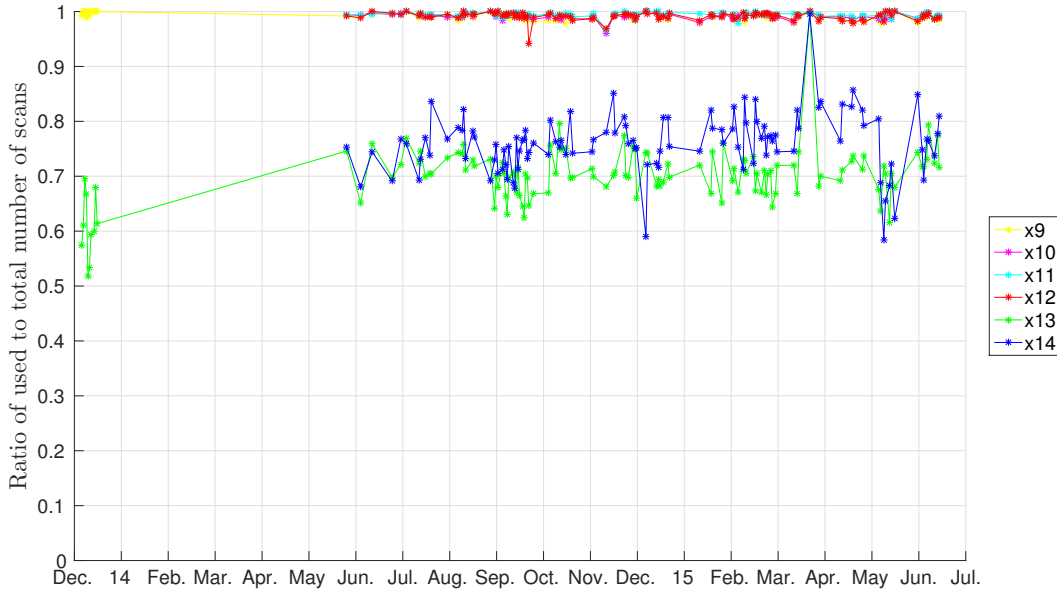
Fig. 5.5: Ratio of used [0, 200 K] to total number of scans of the S-band of Hobart.

is high for all S-band channels.

5.3.2   Correlation between channels

Fig. 5.6 demonstrates the variations in terms of the T_{sys} time series that can occur between channels. Additionally a variation per session of channel variations is noticed. To analyze these variations, this section provides a quantitative global measure of dependence between the channels. It is assumed that in a perfect receiver system without noise and neglecting the difference in frequency, T_{sys} is channel by channel equal. To analyze unexpected variations between the channels the Pearson correlation coefficient is estimated between all channels in X-band and S-band. This method is robust against the differences in scales of the T_{sys}. The results of the lower sidebands are not shown because they are almost equal to the corresponding upper side bands. Fig. 5.6 serves as a demonstration of unexpected variations between channels.

The daily signal, which can be found for channel 2 and channel 3 in Fig. 5.6, occurs for other channels and the other stations too, but underlies irregularities and may be subject to further studies. Pattern recognition could be a reliable tool to study those and other variations during a session and between the channels. Anyway, some results in terms of a daily signal are mentioned here: Hobart shows for channels 1-4 and 6 a strong daily signal
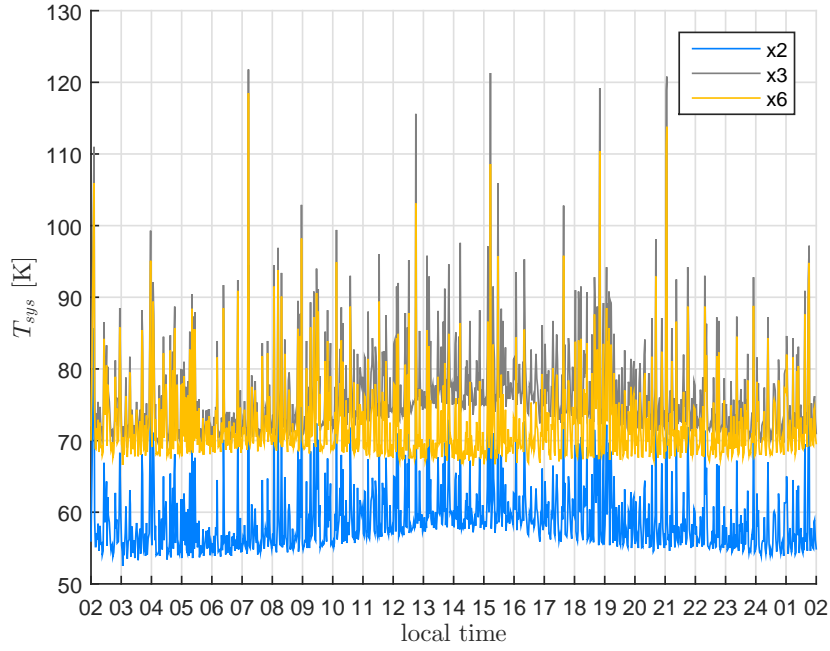
Fig. 5.6: Time series of channels 1, 3 and 6 for session 1522, Yarragadee. Offsets between time series can be found and peaks at 3pm local time for channels 2 and 3 can be found. Additionally a variation per session of channel variations is noticed.

for a high number of sessions. Channels 5 and 7-8 show a weaker daily signal (Fig. 5.7a). A significant daily signal can be noticed of all channels for a very high number of sessions in Katherine (Fig. 5.7b). Yarragadee shows sometimes unexpected jumps during the sessions (Fig. 5.8).

14 measurements of the T_{sys} are obtained per scan (4.4). The estimation of an average of the T_{sys} per scan requires knowledge of the variations between the channels. If the correlation between the channels is high (>80%), a simple average is taken. A low correlation tells us something about systematics in the receiver system and disturbances due to RFI. Figures B.1 to B.3 in the appendix show the detail time series of the mean correlation coefficient of each channel for the X-band. The mean correlation coefficient is an arithmetic mean estimated by using all correlation coefficients of this channel, but neglecting the correlation with itself (Eq. 5.2).

Hobart shows a high mean correlation coefficient for all sessions. Only the sessions a1315, aust64 and aua008hb are below 80%. Channel number 5 is not in a good agreement with the other channels. In comparison to Hobart, Katherine shows a high mean correlation coefficient for all sessions as well. Only a13 is slightly decreased (70%) and aua005 shows a bad correlation. Yarragadee shows a high mean correlation coefficient. In Feb. to Apr.

(a) Hobart

(b) Katherine
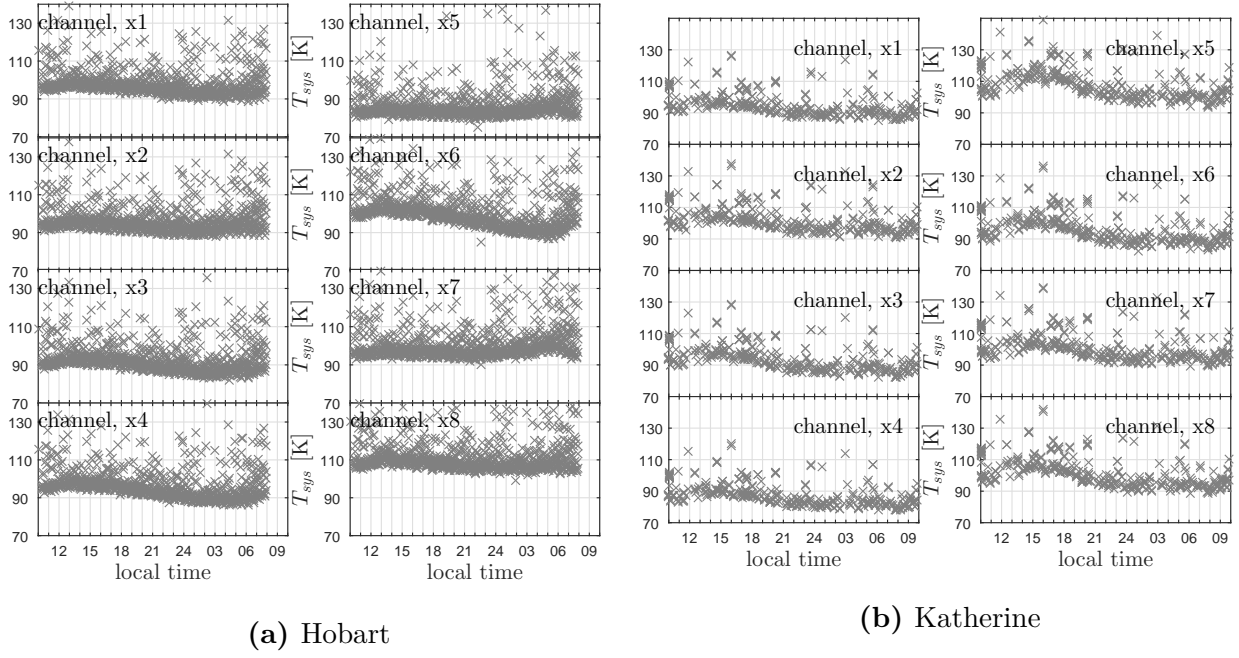
Fig. 5.7: Variations of the T_{sys} between channels of a session (aust69)
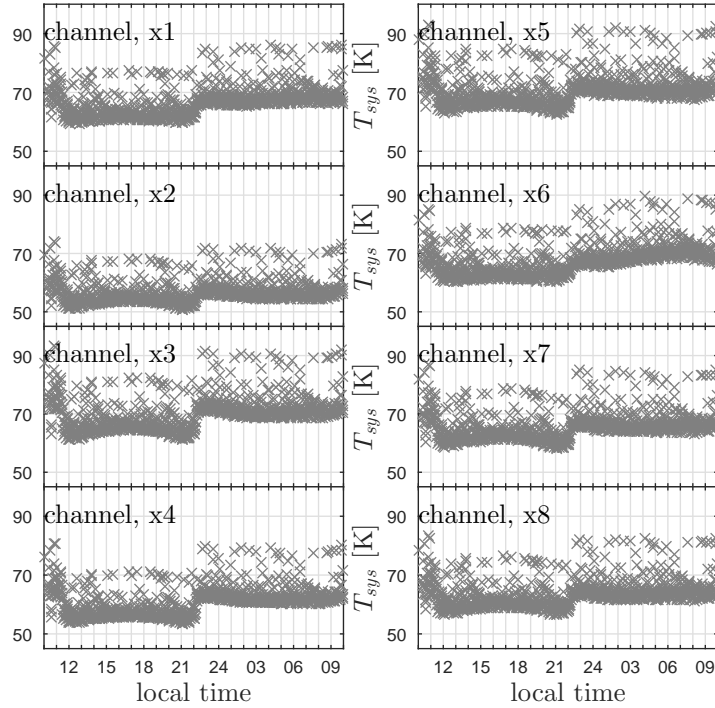
Fig. 5.8: Variations between channels in X-band of Yarragadee session aust69 (13/12/2014).

2015 exist a small number of worse sessions (<80%): aug002, aug003, aug007, a1511yg and aug010yg. The mean correlation coefficients for the S-band are clearly decreased in

channel id	x_1	x_2	x_3	...	x_n
x_1	ρ_{11}	ρ_{12}	ρ_{13}	...	ρ_{1n}
x_2	ρ_{21}	ρ_{22}			
x_3	ρ_{31}		ρ_{33}		
...	...			...	
x_n	ρ_{n1}				ρ_{nn}

Tab. 5.2: Correlation coefficients between channels

$$\mu_{\rho j} = \frac{1}{n} \sum_i^n \rho_{ij} \tag{5.2}$$

with $\mu_{\rho j}$ ... arithmetic mean of correlation coefficients of channel j
         ρ_{ij} ... correlation coefficient

comparison to the X-band and the channels 13 and 14 show an offset in comparison to the other channels. Furthermore the time series of all stations show a higher scatter in the S-band than the X-band. Hobart's S-band shows a significant difference between channels 13 and 14 in comparison to the other channels. May be caused by ground based RFI, channels 13 and 14 do not show any correlation (0%), whereas channels 9 to 12 are scattered around 40%. Katherine shows in comparison to Hobart overall increased mean correlation coefficients and the channels 13 and 14 show a higher correlation (60%) than the others (35%). Channel numbers 9 and 10 are not in a good agreement with the others for a high number of sessions. Yarragadee shows increased mean correlation coefficients for the channels 9 to 12 (50%). Again channels 13 and 14 are decreased (30%), but not that much separated from channels 9 to 12 as in Hobart.

5.4 Atmospheric contribution

The system temperature is affected by the atmosphere (see Sec. 3.2.1). The atmosphere serves as an additional source of noise, because it emits radiation by itself. This depends strongly on the temperature of the atmosphere. Furthermore the noise contribution increases with lower elevation due to the increasing thickness of the atmosphere. The theory of the atmospheric contribution is discussed in Sec. 3.2.1. Now, in this section, the atmospheric contribution of the T_{sys} is analyzed based on the data of the recorded T_{sys} measurements of the AuScope VLBI array.
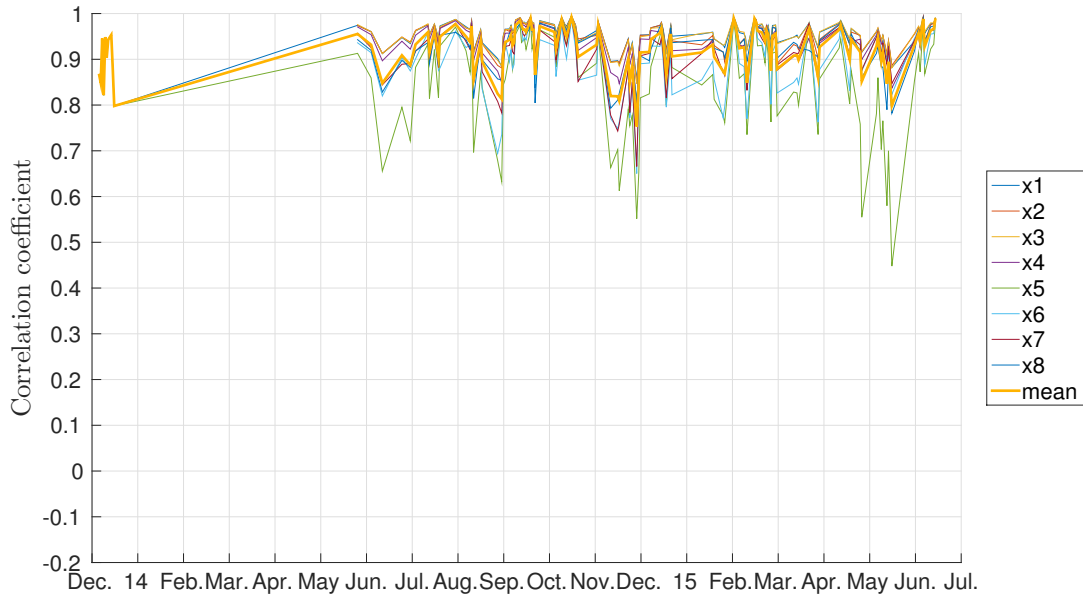
(a) X-band
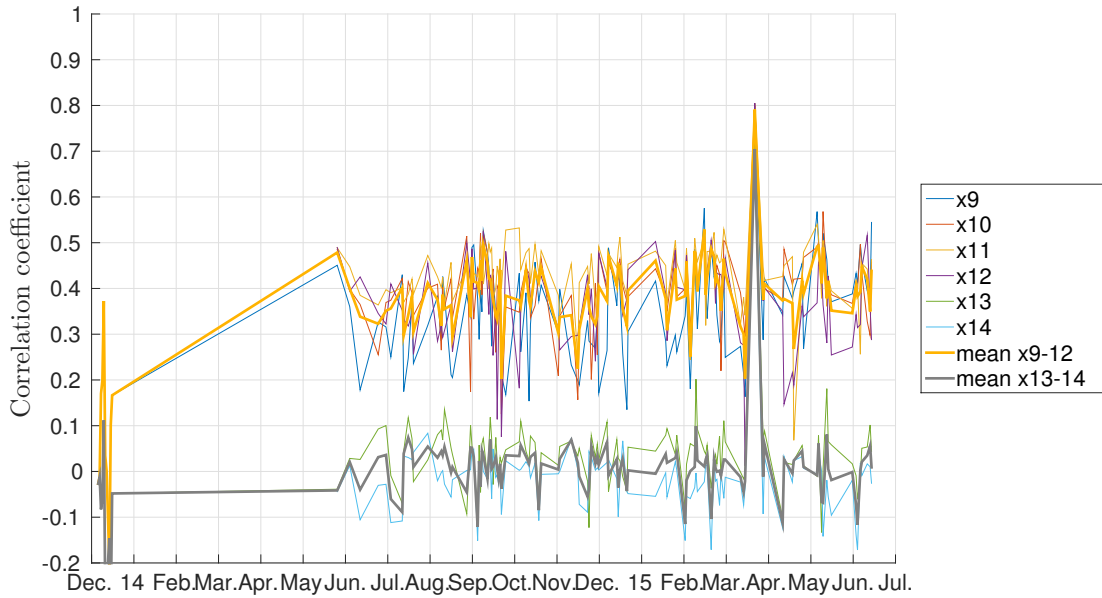
(b) S-band

Fig. 5.9: Hobart, time series of the correlation coefficient (X-band and S-band)

5.4.1 Modeling the atmospheric contribution

The system temperature is a function of the elevation of the pointing direction of the antenna. This circumstance is considered in the VLBI scheduling softwares (Sun [2012] and Gipson [2012]), because the sensitivity of the antenna, described by the SEFD (Sec. 3.3), decreases

34

with lower elevation. In this work the T_{sys} is modeled (least squares adjustment) by use of Eq. 5.3, which simply accounts for the increasing length of the slant path for decreasing elevation.

$$y = a + \frac{b}{\sin(elev)} \tag{5.3}$$

with y ...observed T_{sys} [K]
           a, b ...unknowns
           $elev$ ...elevation

The unknowns a and b will be adjusted for each session and they are used to estimate the T_{sys} in zenith direction (Eq. 5.4).

$$T_{sys}^{zenith} = a + \frac{b}{\sin(90°)} = a + b \tag{5.4}$$

with T_{sys}^{zenith} ...T_{sys} in zenith direction [K]

Average system temperature

The T_{sys} in zenith direction (T_{tsys}^{zenith}) represents the reference value for any further studies, because it is free of elevation dependent systematics. By modeling the elevation dependency including all scans of a sessions only *one* value per session, per station and per channel is obtained. For some results, such as the visualization in Fig. 6.9 to 6.11, it is convenient to estimate an average value using the T_{sys}^{zenith} of each channel. If e.g. the T_{sys}^{zenith} for the X-band is required, the average T_{sys}^{zenith} of channels 1 to 8 is estimated.

Fig. 5.10 shows the modeled elevation dependency and Fig. 5.11 shows the time series of b for Hobart and Katherine. Both are scattered around an average value of about 4.6 (X-band) and are stable in time. Katherine may draw a yearly signal due to atmospheric temperature variations. The time series of the other component, the T_{sys}^{zenith}, is plotted in Fig. 5.18, which is discussed in the section about the receiver contribution (Sec. 5.5), because the T_{sys} inheres systematics due to errors in the receiver hardware components.
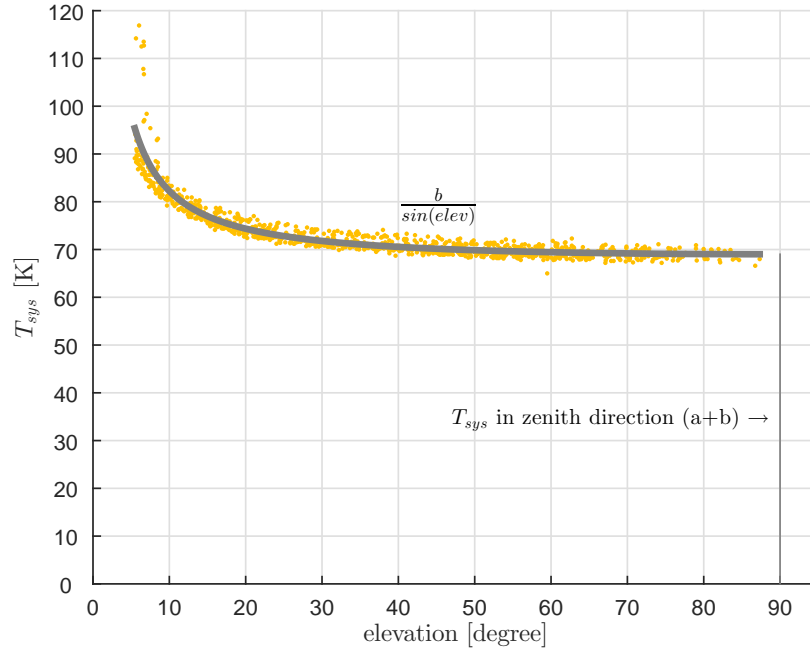
Fig. 5.10: Modeled elevation dependency of the T_{sys} for one channel of one session.
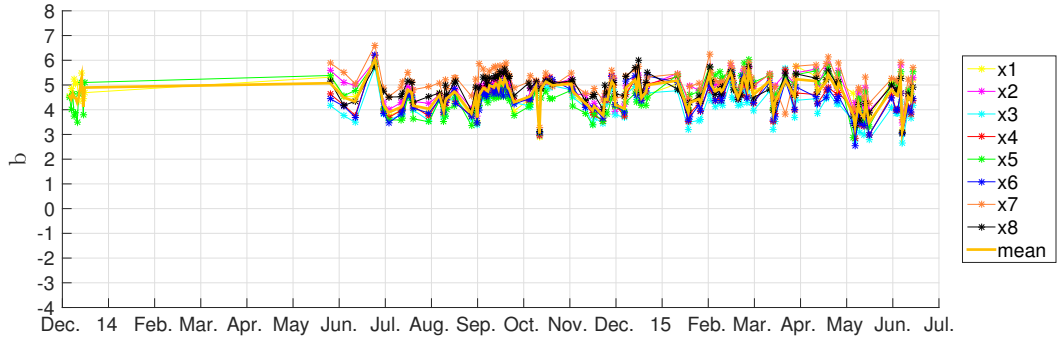
(a) Hobart X-band
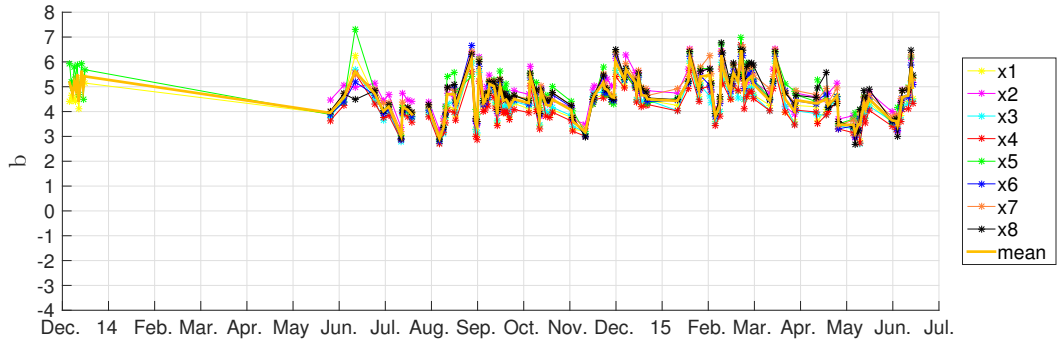
(b) Katherine X-band. A yearly signal due to atmospheric temperature may be noticed.

Fig. 5.11: Time series of elevation dependency b of the X-band for Hobart and Katherine

Tab. 5.3 lists the magnitude of factor b, estimated using all AUSTRAL sessions since December 2013 until July 2015. Hobart and Katherine show an equivalent mean elevation dependency for the X-band and almost the same for the S-band, whereas Yarragadee is decreased in both bands. The reliability of Yarragadees values must be under critical examination, because errors in the measuring process due to failures in the calibration, which can be seen in Fig. 5.8 are assumed. The magnitudes of the average T_{sys}^{zenith} per frequency band is listed in Tab. 5.4.

	Hb	Ke	Yg
X	4.6	4.6	2.6
S	3.0	2.8	2.1

Tab. 5.3: Magnitudes of factor b

	Hb	Ke	Yg
X	95	95	65
S	115	117	110

Tab. 5.4: Magnitudes of the T_{sys}^{zenith} $(a + b)$

5.4.2   Quality of the elevation model

This section is based on the studies of the elevation dependency of those residuals which lie outside the range of $(-2\sigma, 2\sigma)$. The residuals are the difference between the model and the observations. σ is the standard deviation of the residuals and the values range from $(-2\sigma, 2\sigma)$ was determined by random graphical assessment, such as in Fig. 5.12. Appendix D.1 to D.6 show the rate of the residuals outside the range of $(-2\sigma, 2\sigma)$ of all sessions per station and per channel. A strong increase in the rate can be found for elevations lower than 10 degrees. This means, that the model presented in Sec. 5.4.1 fails for those elevations. Two effects can be found. Ground spillover is a common effect, which leads to an increase in T_{sys}. The model approach tries to fit these data as well. Therefore, the rise of the curve is steep and the residuals tend to be affected systematically. Sixty percent of all residuals outside the range of $(-2\sigma, 2\sigma)$ of Hobart's X-band are smaller in elevation than 10 degree (Fig. 5.13). This value is estimated by use of all sessions. The same calculation approach yields 64% for Katherine and 51% for Yarragadee, respectively. The S-band yields 21% for Hobart, 30% for Katherine and 20% for Yarragadee.
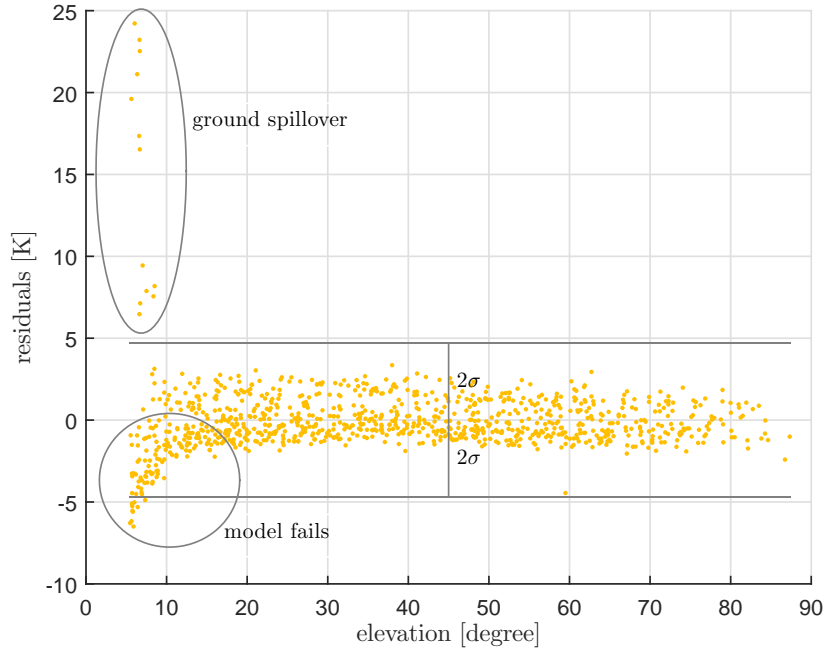
Fig. 5.12: Residuals of the applied elevation model of session 1522 of Yarragadee for channel x1. The elevation model fits with high acceptance for elevations higher than 10°. Ground spillover leads to model failures for elevation lower than 10°.
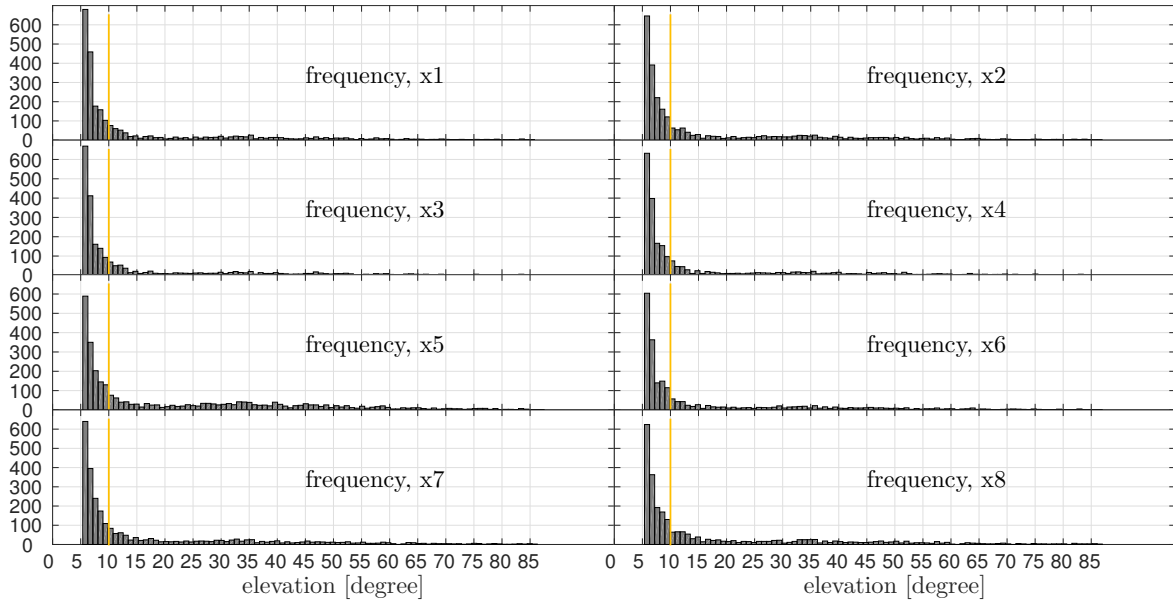
Fig. 5.13: Hobart X-band: Histogram of residuals larger than 2σ.

A measure of the quality of a model approach represents the root mean square (RMS), which is defined (Eq. 5.5) as the square root of the mean of the squares of a sample (residuals of the elevation model).

Tab. 5.5 shows the mean RMS values of the X- and S-band of each station for all sessions.

$$res_{RMS} = \sqrt{\frac{1}{N} \sum_{n=1}^{N} res^2} \tag{5.5}$$

with N ... total number of residuals
           res ... residuals [K]

The applied model (Eq. 5.3) shows consistent RMS values for all stations.

	X-band	S-band
	[K]	[K]
Hobart	6	11 (without x13, x14)
Katherine	6	10
Yarragadee	5	14

Tab. 5.5: Mean RMS of the residuals of the elevation model approach

5.4.3   Atmospheric temperature at the site and the system temperature

The influence of the temperature of the atmosphere on the system temperature has already been mentioned in Sec. 3.2.1. Eq. 3.10 yields the contribution of the cosmic noise component and the atmospheric component. The term which contributes for the atmosphere is proportional to the temperature of the atmosphere (t_{atm}). This relation is under investigation in this section. The atmospheric temperature t_{atm} is measured at each site and is written into the .log files. In the same way as the T_{sys} it is recorded per scan. The atmospheric contribution fluctuates on a daily and a yearly basis. Fig. 5.14 compares the T_{sys} and the t_{atm} of one session (one day) for Hobart and Katherine. The correlation between the system temperature and the atmospheric contribution of this single sessions is significant, but can be found for any further sessions as well. Fig. 5.15 shows the yearly contribution of the t_{atm} to the T_{sys}. The average of the T_{sys} in zenith direction and the average of the t_{atm} of each session is plotted. Katherine may show some t_{atm} failures during Oct. and Nov. 2014. Yarragadee is not shown in both cases (short and long time trends), because there are "jumps" noticed during the sessions. This may occur due to errors in the calibration signal which is actually the way how T_{sys} is measured (see Sec. 5.5). Additionally it has to be mentioned, that the LNA is not cooled in the case of the AuScope Antennas. The signals in the T_{sys} may not only be due to the additional radiation of the atmosphere. The increase of the receiver temperature must be considered as well, which may influence the noise level and contribute to the T_{sys}.

(a) System temperature in zenith direction of channel 6 at Hobart during session aust49.

(b) System temperature in zenith direction of channel 6 at Katherine during session aust39.
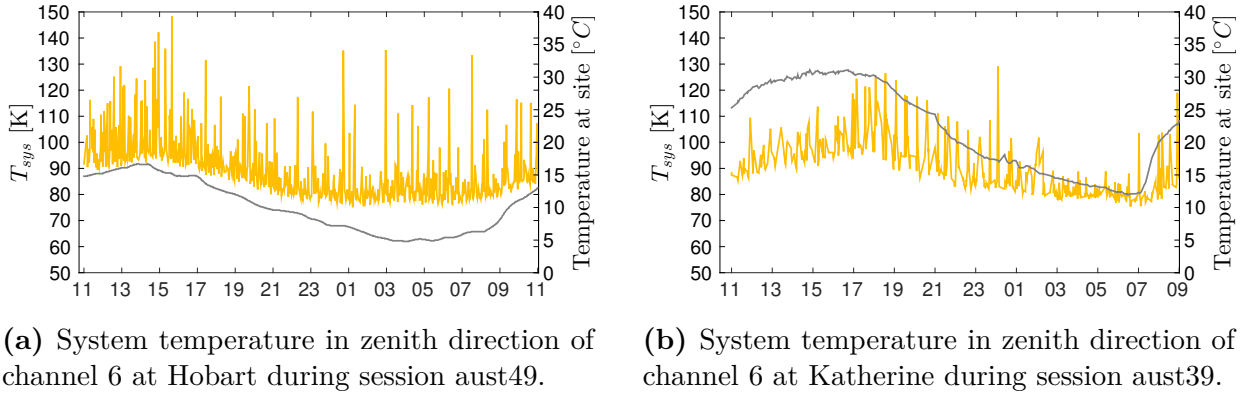
Fig. 5.14: Comparison of the system temperature (orange line) with the atmospheric temperature measured at the site (gray line) during one session. The system temperature of channel 1 (orange line) is plotted and shows a daily amplitude of about 10 K due to the influence of the temperature of the atmosphere for Hobart and Katherine.

(a) Hobart

(b) Katherine
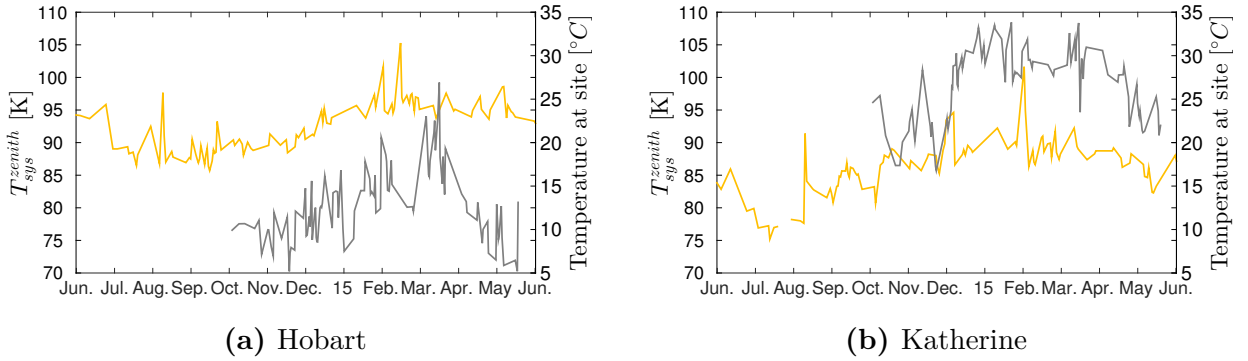
Fig. 5.15: Comparison of the system temperature in zenith direction (orange line) with the atmospheric temperature measured at the site (gray line). The average T_{sys} in zenith direction of channel 1 (orange line) is plotted of almost one year of AUSTRAL VLBI sessions. Hobart and Katherine are shown.

5.5   Receiver contribution

Besides the atmospheric contributions and RFI, a receiver system itself affects the T_{sys}. It is even the main component with respect to the absolute magnitudes. Additionally variations and modifications in the receiver system can influence the T_{sys} on the time axis as well. In order to understand the impact, the receiver system characteristics are discussed (Sec. 5.5.1). Finally the receiver noise components which are found for the AuScope antennas are shown in Sec. 5.5.2.

5.5.1   Receiver system characteristics

As already mentioned in section 3.2, the main component of the T_{sys} is the noise of the receiver system (Fig. 5.16a). This is also the case for the AuScope antennas. A drawing of

the receiver system is shown in Fig. 5.16.

(a) Drawing of the antenna used in the AuScope VLBI array with the main components labeled

(b) The signal path from the feed at the focal point to the receiver in the antenna hub to the IF signal outputs to the DBBC
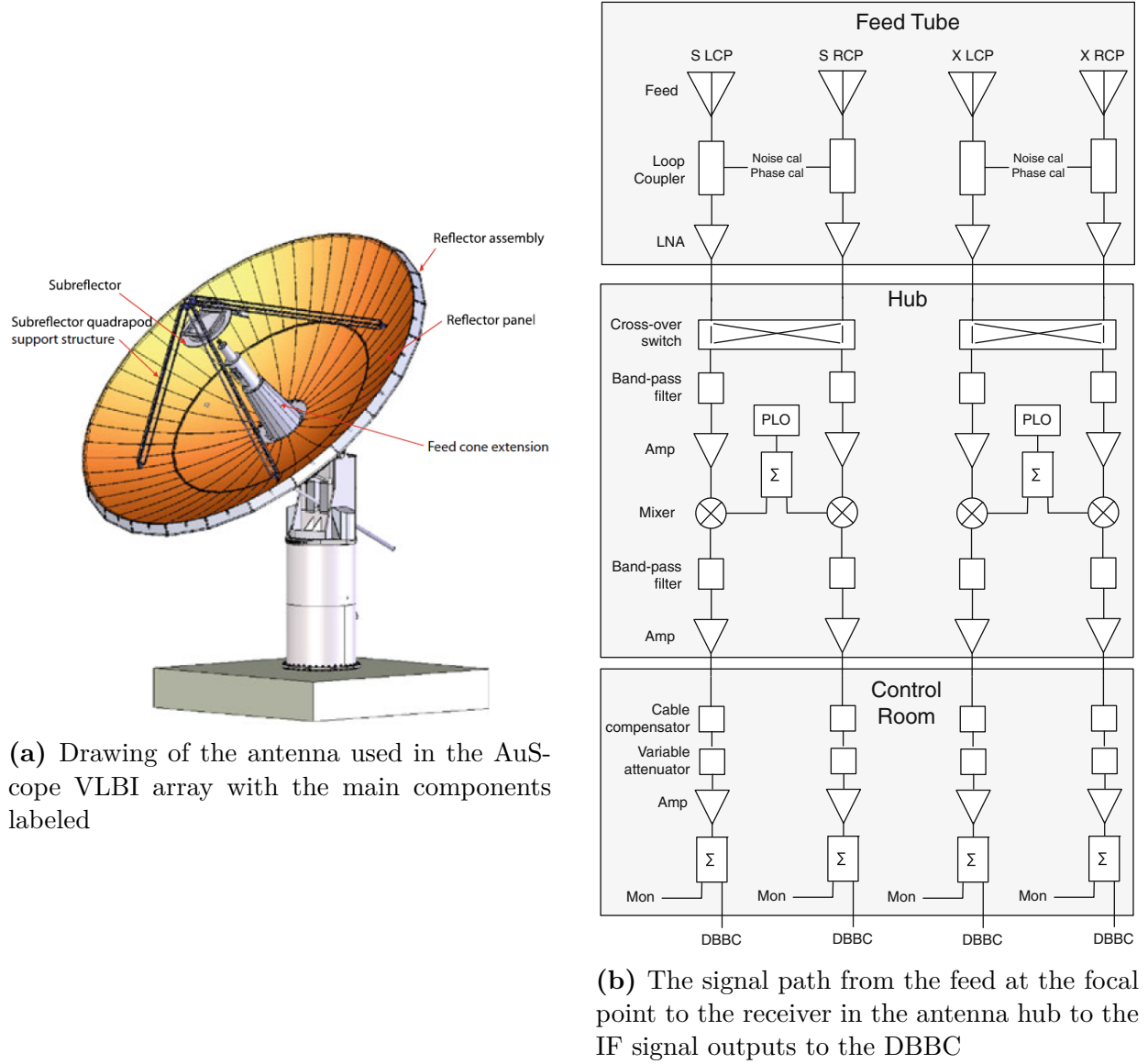
Fig. 5.16: Drawings of the antennas used in the AuScope VLBI array with the main components labeled and a sketch of the signal path from the focal point of the feed to the DBBC (Lovell et al. [2013]).

The known components of the receiver system, which contribute to the T_{sys} are the quadrapod (support structure), the sub-reflector, the feed and the low-noise amplifier (LNA). The magnitudes of these components are shown in Tab. 5.6.

The LNA of the AuScope antennas are not cooled, therefore the noise input level is elevated in comparison to the cryogenic LNA (Petrachenko [2013]) and subject to variations in the ambient temperature. This circumstance has to be considered in the interpretation of the atmospheric temperature dependence of T_{sys}. The expected T_{sys} using the breakdown of

Parameter	X Band [K]	S Band [K]	Additional Notes
LNA	30	50	Manufacturer Specification
Feed	35	25	Based on Ohmic losses above at 290 K
Quadrapod, Subreflector and S-Band Horn Scatter	10	5	
Galactic + Atmospheric	10	10	
T_{sys}	85	90	

Tab. 5.6: Expected performance of the 12m radio telescope with dual band S/X feed (Lovell et al. [2013])

Lovell et al. [2013] of the AuScope array amounts to 85 K for the X-band and 95 K for the S-band.

The mentioned components of the T_{sys} of the AuScope array are located in the feed tube and hub, which refers to the front end of the receiver. In this part of the signal path (Fig. 5.16b), the signal is amplified and down converted to a baseband suitable frequency. The front-end receiver also permits inclusion of notch filters (passes most frequencies unaltered) to block interference signals prior to down-conversion. The rejection of frequencies leads to a variation of the power and T_{sys}, respectively. The down-converted signals from the front-end receiver are then carried underground to the control room, into the digital baseband converter (DBBC) for sampling (the sampled data are then recorded into a disk using a Mark5B+ unit). There are four input bands of the DBBC. The relation between input bands, DBBC channels and X,S-band is shown in Fig. 5.17.

Fig. 5.17: Relation between the narrow intermediate frequency band (IF), the channel number (BBC) and the sky frequency (X,S-band) (Lovell [2015]).

The IF A (narrow intermediate frequency band) is split into the first four BBC channels. IF A and IF B (channel 5-8) cover the X-band and the IF C (channel 9-12) and IF D (channel 13,14) cover the S-Band. The detailed description of the extraction of the T_{sys} information is shown in Sec. 5.1 and the corresponding sky frequencies are shown in Sec. 4.3. This section provided a brief description of the signal path and its components of the receiver systems of the AuScope array. A detailed description can be found in Lovell et al. [2013].

5.5.2 Receiver noise components

The feed and the LNA contribute with 75% to the T_{sys} (Lovell et al. [2013]). In comparison to a cryogenic LNA, the LNA of the AuScope antennas are not cooled, therefore the contribution of noise is elevated. Additionally, changes in the ambient temperature may affect the T_{sys} (see Sec. 5.4.3). Another reason for elevated T_{sys} may be water (condensation) on the feed window or overcast conditions (Lovell [2015]). The injection of a calibration signal must be under critical examination, because the noise diodes can be subject to overheating or the noise diode are not well calibrated. The DBBC plays a role too, such as overheating or restarting of the DBBC can effect the T_{sys}. Any changes in the hardware configuration, such as re-cabling can effect the T_{sys} as well. Fig. 5.18 shows unexpected "jumps" in the long time series of the T_{sys}^{zenith} of individual channels for Hobart and Katherine. Errors in the calibration signal may be a reason. Yarragadee shows unexpected "jumps" after the session aust74 (around 1/1/2015) (see Fig. 5.8), which may be due to restarts of the DBBC. In general, the stability of power inputs is under critical examination. Time series of the T_{sys}^{zenith} of all stations can be found in the appendix C. Furthermore, the average values of the T_{sys}^{zenith} per channel are listed in appendix F.

5.6 Conclusion

A high number >90% of the T_{sys} measurements beneath 200 K is found for the AUSTRAL sessions. However, there are outliers, mainly due to RFI. Especially the S-band, in detail the channel 13 and 14, suffer from RFI. This result can also be found for the variations between channels: The correlation between channels in X-band is of high acceptance (>90%), whereas the S-band shows a low correlation, or even no correlation. This means that the frequencies in channel 13 and 14 should be shifted to frequencies with less RFI for future sessions. However, the entire S-band suffers from RFI, therefore it will be challenging to find appropriate observing bands in the S-band.

Systematics can be found, attributed to the atmosphere: A clear elevation dependence and
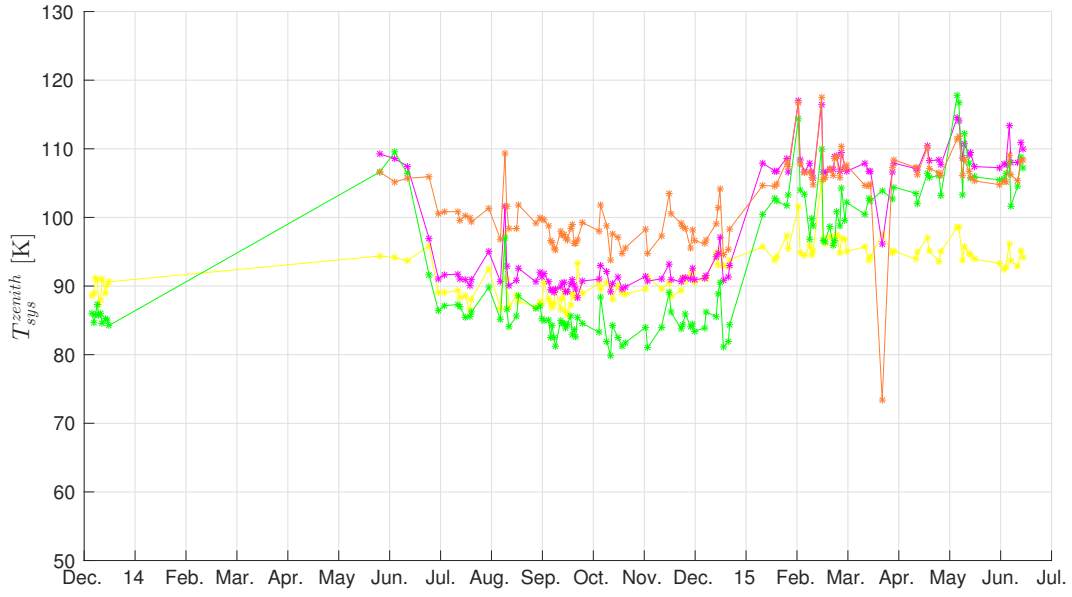
(a) Hobart time series of T_{sys}^{zenith} of channels x1, x2, x5 and x7 are shown. A jump is noticed at around 1/1/2015. Any changes in the hardware configuration may cause such a systematic in the T_{sys}.
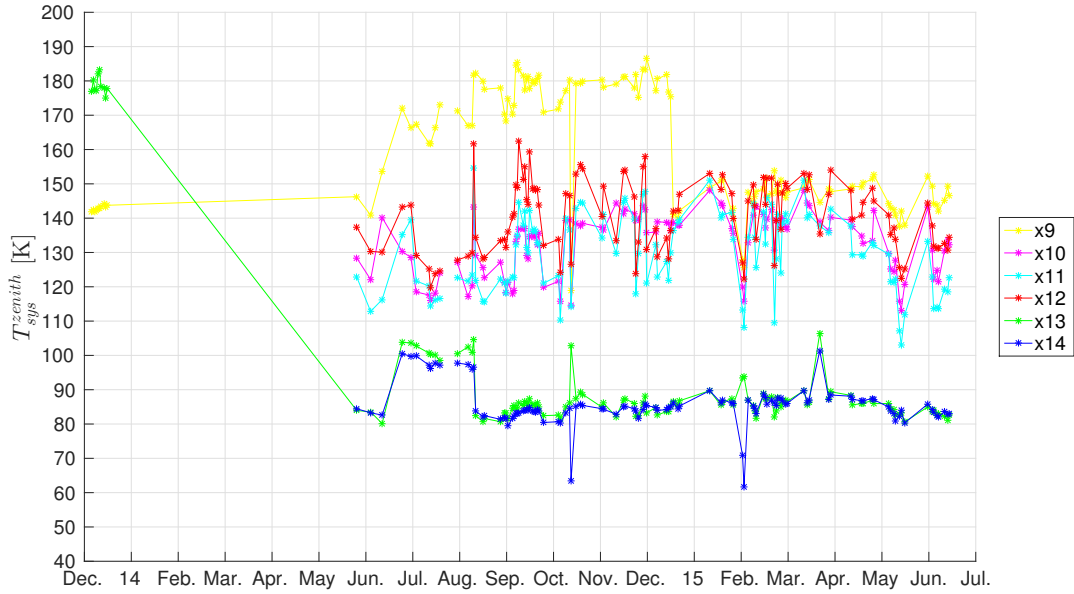
(b) Katherine time series of T_{sys}^{zenith} of the S-band. Channel x9 shows an unexpected time series.

Fig. 5.18: Time series of T_{sys}^{zenith} for Hobart and Katherine (X-band and S-band). The data has already been reduced by the atmospheric elevation dependent influence.

a yearly and a daily atmospheric temperature dependence. On the one hand this variation is due to the radiation of the atmosphere. On the other hand the receiver cools and heats

44

as well depending on the ambient temperature, which forms a noise input as well. It is still to be clarified whether, it is a real noise load or a systematic effect in the calibration signal. If we assume the heating of the noise diodes to be stable and not subject to ambient temperature changes, the daily and yearly noise signals are real noise, which affects the VLBI correlator precision. The magnitude of this impact on the scan length is discussed in Sec. 7.2. Anyway, an examination of the calibration signal stability of the AuScope antennas can create clarification.

A simple elevation model has been applied to account for increasing noise at lower elevations. The AUSTRAL sessions since December 2013 until July 2015 has been used to find reliable model parameters. The magnitudes of the estimated model parameters are consistent for Hobart and Katherine. Yarragadee shows a lower elevation dependence, but the T_{sys} measurements must be under critical examination. Unexpected "jumps" in the time series of the T_{sys} measurements in Yarragadee are noticed, which decreases the reliability of the elevation model parameters of Yarragadee. A detailed discussion of the importance of the elevation corrections can be found in Sec. 7.3.3.

Yarragadee does not show any temperature dependence, because unexpected "jumps" in the measured T_{sys} occur, which must be subject to further investigations, but DBBC restarts may be a reason.

The T_{sys} measurements of Hobart and Katherine are stable during a session. This means the calibration signal is stable during a session and relative changes in the T_{sys} are correct. The absolute T_{sys} level must be under critical examination, because restarting the receiver system can affect the calibration signal and therefore influences the measured T_{sys}. Modifications such as re-cabling influences the sensitivity as well. This means that any modifications of the receiver system in the future must come along with a check of the T_{sys} values.

6 The system equivalent flux density of the AUSTRAL VLBI sessions

System Equivalent Flux Density (SEFD)
-unit: Jansky [Jy]
-measurement of the sensitivity performance of an antenna
-the higher the SEFD, the lower the sensitivity

re-estimated SEFD

data from correlation report

per session

high reliability

(indirect) measured SEFD

data from log.-file measured within the DBBC

per scan

absolute magnitudes must be reviewed critically

absolute measured SEFD can be corrected with re-estimated SEFD

Fig. 6.1: Overview of the SEFD analysis this work is based on.

The System Equivalent Flux Density (SEFD) characterizes the sensitivity of the VLBI receiver. It is the power of all noise components, which is measured in Watts, divided by the area of the antenna. The SEFD and the radio sources are specified with the same physical concept. This means, that the SEFD describes a source, in fact: A source of noise. It is plausible, that the higher the SEFD the lower the sensitivity. In this work, two methods are presented to achieve the SEFDs for the AuScope array antennas. Sec. 6.1 shows the re-estimation of the SEFD with data from the correlation reports. Sec. 6.2 shows how SEFD can be measured indirectly. Finally, the methods are compared in Sec. 6.3. The re-estimated SEFD is used to correct the measured SEFD. It needs to be corrected, because the mea-

sured SEFD is derived from the T_{sys} measurements, which are biased systematically in the measuring process (see Sec. 5).

6.1   Re-estimation of the SEFD

The system equivalent flux density can be calculated as a function of the T_{sys}, because the SEFD is basically the flux equivalent of T_{sys} (Sec. 3.3 & Eq. 3.13). In this section another way of calculating the SEFD is shown and referred to as re-estimation of the SEFD.

6.1.1   Method of the re-estimation of the SEFD

The used data is extracted from corr.perl-files, which are generated after the correlation of the VLBI sessions. These correlation reports provide amongst other informations (Eg. station notes & Qcodes) also a table of mean SNR ratios. An example of such a correlation report can be found in the appendix A. The mean SNR ratio r_{SNR} is the mean ratio of a session between the observed SNR and the predicted SNR and is specified per baseline. Table 6.1 demonstrates the mean SNR ratios of session a1522.

Baseline Station1 - Station2	r_{SNR} X-band	n	r_{SNR} S-band	n
HOBART12 - HART15M	0.92	304	0.92	283
HART15M - KATH12M	0.88	320	1.05	312
HART15M - WARK12M	0.86	177	1.00	159
HART15M - YARRA12M	0.81	509	0.97	493
HOBART12 - KATH12M	1.03	832	0.85	831
HOBART12 - WARK12M	1.24	807	0.93	805
HOBART12 - YARRA12M	0.88	708	0.84	710
KATH12M - WARK12M	0.99	745	0.92	737
KATH12M - YARRA12M	0.90	763	0.93	764
WARK12M - YARRA12M	0.82	564	0.90	557

Tab. 6.1: Mean SNR ratios (r_{SNR}) of a1522, where n is the number of scans.

The r_{SNR} is estimated by baseline for the X- and the S-band and over all scans. Additionally the number of scans n is shown per baseline.

The r_{SNR} provides an information about the sensitivity, because the SNR predicted can be represented as a function of the SEFDs of the antennas of the baseline (Eq. 6.1).

$$SNR_{pred} = \frac{k}{\sqrt{SEFD_1 \ SEFD_2}} \tag{6.1}$$

with k ... factor, equal for both stations

If the r_{SNR} value is lower/higher than 1, then the observed SNR was lower/higher than predicted. In other words, the sensitivities of the baseline antennas were lower/higher than predicted.[1] This relation is used to adjust (least squares) the SEFD of each station. The definition of the r_{SNR} is shown in Eq. 6.2.

$$r_{SNR} = \frac{\frac{k}{\sqrt{SEFD_{1,obs} \ SEFD_{2,obs}}}}{\frac{k}{\sqrt{SEFD_{1,pred} \ SEFD_{2,pred}}}} = \frac{\sqrt{SEFD_{1,pred} \ SEFD_{2,pred}}}{\sqrt{SEFD_{1,obs} \ SEFD_{2,obs}}} \tag{6.2}$$

with $pred$ ... predicted (scheduled)
            obs ... observed

Eq. 6.2 is used to set up the observing equation in terms of the least square adjustment (Eq. 6.3).

$$\frac{\sqrt{SEFD_{1,pred} \ SEFD_{2,pred}}}{r_{SNR}} = \sqrt{SEFD_{1,obs} \ SEFD_{2,obs}} \tag{6.3}$$

A Taylor series expansion of the observing equation results in the design matrix. The scheduled SEFD values are used as approximate values. The number of scans are used to weight the observations. The elements of the design matrix are the first derivatives of Eq. 6.3 and they are shown in Eq. 6.4.

$$\frac{d(r_{SNR})}{d(SEFD_1)} = \frac{SEFD_2}{2 \ \sqrt{SEFD_1 \ SEFD_2}} \quad , \quad \frac{d(r_{SNR})}{d(SEFD_2)} = \frac{SEFD_1}{2 \ \sqrt{SEFD_1 \ SEFD_2}} \tag{6.4}$$

---

[1] It has to be mentioned that not only the sensitivity contributes to the SNR. Eq. 3.16 shows that the SNR depends on the source strength and the scan length as well. These parameters are assumed to be constant in the re-estimation method presented here, but they have uncertainties as well. The re-estimated SEFD are therefore contaminated by these unconsidered uncertainties. This fact is discussed in more detail in Sec. 6.1.4.

The number of observations in the adjustment are the number of baselines and the unknowns are the SEFDs of each station. Not only AuScope antennas are used in this adjustment, but also other stations which have contributed to the session (Eg. Warkworth and Hartbeesthoek). On the one hand this usage means that re-estimated SEFDs are available for those stations and on the other hand that they contribute to the SEFD results of the AuScope antennas as well, because the SNR is defined per baseline and not per station.

6.1.2   Quality of the re-estimation of the SEFD

One of the characteristics of the re-estimation is the low ratio between observations and unknowns. In the event of a loss of a baseline (observation), e.g. due to receiver problems, the normal equations are close to singular or badly scaled. Standard deviations of the unknowns (re-estimated SEFD) may be infinite, and therefore those sessions are not included in the further studies. The mean standard deviation of the re-estimated SEFD is for the X-band around 360 Jy for Hobart, Katherine and Yarragadee and for the S-band 260 Jy, 280 Jy, 330 Jy respectively. The accuracy (standard deviation σ) of the re-estimation is pretty stable over all sessions. Only some of the astronomic sessions (aua) (early May 2015) show standard deviations up to 3000 Jy for the X-band (the S-band is not affected) and therefore they are not used for further studies. Sixteen sessions of Hobart and Katherine and thirteen session of Yarragadee can not be used due to singularity in the least squares adjustment.
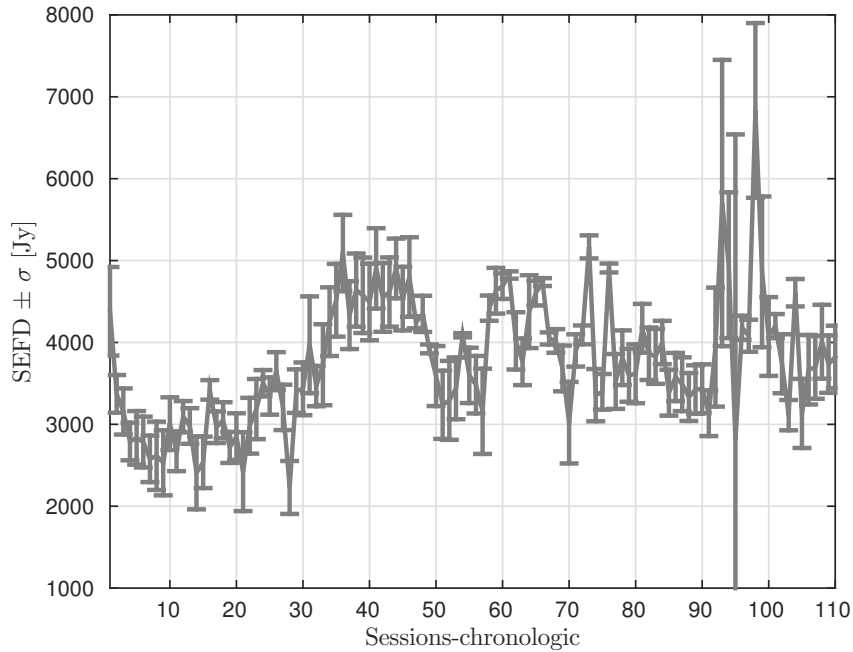
Fig. 6.2: Hobart, X-band, re-estimated SEFDs and standard deviations (σ)

6.1.3   Monitoring re-estimated SEFDs

The re-estimation of the SEFD is based on the mean ratio of the observed SNR and the predicted SNR. The exact method in theory of the re-estimation procedure is shown in Sec. 6.1.1, whereas this section demonstrates the operational implementation. A MATLAB routine is developed to extract and process the data and finally store the results appropriately. Fig. 6.3 provides an overview of the algorithm. The skd files which contain the VLBI schedule information and the correlation reports (.corr.perl) represent the raw input data, which have to be stored in the correct folders. The MATLAB routine extracts the predicted SEFD values from the skd folder and the mean SNR ratio plus the number of baselines of the corr.perl folder. In the next step these data is used in a least-squares adjustment to estimate the SEFD. The estimated SEFDs, referred to as the re-estimated SEFDs represent the result and are stored in the output folder. Additionally, plots of the comparison of the re-estimated SEFD and the predicted SEFD are created, which can be seen in Sec. 6.1.4.

$$\text{.skd folder} \qquad \text{.corr.perl folder}$$

predicted SEFD per station
$$SEFD_{1,2,pred}$$

mean SNR ratio of observed and predicted ratio: $\qquad$ number of baselines
$$r_{SNR} \qquad\qquad n$$

extracting

$$\frac{SEFD_{1,pred}\ SEFD_{2,pred}}{r_{SNR}^2} = SEFD_{1,obs}\ SEFD_{2,obs} \qquad \text{n for weighting}$$

least-squares adjustment

$$SEFD_{1,2,estimated}$$

estimated SEFD refered to as re-estimated SEFD:

result

output folder
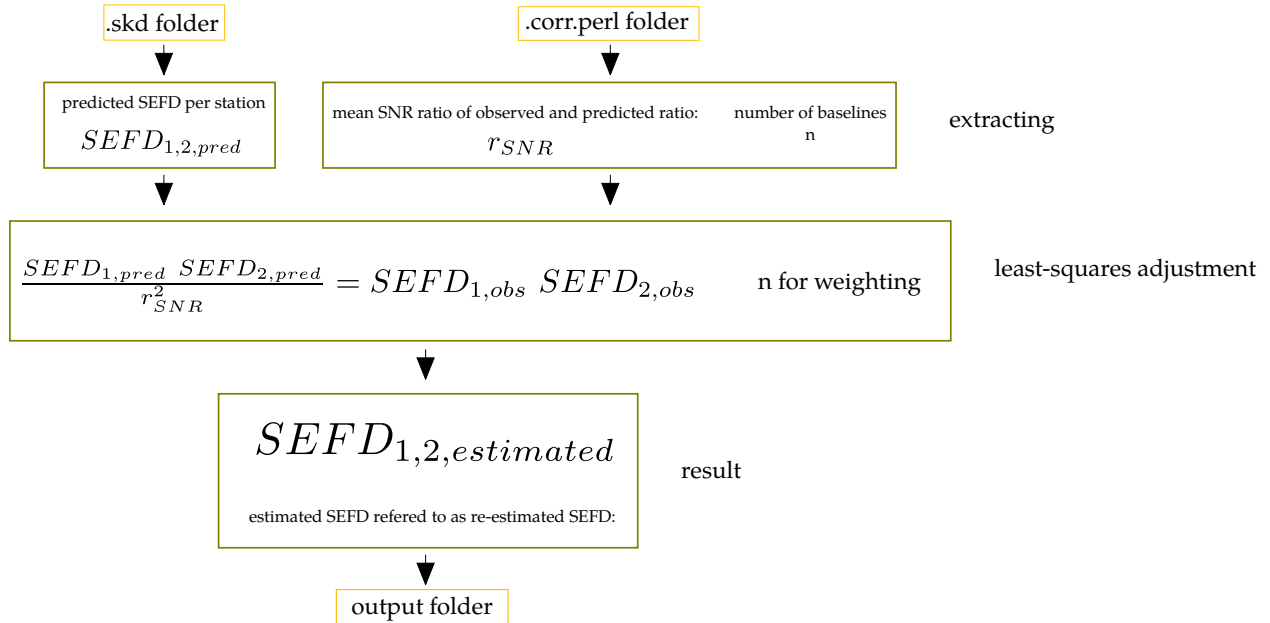
Fig. 6.3: Software architecture of the SEFD re-estimation routine.

One of the characteristics of this MATLAB routine represents the possibility to apply all types of sessions. This means it can be easily used to monitor the AuScope SNR data in the future.

6.1.4   Results of the re-estimation of the SEFD

Considering all sessions since Dec. 2013 for the AuScope VLBI array antennas, one fifth of all are above the predicted (scheduled) SEFDs. From this fifth 80% are due to sessions

later than Feb. 2015. The main reason is the optimistic change of the scheduled SEFD to a higher sensitivity level (lower SEFD). If the re-estimated SEFD falls above the scheduled SEFD, the sensitivity of the antennas was worse than assumed, because the scan length was too short to target the SNR_{min}. In contrast, if the value of the re-estimated SEFD is smaller than the scheduled SEFD, the sensitivity of the antennas was better than assumed, because the scan length was longer than needed.

(a) Hobart X-band

(b) Hobart S-band

Fig. 6.4: Time series of the re-estimated SEFD (orange dots) and scheduled SEFD (gray line) of the X- and S-band for Hobart.

Merge X- and S-band

The AUSTRAL experiments are operated in the X- and S-band. It is convenient to merge the SEFD of both bands to achieve one SEFD, which allows a comparison with geodetic results. Eq. 6.5 shows the merged SEFD. The X-band contributes with $\frac{13}{14}$, whereas the the S-band contributes with $\frac{1}{14}$. For more information see Porcas, R. [2010], Sec. 4.3, respectively.

The $\overline{SEFD}$ of Hobart, Katherine and Yarragadee is shown in Fig. 6.8a to 6.8c. All stations show an increase in $\overline{SEFD}$ over time (December 2013 to July 2015). This may be due to a decrease in the aperture efficiency, because the quality of the antenna surface material decreases. The increase of the $\overline{SEFD}$ is stronger in the S-band than in the X-band. The average session-wise variation of the $\overline{SEFD}$ is about ±900 Jy for Hobart, ±600 Jy for

(a) Katherine X-band

(b) Katherine S-band

Fig. 6.5: Time series of the re-estimated SEFD (orange dots) and scheduled SEFD (gray line) of the X- and S-band for Katherine.
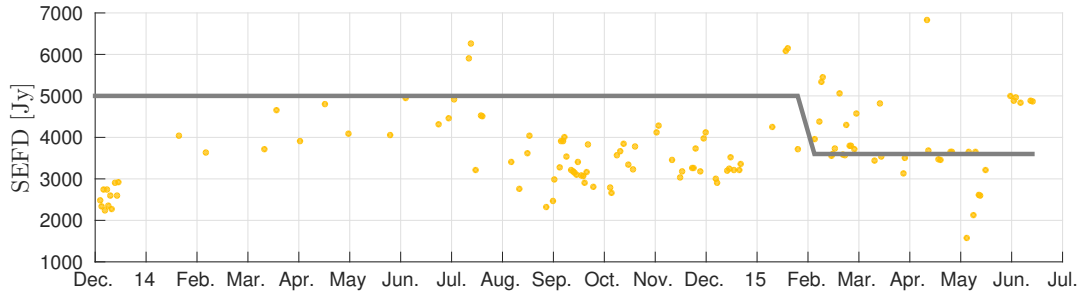
(a) Yarragadee X-band
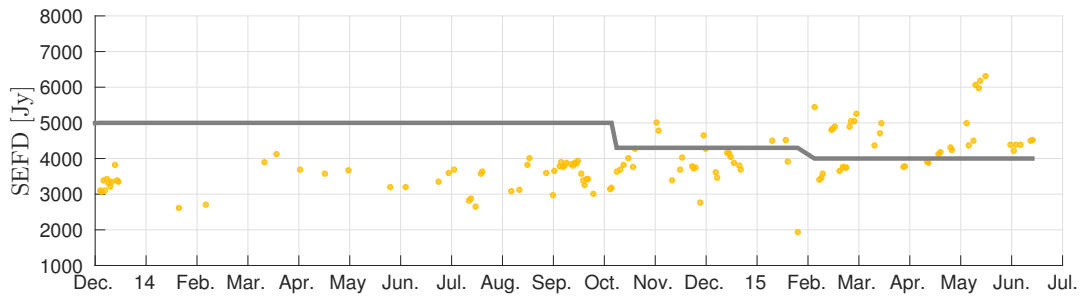
(b) Yarragadee S-band

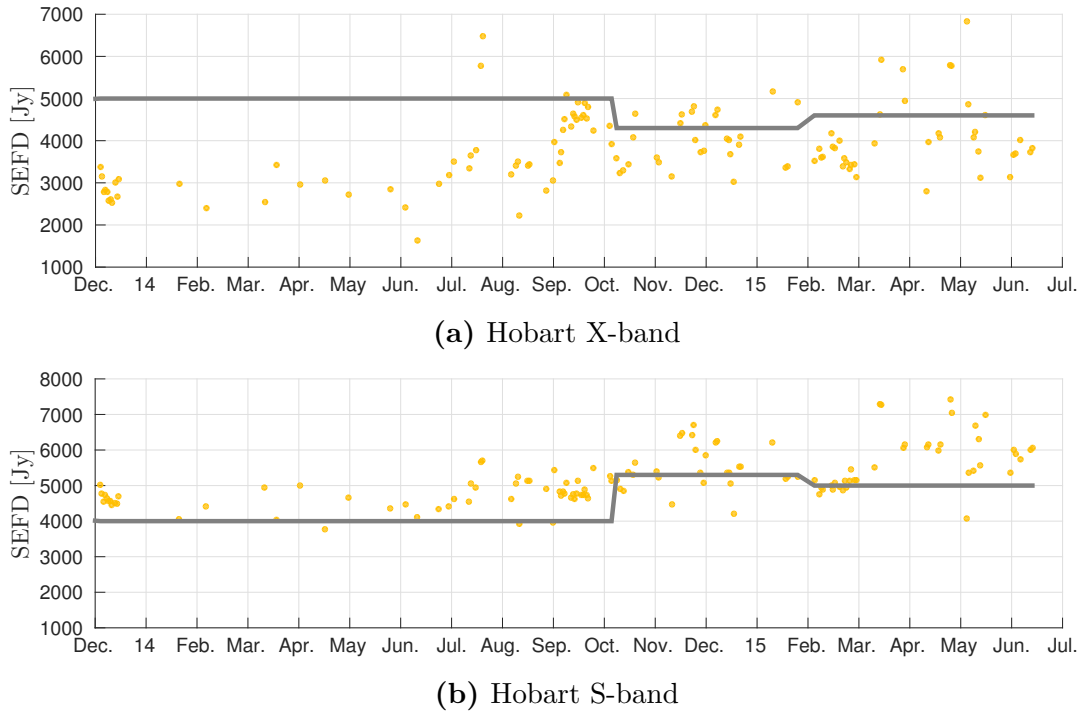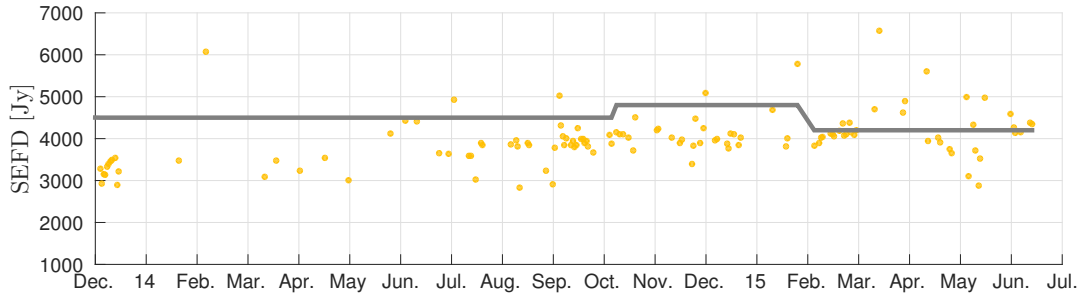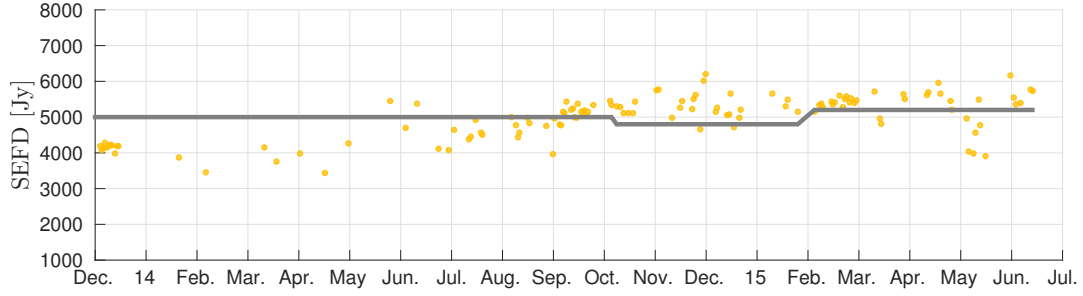**Fig. 6.6:** Time series of the re-estimated SEFD (orange dots) and scheduled SEFD (gray line) of the X- and S-band for Yarragadee.

$$\overline{SEFD} = \frac{12}{13}\,SEFD_X + \frac{1}{13}\,SEFD_S \qquad (6.5)$$

with $\overline{SEFD}$ ... SEFD merged [Jy]
$SEFD_X$ .. SEFD in X-band [Jy]
$SEFD_S$ .. SEFD in S-band [Jy]

Katherine and ±900 Jy for Yarragadee. However, a general assumption of increasing SEFD is inappropriate, because the scatter of the re-estimation dominates. Furthermore, the systematics which can be seen in Figs. 6.8a to 6.8c require further investigations and are not entirely clarified in this work. Weather dependent influences may be a reason. Table 6.2 lists the influences, which might cause the differences of the real observed and scheduled SEFD in theory. The practical aspects of the difference from scheduled to real observed alias source strength, atmospheric conditions, effective scan length and sensitivity has to be considered when analyzing SNR ratios of the AuScope stations.

The source strength of the quasars used in VLBI are subject to variations (see Fig. 6.7). Due to these variations the flux can not be predicted exactly. This means that the source is stronger than expected or sometimes weaker than expected. However this effect should somehow cancel each other out for an entire session. This does not mean that the uncertainties of the source flux per scan can be neglected. In order to create an efficient schedule the source flux has to be known precisely to calculate the optimal scan length, but does not significantly effect the mean SNR of the entire session.

Fig. 6.7: Flux density variability of quasar PKS B1144–379 at X- and S- bands. It is raw data from IVS observations (Shabala et al. [2014])

Atmospheric conditions represent a big topic in the sensitivity analysis. Some of the characteristics, such as the contribution of the daily and yearly temperature signals have already been discussed in prior sections (see Sec. 3.2.1 & 5.4.3). In general the atmospheric contribution is covered by the SEFD 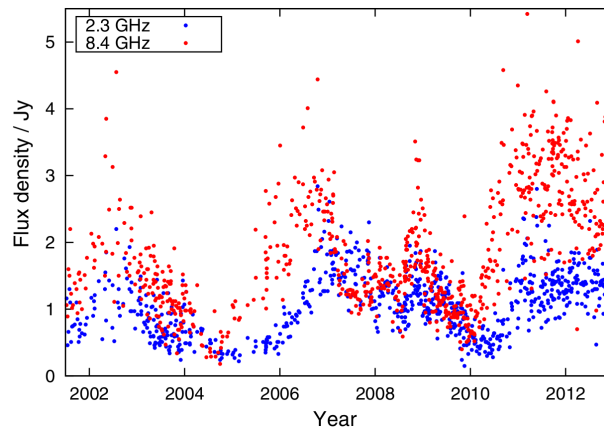values. Fast upcoming and changing weather conditions such as rain falls can degrade the sensitivity within hours, whereas the predicted SEFD in the state of the art VLBI creation are static for session. This means that the scan length or SEFD respectively, have to be adjusted in real time to avoid differences in the predicted to real observed SNR and to create an efficient schedule.

Differences in the scheduled scan length and the real effective scan length (on source time) of an antenna can occur. For example, this happens when calibration steps are executed during the operational observation time. Recording is stopped during these steps and the effective scan length is shorter than expected, hence the SNR is decreased. A check of the effective scan length must be done to provide an optimal observing system.

$\frac{SNR_{obs}}{SNR_{skd}} > 1$	the observed SNR is higher than expected; the scheduled SEFD is too pessimistic; the expected source flux is lower than the observed one; clear sky; low humidity; the effective scan length is higher than expected one
$\frac{SNR_{obs}}{SNR_{skd}} < 1$	the observed SNR is lower than expected; the scheduled SEFD is too optimistic; the expected source flux is higher than the observed one; overcast conditions; the effective scan length is shorter than expected one; unexpected RFI
$\frac{SNR_{obs}}{SNR_{skd}} = 1$	the observed SNR is equal to the scheduled SNR; the expectation of all scheduling parameters are equal in average

Tab. 6.2: Reasons for differences between the observed SNR and the scheduled SNR

6.2   Measured SEFD

The T_{sys} is measured by use of a calibration signal (Eq. 5.1, Sec. 5.5.1 & 5.1). Due to the fact that the $SEFD$ is just the flux equivalent of the T_{sys}, it can be estimated with Eq. 3.15. Therefore it is referred to as the measured SEFD. The required apertures efficiencies (η) were determined by Lovell et al. [2013] with η_X being 64.3% (X-band) and η_S is 59.7% (S-band).

(a) Hobart

(b) Katherine
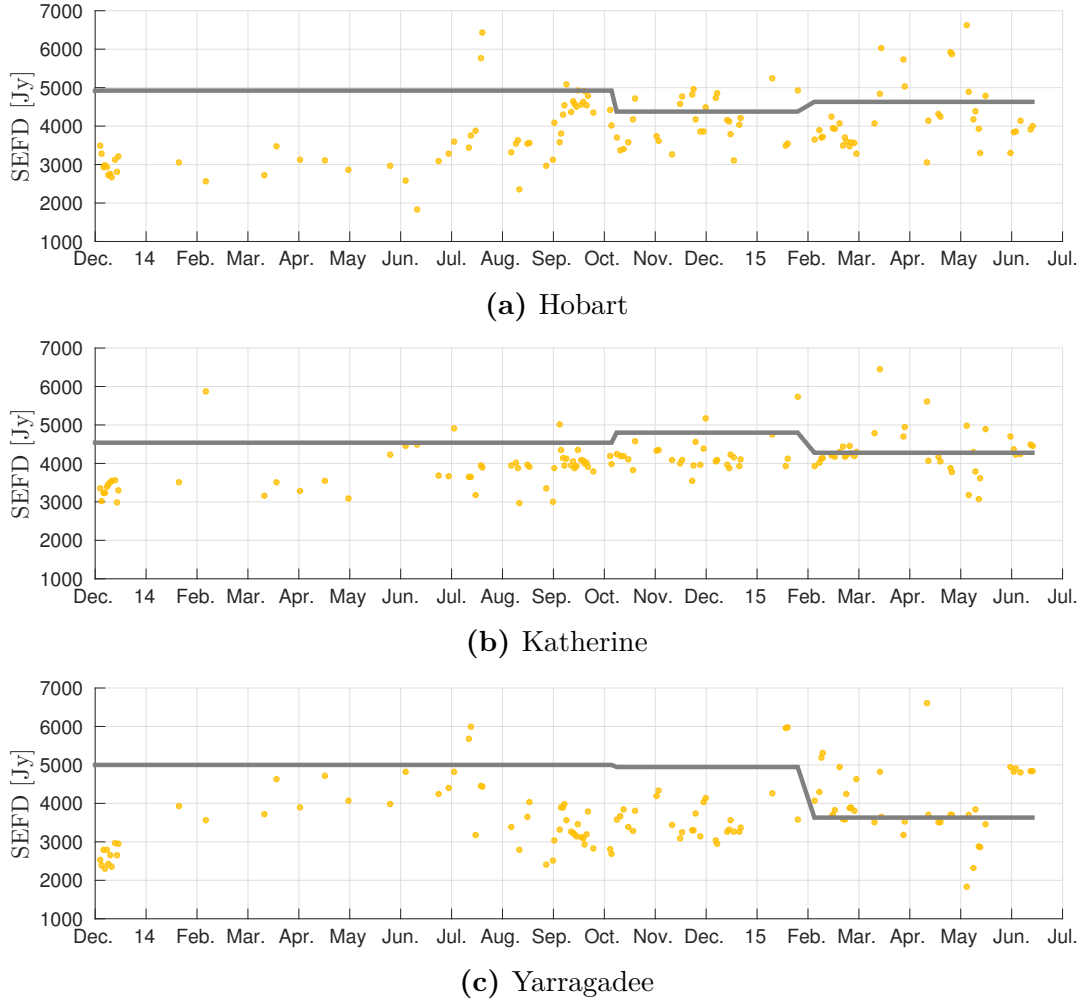
(c) Yarragadee

Fig. 6.8: Merged SEFD (X,S) of Hobart, Katherine and Yarragadee, re-estimated SEFD (orange dots), scheduled SEFD (gray dots)

The used T_{sys} is described in detail in Sec. 5. However, an important characteristic of the measured SEFD should be mentioned: The measured T_{sys} is not consistent between stations, therefore statements about differences in absolute levels of measured SEFDs between stations can not be made.

6.3   Re-estimated SEFD and measured SEFD

In this section the re-estimated SEFD (Sec. 6.1) is compared with the measured SEFD (Sec. 6.2). The measured SEFD is solely based on measurements of the T_{sys}. These measurements are taken per station (single dish physics) and therefore they are not consistent between different stations. Whereas the re-estimated SEFD is based on the observed signal to noise ratios of a VLBI session. All stations contribute to the re-estimated SEFD in a best fit adjustment. This means that the re-estimated SEFD is more reliable due to

the redundancy of the adjustment. The measured SEFD (no information about quality) is dependent on the quality of the calibration signal, which should be examined critically, because of instabilities in the calibration signal producing noise diodes (Sec. 5.5). Fig. 6.9 to Fig. 6.11 show the comparison of re-estimated SEFD and measured SEFD. Hobart shows a low correlation between the times series, in both X- and S-band, probably caused due to the limitation of the quality of the calibration signal. It seems that the variations in the T_{sys} can not be resolved. The measured SEFD of Katherine show a higher correlation with the re-estimated SEFD. The data series of the measured SEFD show a strong scatter, probably caused due to a higher sensitivity of the calibration signal. Offsets are noticed, probably caused by systematics in the calibration signal or a wrong value of the aperture efficiency, whereas the longtime trends are conform. The measured SEFD for the X-band of Yarragadee does not fit the trend of the re-estimated SEFD, whereas the correlation coefficient is higher than in Hobart. The correlation coefficients between measured and re-estimated SEFD are shown in Tab. 6.3 . The overall correlation coefficient is lower than 23% for the X-band and lower than 49% for the S-band. But the continuous campaigns, referred to as a14 and a15, show a high correlation (see Tab. 6.3). This circumstance may be caused due to the timely sessions and maybe the DBBC performed very stable. Another reason may be the unconsidered variation of the source flux, which significantly affects the scan length, but does not have an impact on the measured SEFD during the CONT-like campaigns. Possibly the variation in source flux during the AUSTRAL CONT-like campaigns is infinitesimal and the re-estimated SEFD is not affected and is consistent with the measured SEFD.

	X			S		
	a14	a15	all	a14	a15	all
Hobart	21	58	0	7	62	-15
Katherine	-55	76	-23	97	46	35
Yarragadee	79	74	18	96	94	49

Tab. 6.3: Correlation coefficients in % determined between re-estimated SEFD and measured SEFD

6.3.1   Average difference of the re-estimated SEFD and the measured SEFD

There is a significant offset between the re-estimated SEFD and the measured SEFD in both, the X- and the S-band. The reason might be a bias in the calibration signal of the T_{sys} measurement. To account for this systematics, the average difference between the re-estimated SEFD and the measured SEFD is calculated for the X and the S-band of each

(a) X-band

(b) S-band
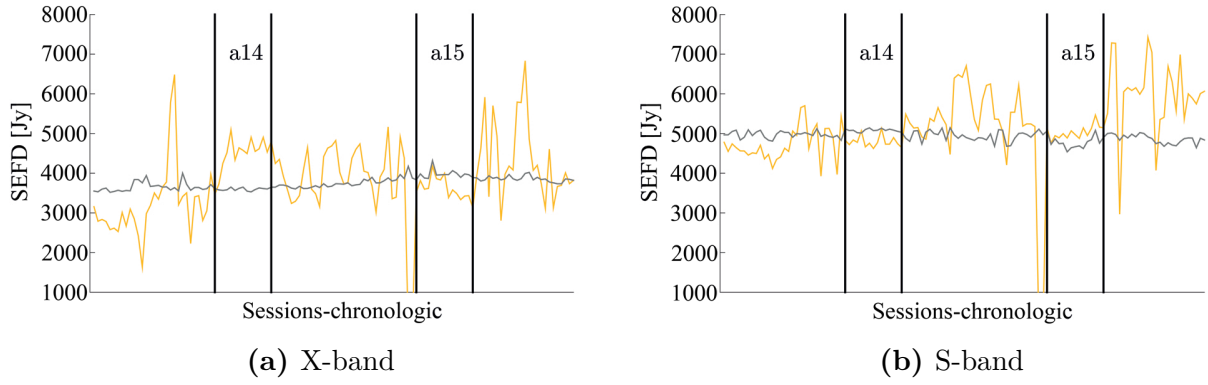
Fig. 6.9: Hobart, re-estimated SEFD (orange line) and measured SEFD (gray line)

(a) X-band

(b) S-band
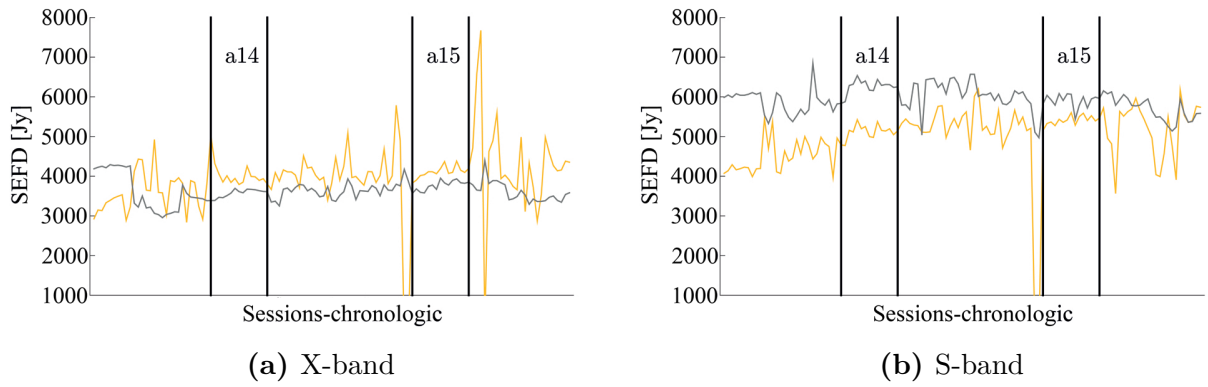
Fig. 6.10: Katherine, re-estimated SEFD (orange line) and measured SEFD (gray line)

(a) X-band

(b) S-band

Fig. 6.11: Yarragadee, re-estimated SEFD (orange line) and measured SEFD (gray line)

antenna. Table 6.4 lists the magnitudes, which will be used to correct the estimated elevation model parameters presented in Sec. 5.4.1.

	X [Jy]	S [Jy]
Hobart	352	203
Katherine	506	-1018
Yarragadee	950	-510

Tab. 6.4: Average difference between the re-estimated SEFD and measured SEFD (based on the T_{sys} measurement) for the X- and the S-band of each antenna.

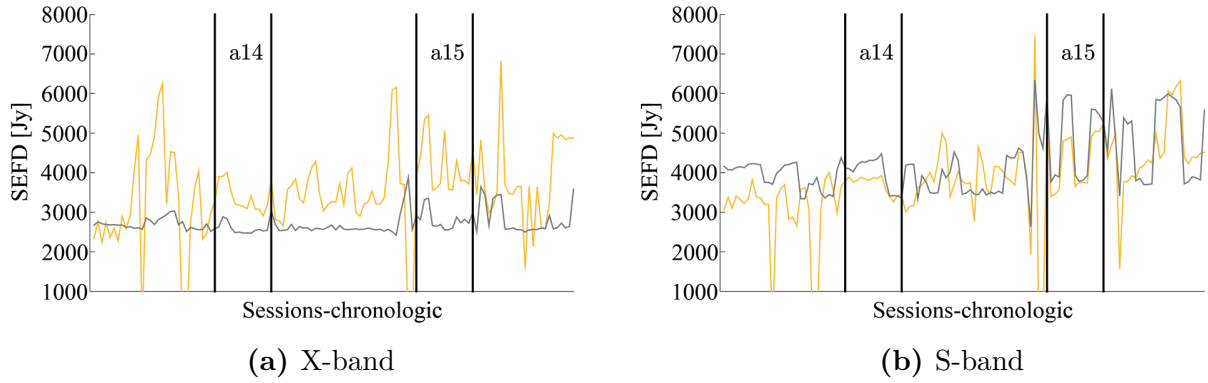## 6.4   Conclusion

The presented method allows the re-estimation of the SEFD based on the mean SNR ratios provided by the correlation report. The re-estimated SEFD can be interpreted as the value, which has to be used to achieve the required SNR.

In this work two completely independent ways of achieving sensitivity parameters are provided. On the one hand there is the re-estimation of the SEFD by use of the correlation reports and on the other hand there is the T_{sys} which can be converted into SEFD. The comparison of the time series of both datasets shows a higher scatter of the re-estimated SEFD. The exact reason of this result is not investigated entirely within this work. The outliers in the data may be caused due to sessions with a low degree of freedom in the estimation process or any kind of antenna problems. A correlation of both time series for timely sessions can be found. This is quite an interesting result, because this shows the impact of changing the schedule configuration and indicates the uncertainties in the schedule parameters. However the exact reason of the low and high correlations periods can not be specified within this work.

Analyzing the high correlation periods from another point of view shows us, that the T_{sys} measurements are consistent with the SEFDs from the correlation report. This means the T_{sys} measurements represent a proper way of providing sensitivity information. The real-time availability (in fact per scan) represents a big advantage of the reliable T_{sys} measurements.

Besides the relative variations of the measured and re-estimated SEFD, the absolute magnitudes have to be scrutinized. As already discussed in Sec. 5, the absolute magnitudes of the T_{sys} measurements must be under critical investigation. The re-estimated SEFDs have the characteristic that they are estimated using the real observed SNR ratios. This means that the T_{sys} values can be corrected to match with the absolute magnitudes of the re-estimated values. With this the corrected T_{sys} measurements are a very reliable representation of the sensitivity in real time of the AuScope array antennas.

Two different ways of obtaining sensitivity parameters are discussed. The re-estimated SEFD and the measured SEFD by use of the T_{sys} measurements. The former is estimated by use of very reliably mean SNR ratios provided per session by the correlation report. The disadvantage of this method is that the mean SNR is an average over the entire session. This means that it is not possible to clarify the impact of a wrong prediction of the source flux, because failures in the prediction can cancel each other out. In future analysis the SNR ratios per scan should be investigated to get an exact idea of the goodness of prediction.

7 Sensitivity and schedule characteristics of the AUS-TRAL sessions

There are different VLBI schedule strategies to achieve different goals, such as geodetic or astronomical aims. Fundamentally, the creation of the schedule is based on the calculation of the on-source scan length to meet the required SNR in order to resolve the received signals precisely in the VLBI-correlator. The scan length is determined by the strength of the source, the sensitivity, the recording rate and the required SNR (Fig. 7.1). The real observed source flux and the real observed sensitivity yield the observed SNR. If the observed and required SNR matches, the measurement precision matches the expectations, otherwise the measurement precision is low or the schedule is inefficient due to too much on source time, which blocks the aim of as many observations per session as possible.
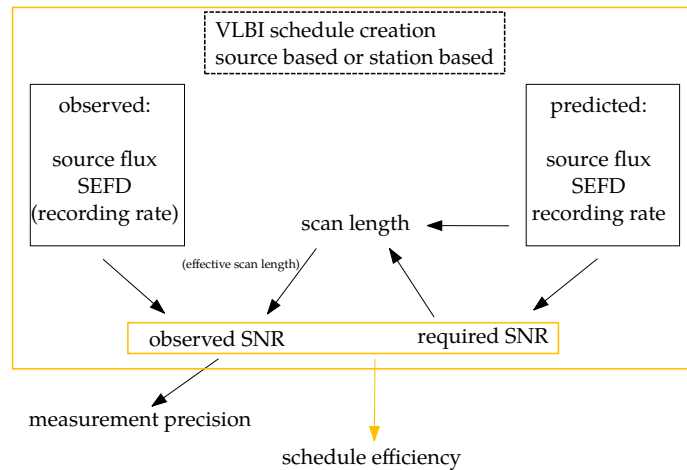

Fig. 7.1: Relations between sensitivity, scan length, SNR, measurement precision and schedule efficiency.

7.1   AUSTRAL scheduling characteristics

The schedules of the AUSTRAL sessions are created in Vienna, Austria, using the Vie_SCHED module (Sun 2014) of the Vienna VLBI Software (VieVS, Böhm et al. [2012]). There are two somewhat contradictory strategies, the creation of a schedule is based on: Station based and source based strategy. The former targets geodetic goals, such as the estimation of precise station coordinates. This is achieved by the elimination of the errors due to the wet part of the troposphere with as many observations as possible and to spread them evenly in different directions (maximization of sky coverage). The source based strategy still has an acceptable sky coverage at each station as well, but focuses on the observation of new and poorly observed sources. In this work, the geodetic sessions are of importance. The scheduling parameters, which are used for the creation of schedules of the AUSTRAL sessions are specified in Tab. 7.1.

SNR_{min}: 20 in X-band, 15 in S-band

minimum Sun distance 4°

source flux stronger than 0.5 Jy

minimum scan length: 20 s

maximum scan length: 200 s

the same source will not be observed twice in 30 min

Tab. 7.1: Parameterization for the creation of a station-based schedule (Mayer et al. [2015]).

7.2   Influence of scheduling parameters on the scan length

The influences of variations in the scheduling parameters on the scan length are discussed in this section. Eq. 3.17 shows the calculation of the scan length, which is used in the state of the art VLBI scheduling packages (Sun [2012] and Gipson [2012]). It is based on following parameters: Source Strength, $SEFD_{1,2}$ of station 1 and station 2, recording rate and the required SNR.

7.2.1   Source strength and SEFD

The strength of the source controls the influence of the variations in the SEFD and therefore the source must be chosen carefully. A strong source decreases the length of the scan and the influence of variations in the SEFD are relatively small, whereas the influence of variations in the SEFD is relatively high for a weak source. Using a high sensitivity (with respect to

AUSTRAL sessions) with SEFD 3600, the recording rate is set to 1 Gbps, the minimum SNR is specified as 20, hence the required scan length is 7 s for a very strong source with 1.5 Jy. Using the same source strength, but a low sensitivity with SEFD 5200, the required scan length is 14 s. Using a weak source with 0.5 Jy the required scan length is 64 s for a high sensitivity (3600 Jy) and 132 s for a low sensitivity with 5200 Jy, respectively. Considering the range of the source fluxes of the radio sources used in the AUSTRAL sessions (0.5 to 2 Jy) and the range of the possible SEFDs (3600 to 5200 Jy), a stronger influence on the scan length can be found for variations in the source flux compared to the variations of the SEFD. However, in both cases the scan length increases quadratically.
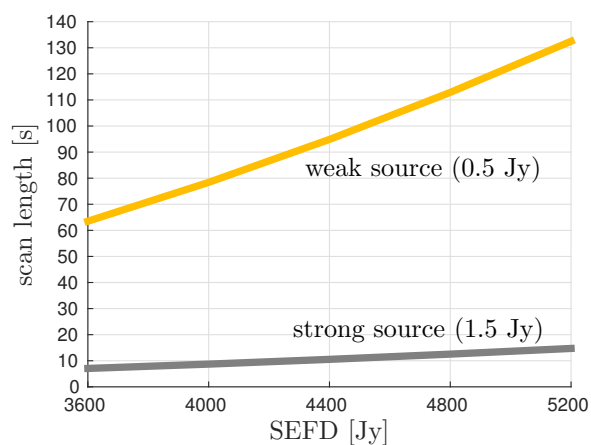

Fig. 7.2: Influence of SEFD and source flux on the scan length

Fig. 7.2 shows the scan length as a function of SEFD for a weak source and a strong source. The weaker the source the higher is the impact of the variations in the sensitivity. Considering the e.g. big jumps of 3600 to 4800 Jy in the re-estimated sensitivity of Yarragadee during the a15 sessions in Feb. 2015 shown in Fig. 6.8c, the scan length varies between 63 s and 132 s to achieve the required minimum SNR. Whereas the scan length of strong sources varies between 7 and 14 s. This means, that care has to be taken when using weak sources in VLBI, if the sensitivity of the antenna is subject to high variations.

Noise signals due to the atmospheric temperature and their impact on the scan length

The influence of the atmosphere on the sensitivity is not investigated completely in this work. However, a significant daily influence can be found for some sessions (see Fig. 5.14) and a yearly noise signal might be interpreted in Fig. 5.15a. The amplitudes are quantified with 10 K of the daily signal and 5 K for the yearly signal, with offsets of 90 K and 95 K,

respectively. Fig. 7.3 shows a simulation of the influence of the atmospheric noise signals. The scan length varies between 12 and 18 s due to a noise influence of the atmospheric temperature, when observing a source with 1 Jy and targeting a SNR_{min} of 20 with a 1 Gbps recording system. In general the influence decreases strongly (for all kind of parameters, not only for SEFD) when using higher recording rates and is shown additionally in this figure. Considering a yearly temperature signal, the scan length varies betweeen 14 and 18 s.
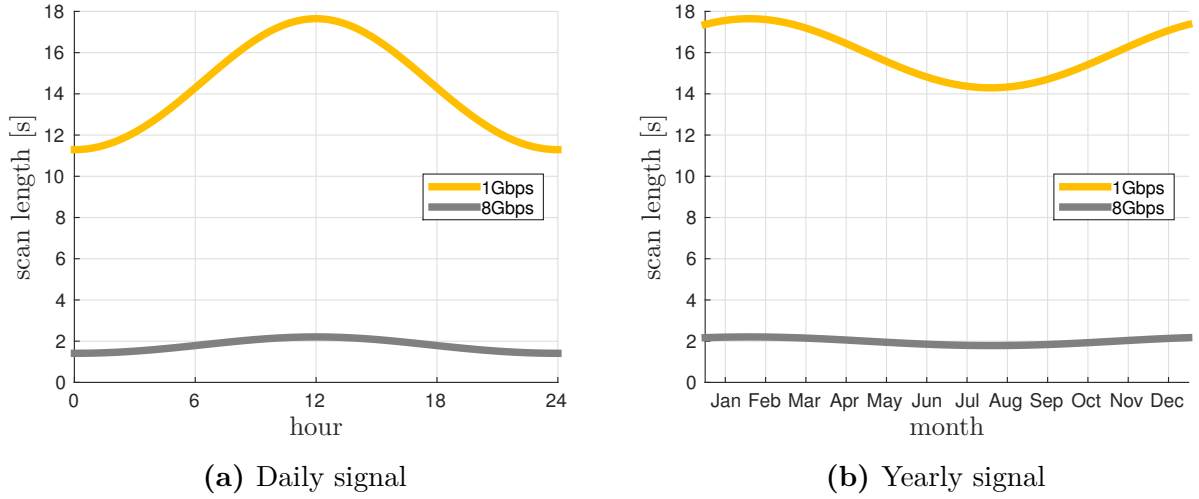

(a) Daily signal   **(b)** Yearly signal

Fig. 7.3: This figure shows the influence of the variations in the SEFD due to the daily and yearly atmospheric noise contribution. When observing a source with a strength of 1 Jy and 1 Gbps recording rate, the scan length varies between 12 and 18 s, due to the atmospheric influence on the receiver sensitivity. The yearly contribution is less when considering a variation in the sensitivity with an amplitude of 5 K. Additionally, the increased performance when upgrading to a 8 Gbps recording system is shown.

7.2.2   Recording rate

The choice of the recording rate has a huge impact on the scan length calculation (and even on the position accuracy, see Plank et al. [2015]). A higher recording rate reduces the length of the scan and reduces the influence of variations in the sensitivity, which can be seen in Fig. 7.3. However, the installation of a higher recording system at the site and the demand for the increasing memory capacity is a challenging task and can not be achieved easily. The AuScope receiving system will be upgraded to 2 Gbps in the near future.

7.2.3   Required SNR

The choice of the required SNR (SNR_{min}) is based on the determination through eq. 8.1. The higher the SNR the lower (better) is the measurement error of the delay observation. The SNR_{min} has not been chosen too high (good) for efficiency reasons, because at some stage

the contribution of the SNR on the scan length is too high compared to the high precision of the measurement. The SNR_{min} will be set to 20 for the S-band for the AuScope antennas, because scans were lost due to short integration time.

7.3   SEFD setting in the state of the art VLBI scheduling packages

The state of the art VLBI scheduling packages (Gipson [2012] & Sun [2012]) use station specific parameters from the equip.cat file, provided by the IVS for the creation of schedules.[2] The SEFD of the X- and the S-band is specified and an elevation function can be added optionally. Sec. 7.3.1 discusses the magnitudes of the X- and S-band SEFD values for the AuScope array antennas. Sec. 7.3.2 discusses and provides magnitudes for the elevation function coefficients, which can be added optionally in the creation of schedules for the AuScope array in the future.

7.3.1   System equivalent flux density in the X- and the S-band

The SEFD of the AUSTRAL sessions was adjusted several times in the past and lies in the range of 3600 to 5200 Jy for the X-band and 4000 to 5200 Jy in the S-band, respectively. The real observed SEFDs for the AuScope array antennas are scattered, neglecting some outliers, in a range between 3000 to 5000 Jy for the X-band and 3000 to 6000 Jy for the S-band, respectively. A perfect match of scheduled and observed SNR can not be achieved in practice, due to the high dispersion in the real observed SEFDs (see Sec. 6.1.4). The optimistic shift to lower SEFDs in the creation of the schedule in the near past, has led to some lower (worse) SNRs and even to a loss of scans. Tab. 7.2 shows the new SEFDs for the X- and the S-band, which are recommended in this work. The magnitudes are obtained by the visual interpretation of the figures 6.4, 6.8 and 6.6.

	old (X/S)	new (X/S)
HOBART12	4600/5000	4600/6000
KATH12M	4200/5200	4600/5600
YARRA12M	3600/4000	3600/4500

Tab. 7.2: Recommended SEFD in Jy of the X- and S-band for creation of the schedule. The old SEFD values refer to the latest SEFDs used in the creation of the AUSTRAL schedules.

---

[2](ftp://gemini.gsfc.nasa.gov/pub/sked/catalogs/)

7.3.2   Elevation function

The sensitivities of the AuScope VLBI antennas show a significant elevation dependency (Sec. 5.4.1). The lower the elevation of the pointing direction the higher is the noise load, due to the increasing thickness of the atmosphere. The elevation dependency is modeled using a factorized inverse sinus function $a + \frac{b}{sin(elev)}$, where the factor b simply represents the thickness of the atmosphere. All channels of 128 AUSTRAL sessions since Dec. 2013 of each antenna are analyzed in a least-squares adjustment to obtain the most probable factor of each antenna for the X- and S-band, respectively. The time series show a negligible stable scatter around the estimated mean factor (Fig. 7.4 to Fig. 7.6).
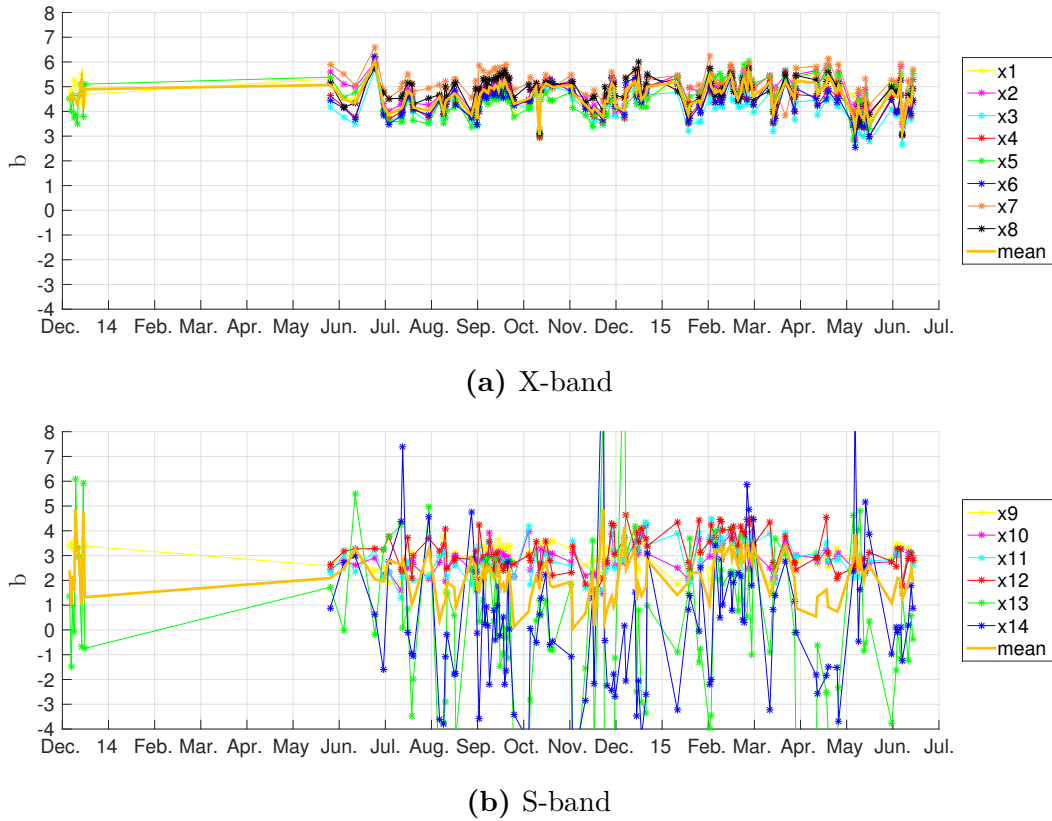

(a) X-band

(b) S-band

Fig. 7.4: Time series of the factor b of the X-band and S-band of Hobart

The residuals of the model approach are free of systematics for elevations higher than $10°$. Ground spillover leads to outlier measurements at low elevations. These values are not treated as outliers and therefore the residuals are affected systematically for elevations lower than $10°$ (see Fig. 5.12). A detailed discussion of the quality the of elevation model is presented in Sec. 5.4.2.
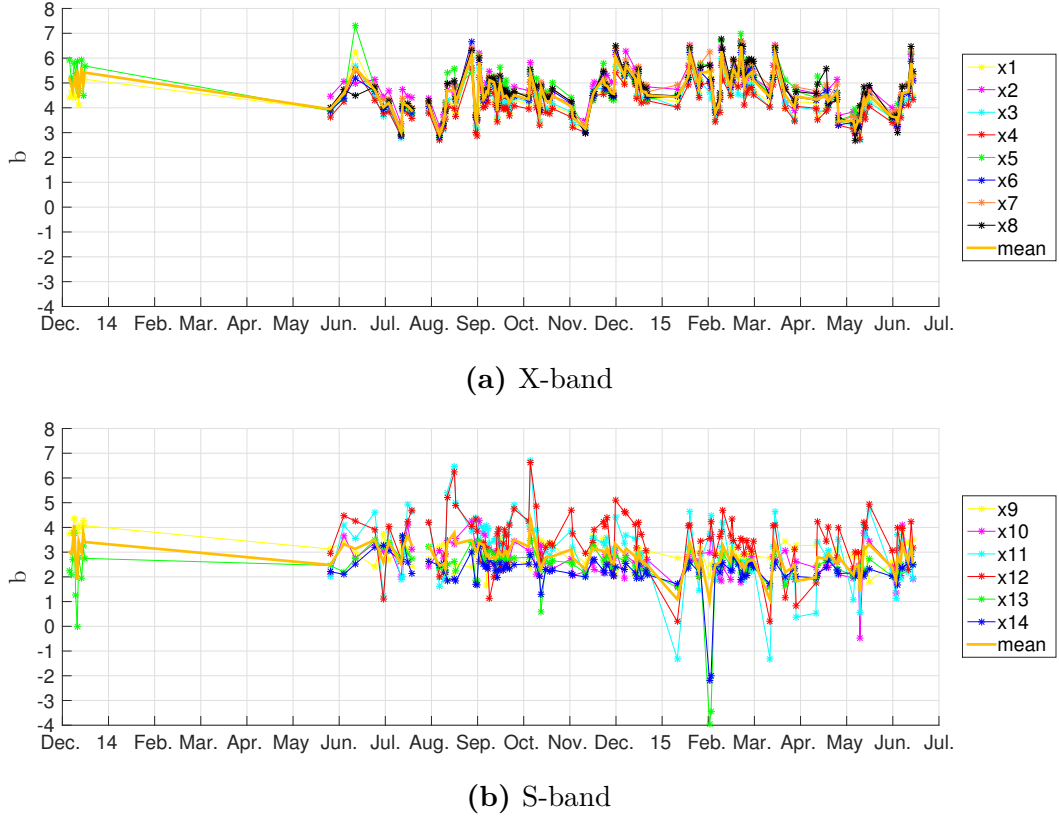
(a) X-band

(b) S-band

Fig. 7.5: Time series of the factor b of the X-band and S-band of Katherine

The parametrization used in the equip.cat file are based on eq. 7.1. The coefficients c_i are the parameters, which can be written into the equip.cat file.

$$f(elev) = \sum_{i=0}^{n} \frac{c_i}{(\sin(elev)^y)^i} \tag{7.1}$$

with n ... usually 0 to 1
        y ... power
        $c_{0,1}$ ... coefficient

$f(elev)$ is the mapping function, which is used to scale the SEFD in zenith direction ($SEFD_{zenith}$) to yield the SEFD for a certain elevation ($SEFD(elev)$, eq. 7.2). The conver-

$$SEFD(elev) = SEFD_{zenith} \; f(elev) \tag{7.2}$$

sion of the elevation model (a,b) used in this work to the IVS standard is shown in eq. 7.3.

(a) X-band

(b) S-band

Fig. 7.6: Time series of the factor b of the X-band and S-band of Yarragadee

$$c_0 = \frac{a + b - b}{a + b} \quad , \quad c_1 = \frac{b}{a + b} \tag{7.3}$$

with $c_{0,1}$ . . . coefficient

The T_{sys} measurements, which are used to estimate the model parameters (a,b) are biased by systematics in the calibration signal. The comparison between those and the re-estimated SEFDs yield offsets, which are used to correct the model parameters. In fact, the parameter a represents the absolute level of the T_{sys} measurement. Therefore, the correction term (δa) is simply added to a (eq. 7.4).

$$a_{corr} = a + \delta a \tag{7.4}$$

b will not be corrected, because the T_{sys} measurements are only biased. The relative variation, such as the elevation dependent contribution, is correct. The corrected magnitudes of the parameter $a + b$ are shown in table 7.3 and they are used to calculate the coefficients c_0 and

67

c_1 with eq. 7.3 and can be included in the equip.cat file.

	Hb	Ke	Yg
X	100	103	87
S	117	89	95

Tab. 7.3: Corrected magnitudes of the T_{sys}^{zenith} $(a+b)$ in K

The magnitudes of c_0 and c_1 are listed in Tab. 7.4 and 7.5.

	Hb	Ke	Yg
X	0.956	0.958	0.971
S	0.975	0.970	0.978

Tab. 7.4: Coefficient c_0

	Hb	Ke	Yg
X	0.044	0.042	0.029
S	0.025	0.030	0.022

Tab. 7.5: Coefficient c_1

Tab. 7.6 lists the magnitude of the mapping function for each side for the X- and the S-band. The SEFD at an elevation of 5° is increased by a factor of 1.46 for the X-band in Hobart. Using a SEFD of 4600 Jy, hence the SEFD at 5° is 6716 Jy.

	Hb	Ke	Yg
X	1.46	1.44	1.30
S	1.26	1.31	1.23

Tab. 7.6: Mapping function f at 5° elevation

7.3.3   Expected performance by use of an elevation function in the creation of a schedule

The received noise increases significantly at low elevation. If this impact is not considered, the SNR is low and the measurement error will increase. But the measurement error is used to weight the observation in the VLBI analysis. This means, that due to the low precision, observations are weighted weakly and the relative number of observations decreases at low elevation. This relative reduction increases the highly unwanted correlation of the design parameters, which degrade the precision of the station coordinates. There could be even

a loss of observations at low elevation due to a bad SNR, because the VLBI correlator is not able to resolve the signals. Considering a perfect mean match of observed SNR and scheduled SNR over all scans of a session, but without using an elevation function, the SNR in zenith direction is high and the SNR at low elevation is small, but in average the session is matched perfectly. Introducing an elevation function in the creation of the schedule will increase the measurement precision for observation at low elevation and will increase the session performance in terms of efficiency, because the observations in zenith direction are not observed too long.

The SEFD for X-and S-band which can be set in the equip.cat file represent the sensitivity in zenith direction. The SEFD values of the AuScope array were selected by interpretation of the mean SNR ratios of observed and predicted SNR. A perfect mean match is achieved by an inefficient high SEFD in zenith direction and an insufficient SEFD at low elevation. In average the ratio results in a perfect match. Applying a mapping function yields perfectly matched SNR ratios at each elevation (see Fig. 7.7). By usage of the elevation function and the present SEFD in the X- and S-band, the mean SNR ratio is expected to increase. The SEFD of the AuScope antennas should be monitored to examine this expectation and to adjust in case.
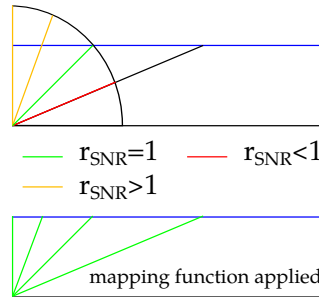

Fig. 7.7: Applying a mapping function in the creation of schedules yields optimal SNRs for each elevation.

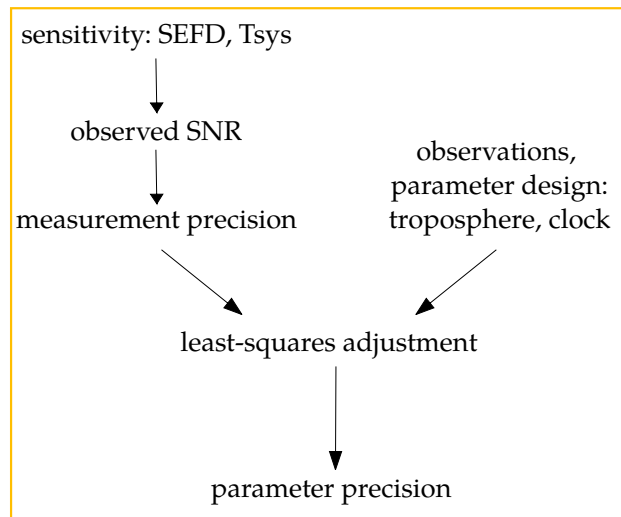# 8 Impact of the sensitivity on the VLBI session performance

sensitivity: SEFD, Tsys

observed SNR

observations,
parameter design:
troposphere, clock

measurement precision

least-squares adjustment

parameter precision

Fig. 8.1: The role of the sensitivity in the VLBI analysis.

The measurement error σ_τ depends on the sensitivity of the antennas, or to be more precise on the SNR of the antennas (Eq. 2.3). This is the level, where the sensitivity influences the geodetic VLBI session performance. The impact of the measurement error is considered to be relatively small compared with the impact of the model errors in the analysis, such as the troposphere and the clock. Pany et al. [2011] pointed out that the dominating stochastic error contribution comes from the wet component of the troposphere and that the VLBI session performance depends primarily on how well it can be modeled. Sec. 8.1 specifies the processing environment of the VLBI analysis, Sec. 8.1 examines the session performance from a statistical point of view and Sec. 8.3 compares the sensitivity with the VLBI session performance.

8.1   Processing AUSTRAL sessions

The AUSTRAL sessions are processed with the Vienna VLBI Software (VieVS). VieVS is being developed at the Institute of Geodesy and Geophysics in Vienna taking into consideration all present and future VGOS requirements. It is equipped with the most recent models recommended by the IERS conventions. First comparisons with other VLBI software packages show a very good agreement (VieVS, Böhm et al. [2012]). In this work version 2.2 (released in 2015) is used. The parametrization is set by default and kept for all sessions.

8.1.1   Clock breaks

At stations may occur clock breaks. These are discontinuities ('jumps') at the station clocks, which can degrade the estimates. VieVS offers a handy tool, which is used in this work, to properly model these errors using the first-solution residuals to identify the clock breaks.

8.1.2   Outliers

Outliers are identified using a 'simple' outlier test provided by VieVS. It sets observations as outliers which have larger residuals than $c\ m0$ where c is a user-definable number (set to 5 in this work) and $m0$ is the a posteriori standard deviation of unit weight.

8.2   VLBI session performance: The variance factor

The variance factor σ_0^2 scales the cofactors to calculate the covariances (Eq. 8.1).

$$\Sigma_{\tau\tau} = \sigma_0^2\ Q_{\tau\tau} \tag{8.1}$$

with $\Sigma_{\tau\tau}$ . . . covariance matrix of the observations
          $Q_{\tau\tau}$ . . . cofactor matrix of the observations

The covariance matrix is used to weight the observations.

$$P = Q_{\tau\tau}^{-1} \tag{8.2}$$

with P . . . weight matrix

$Q_{\tau\tau}$ shows the relative precision of the observations, whereas Q_{xx} shows the relative precision of the unknown parameters. The matrix A contains the information of the model in the least-squares adjustment and is necessary to obtain Q_{xx} (Eq. 8.3). This means that any kind of model errors influence the precision of the unknowns, such as limitations in the model of the atmosphere.

$$Q_{xx} = (A^T P A)^{-1} \tag{8.3}$$

In order to obtain the absolute precision of the unknowns Σ_{xx}, Q_{xx} (e.q. 8.5), has to be scaled with the variance factor a posteriori $\hat{\sigma}_0^2$. The latter can be derived by estimating the variance of the weighted residuals (e.q. 8.4).

$$\hat{\sigma}_0^2 = \frac{res^T P \ res}{n - u} \tag{8.4}$$

with n ... number of observations
         u ... number of unkowns

$$\Sigma_{xx} = \hat{\sigma}_0^2 \ Q_{xx} \tag{8.5}$$

The residuals res are the difference between the real observations τ and the estimated ones (Eq. 8.6).

$$res = (A Q_{xx} A^T P - I) \ \tau \tag{8.6}$$

The variance factor a posteriori is used to describe the session performance because it is estimated per session and it is a measure of the measurement precision. However, this applies only if the design is correct.

8.3   Results and Conclusion

The re-estimated SEFD (see Sec. 6) and the variance factor of the VLBI analysis is used to compare the sensitivity of an antenna with the VLBI session performance. Fig. 8.2 shows

the time series of the sensitivity of Hobart and compares it with the variance factor. No dependency can be found. The systematics in the session performance are not caused by the sensitivity, SNR respectively. This result agrees with the simulations of Pany et al. [2011]. The correlations of the other stations are shown in Fig. 8.3 and does not show any dependency between the sensitivity and the session performance either. Other influences have to be considered in order to discuss the systematics in the time series of the variance factor. Of course the analysis parameters, for e.g. troposphere and clocks play a big role. Additionally different approaches in the schedule creation can affect the quality of the session performance. Furthermore, an unexpected loss of stations during a session can have a serious influence on the reliability of a session, overall with respect to the small AUSTRAL network.
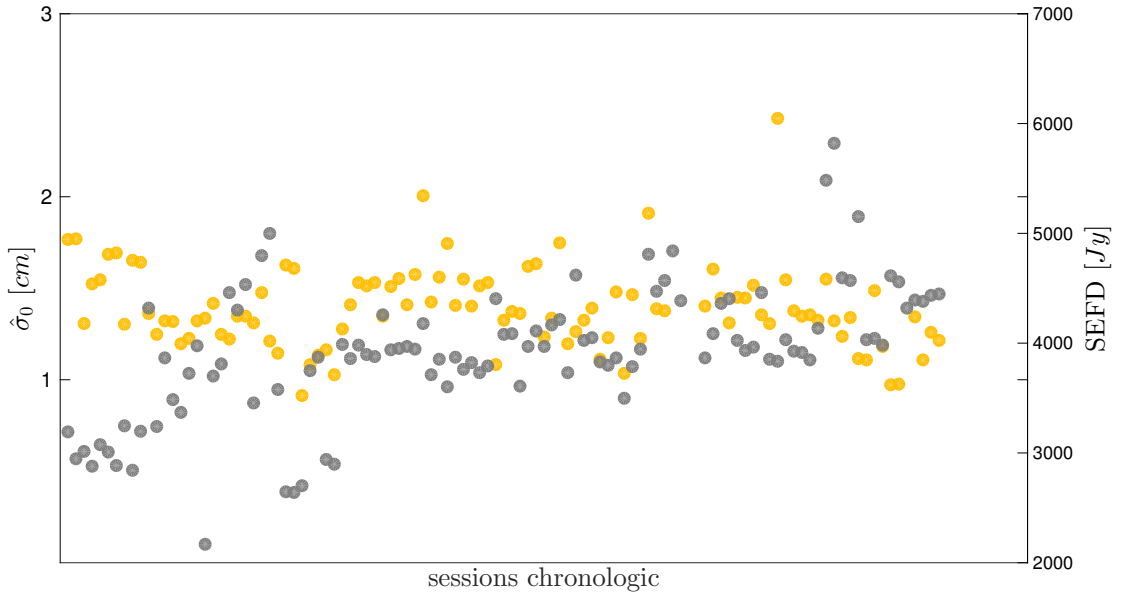
Fig. 8.2: Time series of the variance factor σ_0 (orange dots) and of the SEFD (gray dots) of Hobart. They do not show any correlation.
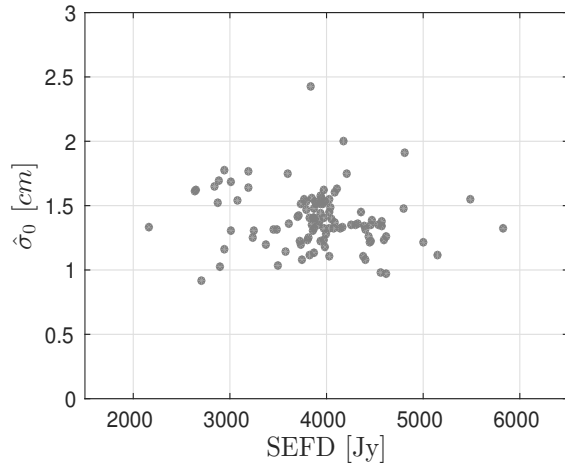
(a) Hobart
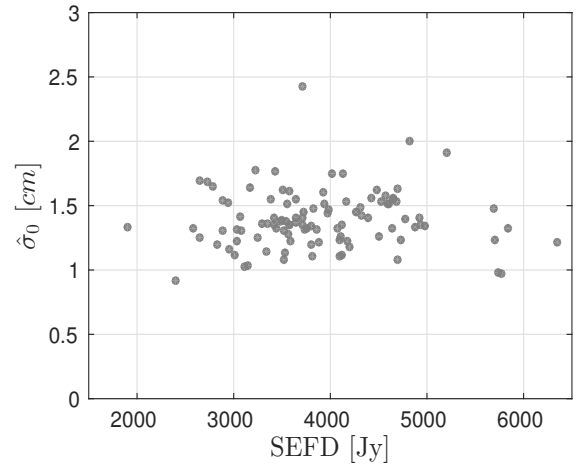
(b) Katherine
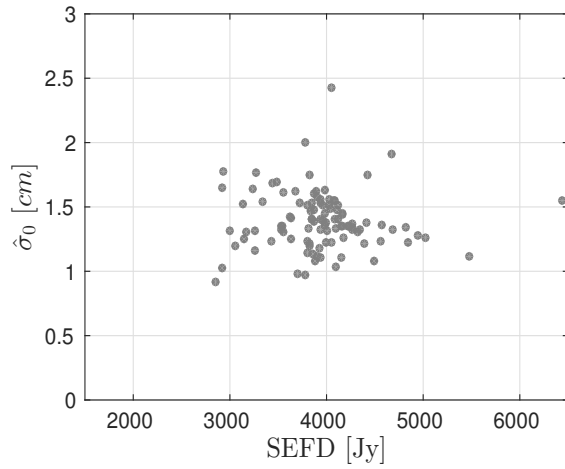
(c) Yarragadee

Fig. 8.3: Correlation between SEFD (x-axis) and the variance factor (y-axis) for Hobart, Katherine and Yarragadee. The X- and S-band is merged with Eq. 6.5. A correlation can not be found.

9 Conclusions, future work, and perspectives

9.1 Conclusion

The sensitivity of the AuScope antennas was examined on the basis of 130 AUSTRAL sessions. The system temperature (T_{sys}) and the system equivalent flux density (SEFD) were analyzed for these sessions in order to determine the sensitivity performance.

The T_{sys} is measured per scan at each site independently and for all receiver channels separately by the injection of a calibration signal. Systematics in the T_{sys} measurements were found because the calibration signal is affected by errors of the noise diodes. The absolute magnitudes of the T_{sys} measurements must be under critical examination due to these errors. Relative variations in the T_{sys} are reliable, only the antenna at Yarragadee shows unexpected systematics even for relative variations.

The correlation report, which is generated after a VLBI session, provides a mean SNR ratio between the scheduled SNR and real observed SNR per session and per baseline. The fundamental relation between SNR and SEFD per site was used to re-estimate *the real observed SEFD* per site and per session. A comparison between expected and real observed SEFD showes a high scatter of the real observed SEFD and points out the difficulties of a perfect prediction of the sensitivity of a VLBI antenna.

Both the T_{sys} and the SEFD characterize the sensitivity of a VLBI antenna. The T_{sys} can be easily converted to the flux equivalent (SEFD) and vice versa by: $SEFD\ A_{eff} = 2\ k\ T_{sys}$, with the effective antenna area A_{eff} and the Boltzmann constant k. Due to the higher reliability, the absolute magnitudes of the re-estimated SEFD were used to correct the T_{sys} measurements. This means that reliable sensitivity parameters were estimated per antenna

and per scan.

The sensitivity determines the length of a scan in a VLBI session. Any variations in the sensitivity cause variations in the scan length. If such a variation is not considered in the creation of a schedule, the required SNR can not be achieved. On the one hand, the sensitivity can be better than predicted and the source is observed too long, which blocks the aim of a high number of observations per session. On the other hand, the sensitivity is worse than predicted and the measurement error increases due to a bad SNR. The elevation of the pointing direction of the VLBI antenna causes such a variation in sensitivity. The sensitivity increases systematically at low elevation. This work determined and provided a mapping function to account for this systematics with coefficients for each side of the AuScope array. The coefficients are reliable for the 12m dish in Hobart and in Katherine. The values for the 12m dish in Yarragadee must be reviewed critically because of errors in the calibration signal of the T_{sys} measurement. However, the calculated coefficients can be used in the creation of schedules for the AuScope array in the future. An improved precision on the observation level (VLBI delay τ) is expected. Additionally, low measurement errors of the receiving system will make it more efficient to identify systematic errors of the VLBI system and unmodeled errors stemming from the atmosphere.

A comparison shows that there is no influence of the sensitivity on the VLBI session performance (variance factor). Errors in the design parameters, such as the troposphere, dominate the VLBI session performance.

9.2 Future Work

Examination of the impact of the sensitivity on the observation precision can be subject to future work. Fig. 9.1 shows the formal error of τ for session a1501 for the baseline Hobart and Katherine. High formal errors might be due to low elevation at both sites. A daily signal may be interpreted, which might occur due to the daily temperature dependent atmospheric noise contribution. The application of a mapping function in the creation of the schedule should reduce the formal error. A correction due to the daily signal may increase the precision of σ_τ as well, but can not be applied easily in the state of the art VLBI scheduling packages. All these corrections can bring us closer to the VGOS goal of 4 [ps] of the formal error.

A detailed investigation of the T_{sys} showed that Hobart and Katherine provide very reliable
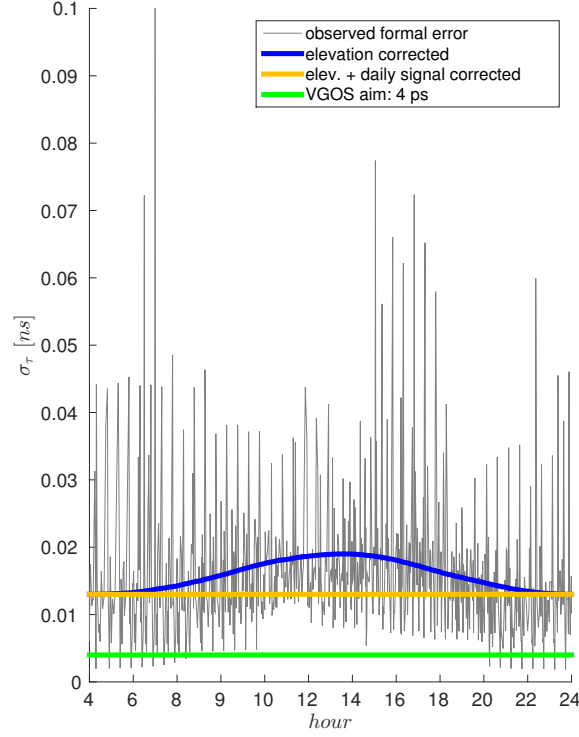
Fig. 9.1: Time series of the observed formal error of τ (σ_τ) per scan of baseline Hobart and Katherine for the AUSTRAL session a1501. The data is extracted from NGS file.

relative T_{sys} measurements during the session. Due to the fact that these measurements can be achieved in real-time via the log-files, the T_{sys} can be used to determine the sensitivity of each antenna per scan in real time. This information can be accessed to optimize the schedule in real time: *Dynamic scheduling.*

A   Part of a correlation report: corr.perl

```
+HEADER
CORREL    CRTN
DATABASE 15JUN13XA
SESSNAME A1522
UTSTART  1900
DURATION 24
DOY      164-165
CORRTIME 2015/09/26 2015/09/27
CORRPASS 1
EXPORT   DONE


+SUMMARY
Qcode       % of Total   % of Correlated
scans          scans


5-9           95%              -
0             2%               -
4-1,A-H,N      3%              -
Removed        -               -


+CORRELATOR_NOTES

+STATION_NOTES

HART15M  (Ht/g): Manual phasecal. Ok.

HOBART12 (Hb/L): Manual phasecal. Small clock breaks noted at 0230 and
0753

KATH12M  (Ke/i): Manual phasecal. Small clock breaks noted at 0048, 0239,
0328, 1015 and 1343.

WARK12M  (Ww/W): Manual phasecal. Ok.

YARRA12M (Yg/e): Manual phasecal. Ok.

+DROP_CHANNELS
Ht
Hb
Ke
Ww
Yg

+SNR_RATIOS

MEAN RATIOS = Observed SNR / Predicted SNR  for exp no. 1366

...by baseline, over all sources:

bl    X    n      S     n

Lg    0.92  304    0.92  283
gi    0.88  320    1.05  312
gW    0.86  177    1.00  159
ge    0.81  509    0.97  493
Li    1.03  832    0.85  831
LW    1.24  807    0.93  805
Le    0.88  708    0.84  710
iW    0.99  745    0.92  737
ie    0.90  763    0.93  764
We    0.82  564    0.90  557
```

B Correlation between channels
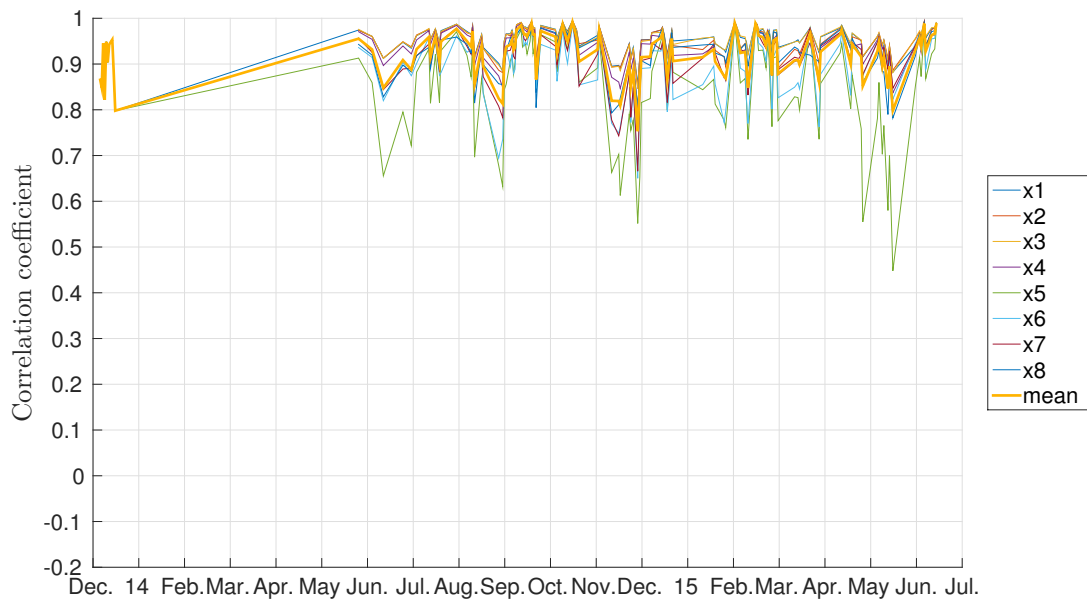
(a) X-band
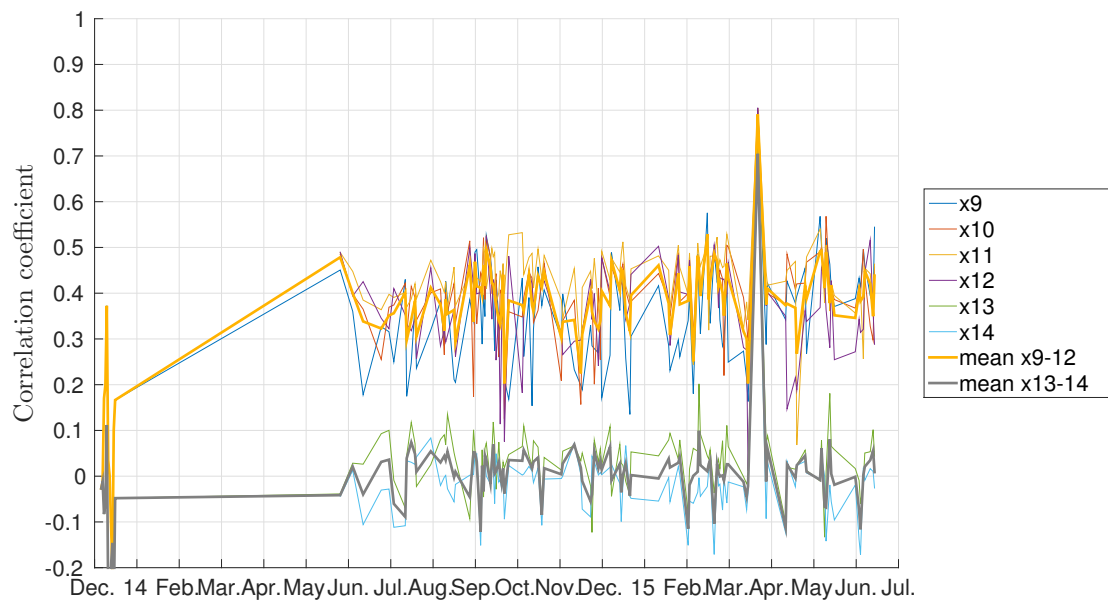
(b) S-band

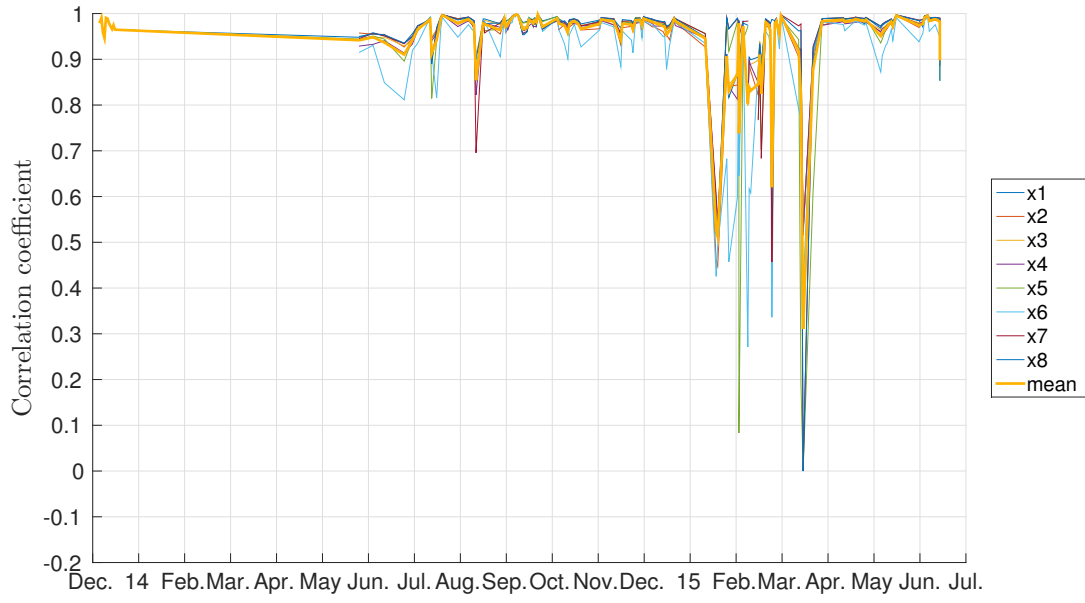**Fig. B.1:** Hobart, time series of the correlation coefficient (X-band and S-band)
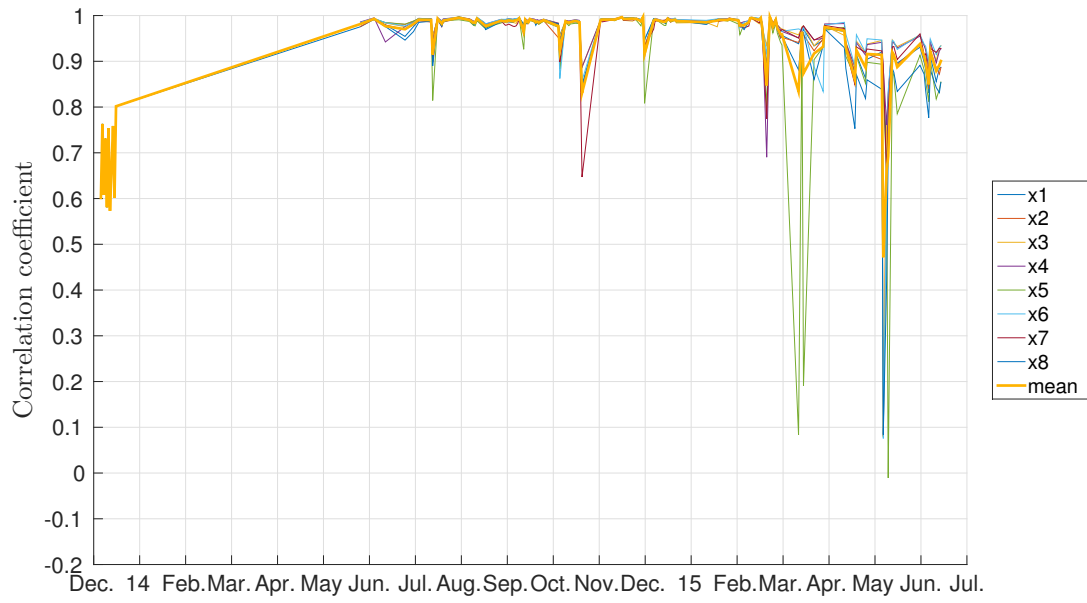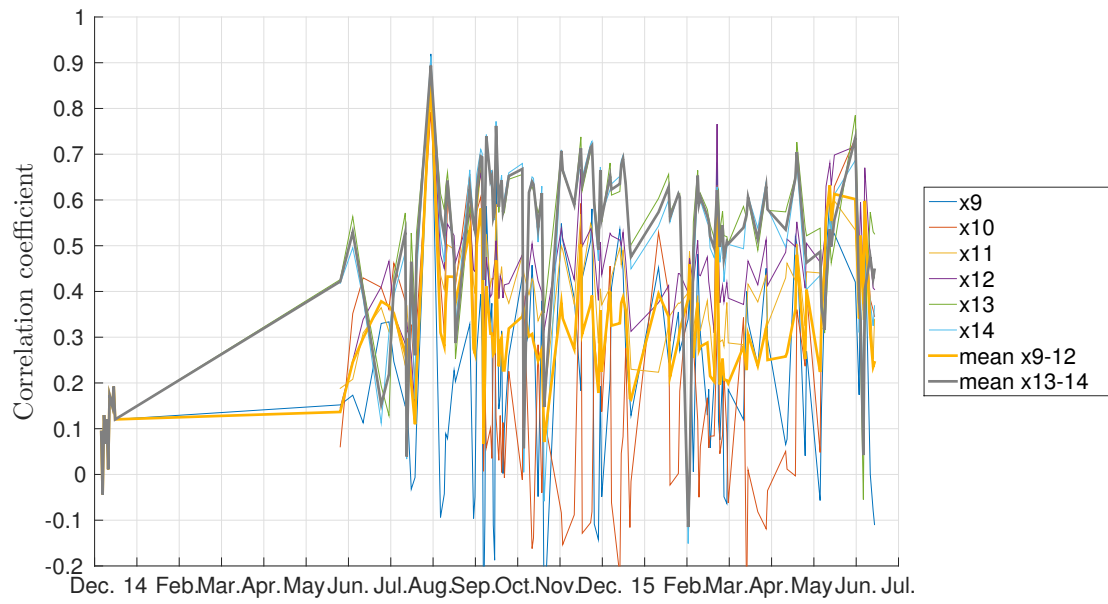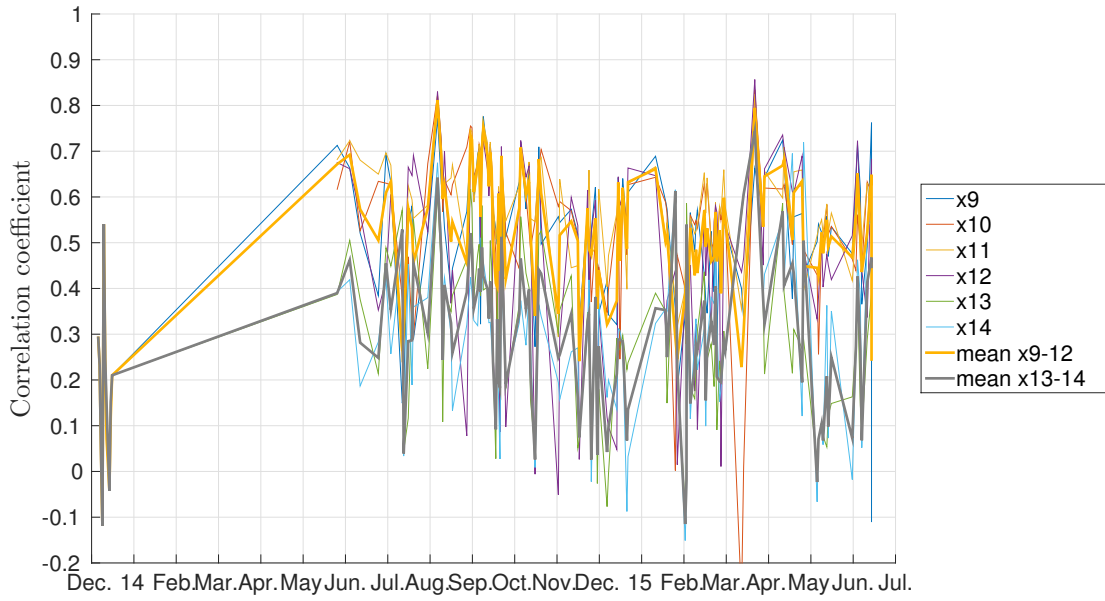
(a) X-band

(b) S-band

Fig. B.2: Katherine, time series of the correlation coefficient (X-band and S-band)
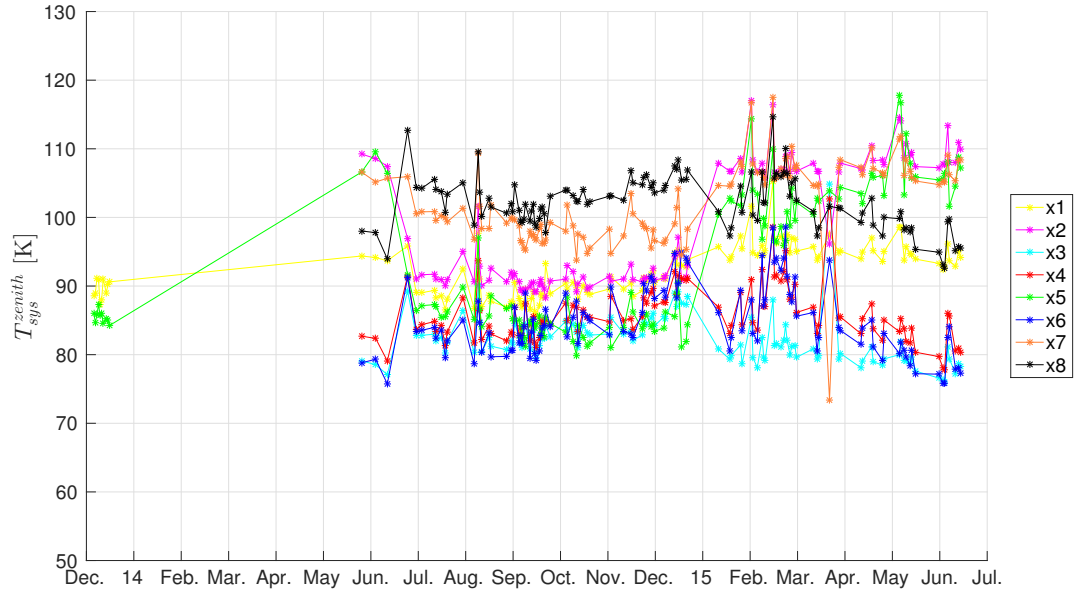
(a) X-band

(b) S-band

**Fig. B.3:** Katherine, time series of the correlation coefficient (X-band and S-band)

C   System temperature in zenith direction - time series

The channels which are plotted in this Fig., show a jump after session aust74. In comparison to the channels which are shown in fig. C.1, the channels in this fig. don't show a jump.

They started decreasing in Feb. 2015. One might interpret a yearly signal. A slight decrease of T_{sys} can be found for Hobart's S-band. Again channels x13 and x14 are separated with lower T_{sys}, but fig. B.3b show that approximately 50% of scans per session are lost because they are not in the range of 0 to 200 K. The yearly signal mentioned in fig. C.1 is much more present in Katherine's X-band. In contrast to Hobart's S-band, Katherine's S-band shows separated channels x13 and x14 as well, but without eliminating a high number of scans (less than 5%). Again, one might interpret a yearly signal. This time series of the X-band of Yarragadee doesn't show any time depend signals. The T_{sys} is stable. There is only a higher scatter (mainly due to x6) during a14 and a15, which can also be seen in the correlation coefficients of Yarragadee for a15. The channels of the S-band of Yarragadee all are pretty separated. Any yearly signal or decrease of T_{sys}^{zenith} can not be found, but a lot of peaks for each channel.
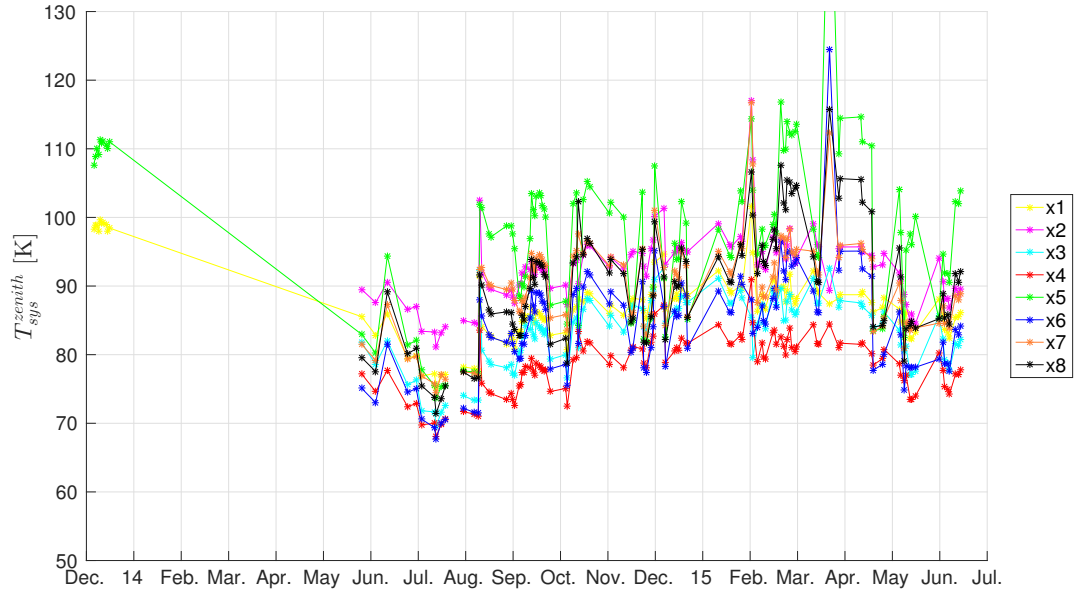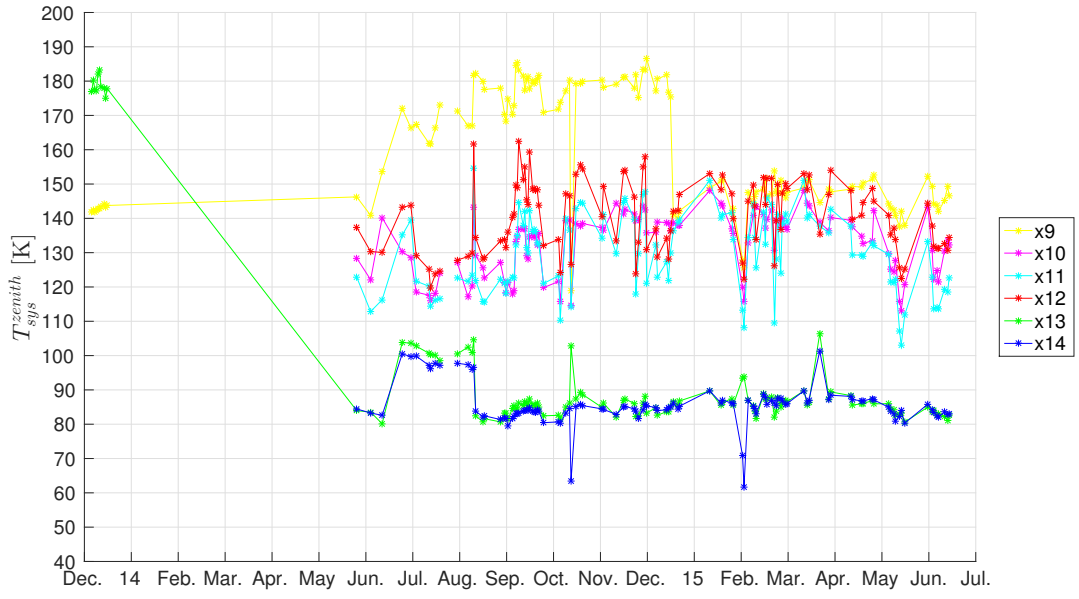
(a) Hobart time series of T_{sys}^{zenith} X-band
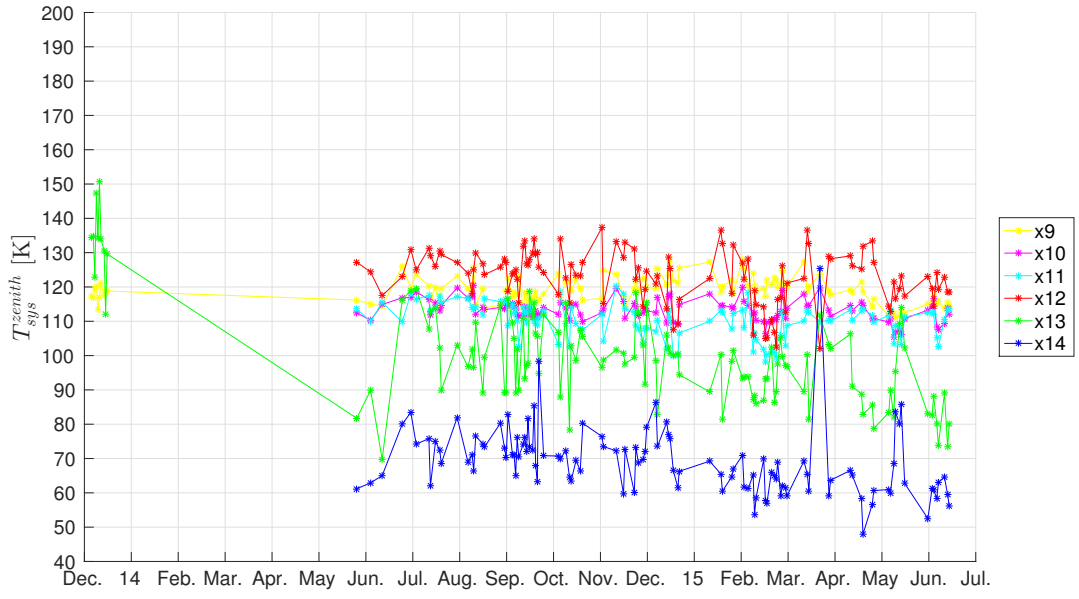
(b) Hobart time series of T_{sys}^{zenith} S-band

Fig. C.1: Hobart time series of T_{sys}^{zenith} (X-band and S-band)
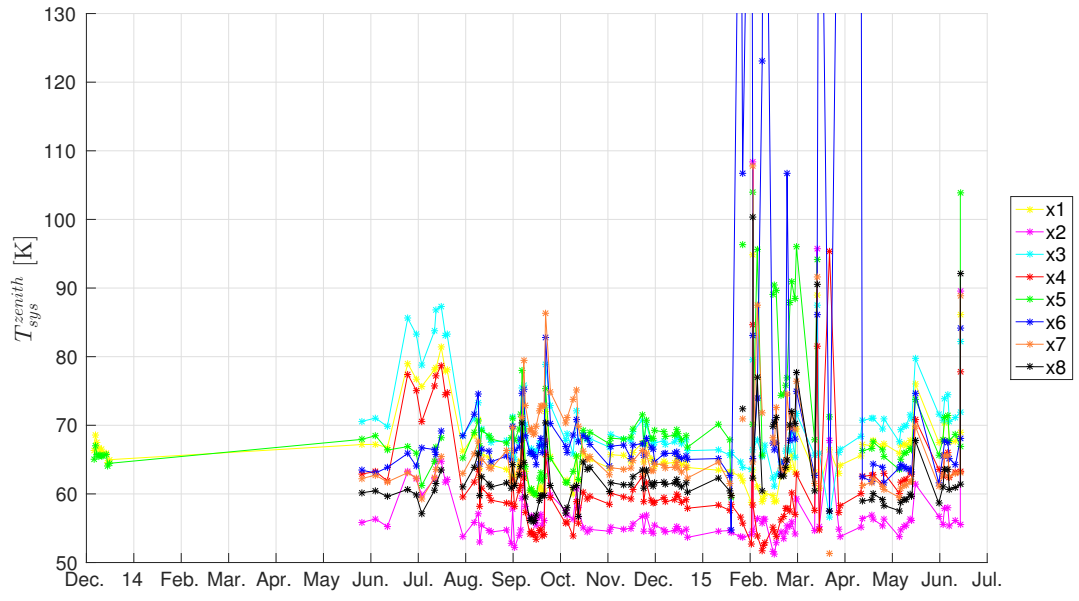
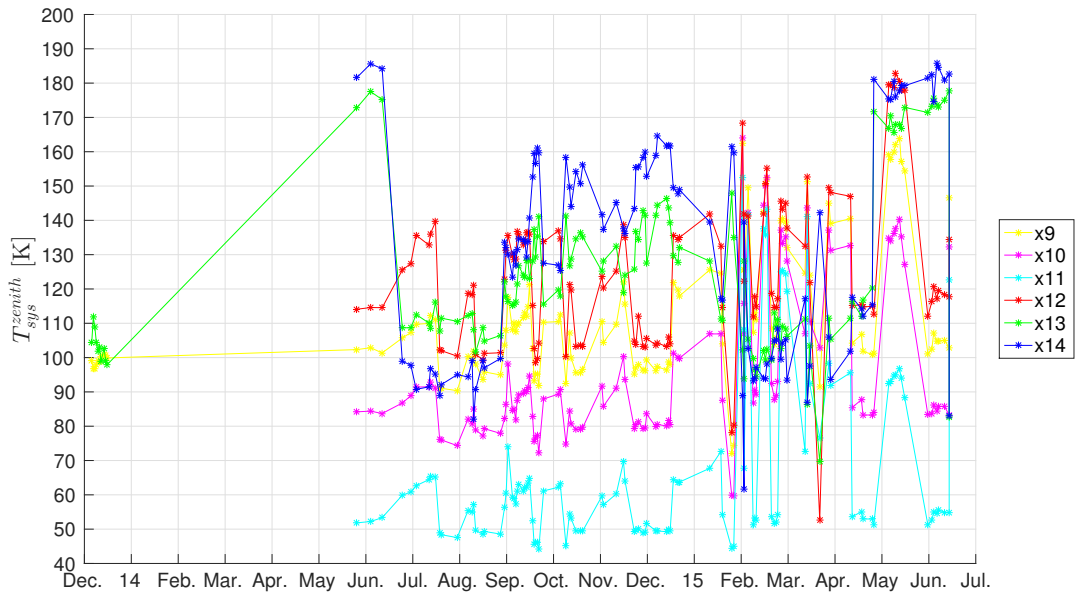**(a)** Katherine time series of T_{sys}^{zenith} X-band

(b) Katherine time series of T_{sys}^{zenith} S-band

Fig. C.2: Katherine time series of T_{sys}^{zenith} (X-band and S-band)

(a) Yarragadee time series of T_{sys}^{zenith} X-band

(b) Yarragadee time series of T_{sys}^{zenith} S-band

Fig. C.3: Yarragadee time series of T_{sys}^{zenith} (X-band and S-band)
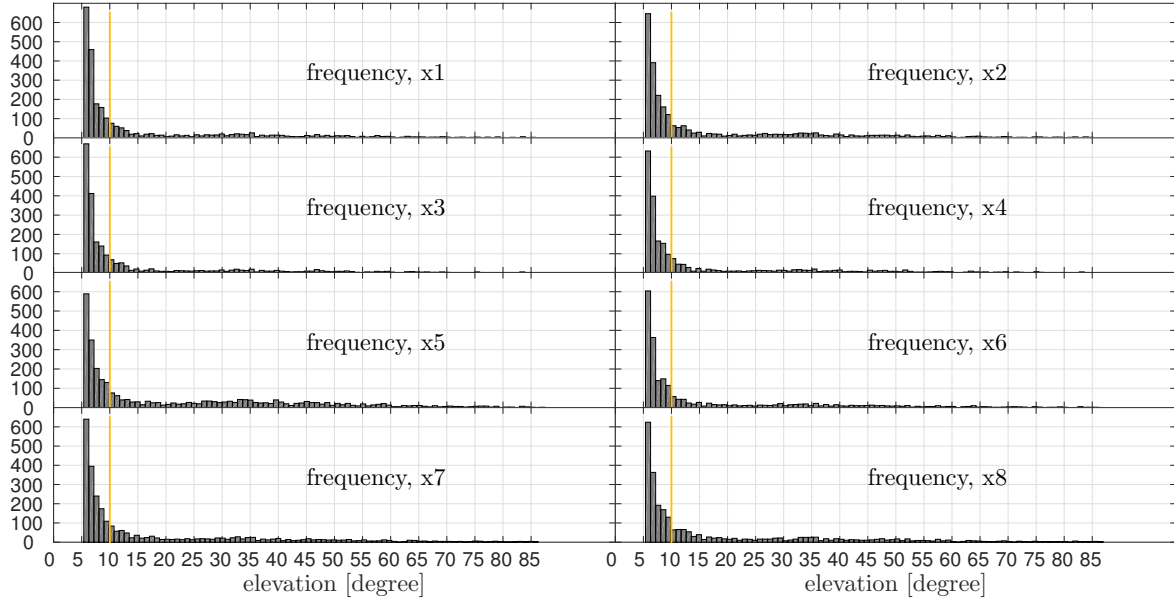
D   Histogram of residuals larger than 2σ

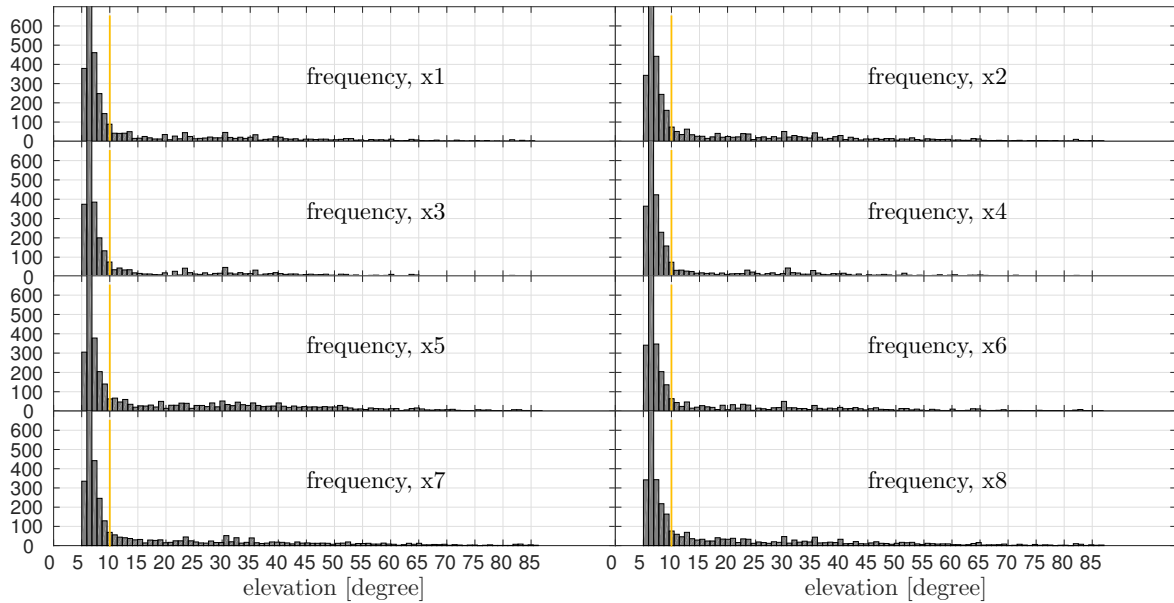**Fig. D.1:** Hobart X-band: Histogram of residuals larger than 2σ.

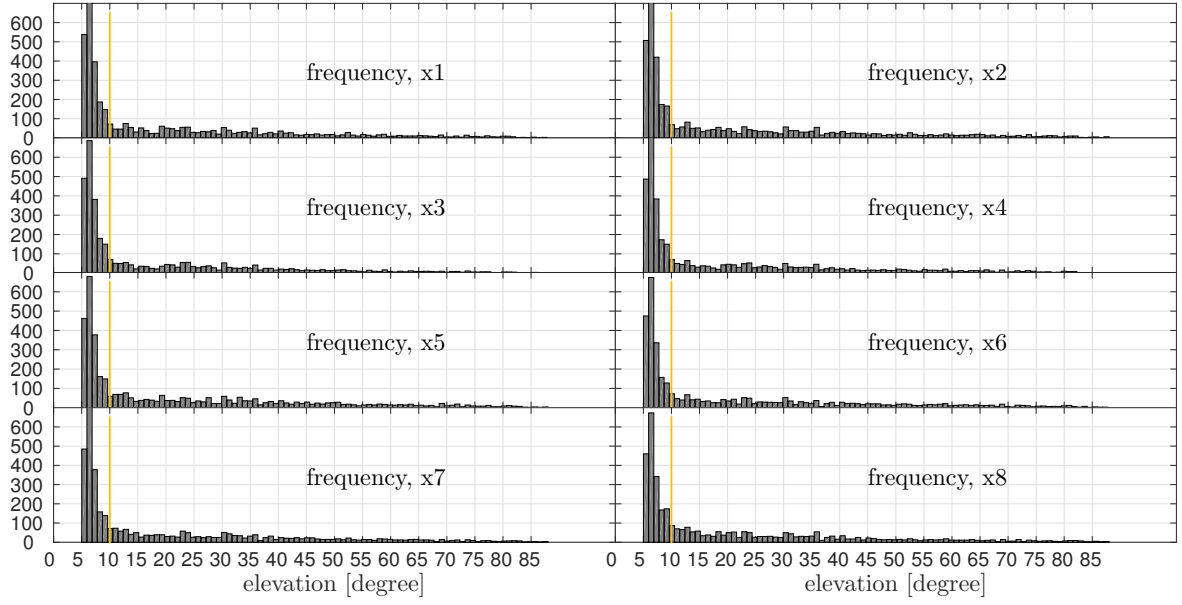**Fig. D.2:** Katherine X-band: Histogram of residuals larger than 2σ.

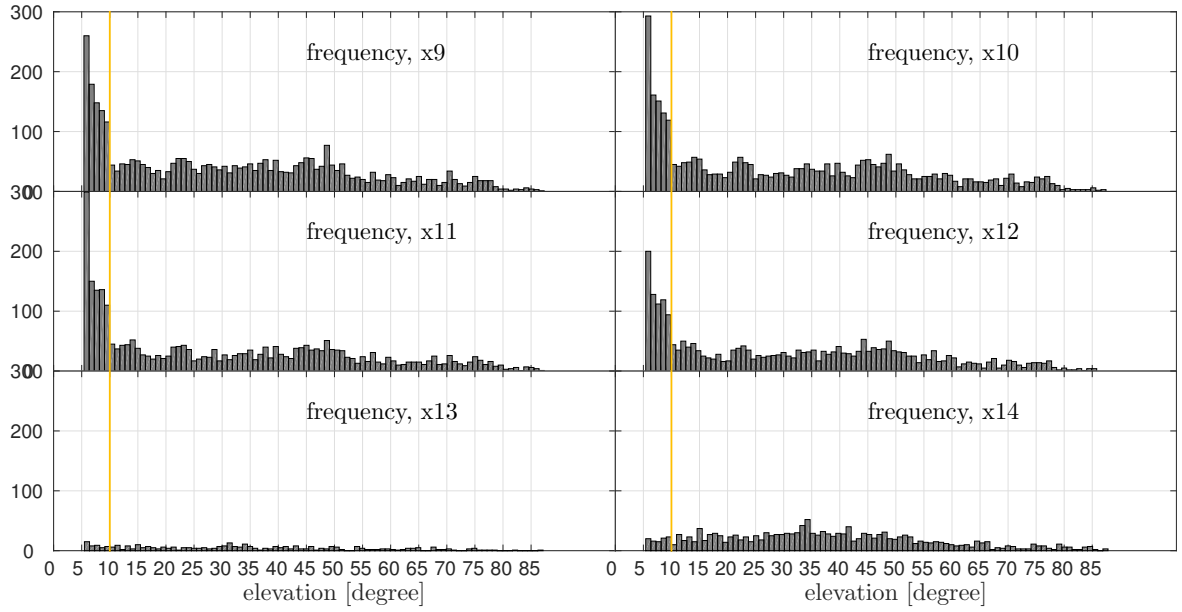**Fig. D.3:** Yarragadee X-band: Histogram of residuals larger than 2σ.

Fig. D.4: Hobart S-band: Histogram of residuals larger than 2σ. The low number of resiudals larger than 2σ for channel x13 and x14 is due to the low number of observations, because a very high number of T_{sys} are outliers.
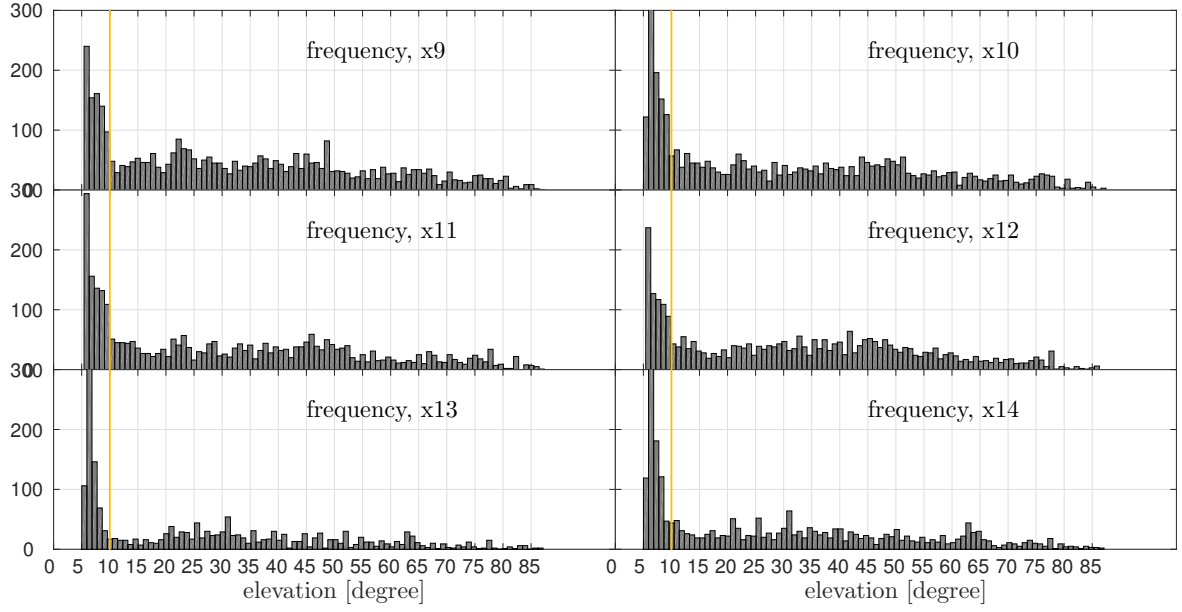
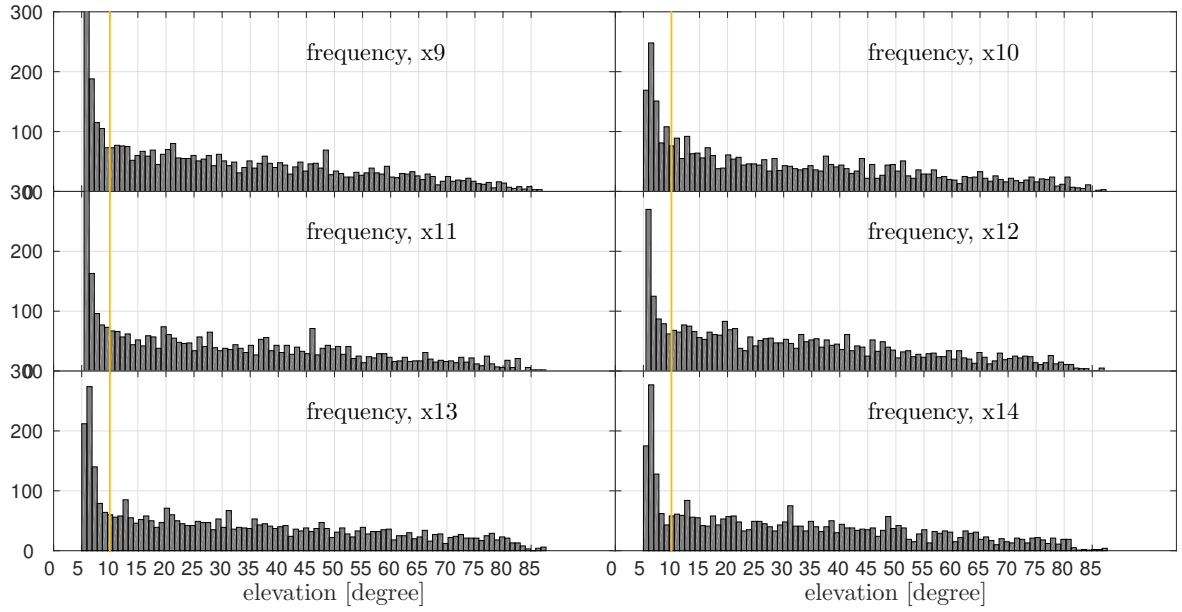**Fig. D.5:** Katherine S-band: Histogram of residuals larger than 2σ

Fig. D.6: Yarragadee S-band: Histogram of residuals larger than 2σ.

E Average system temperature in zenith direction estimated over all sessions

This section provides an overview of the T_{sys}^{zenith} for the stations Hobart (Fig. E.1), Katherine (Fig. E.2) and Yarragadee (Fig. E.3) for each channel. These values are an simple average value of all available T_{sys}^{zenith} values of each stations.
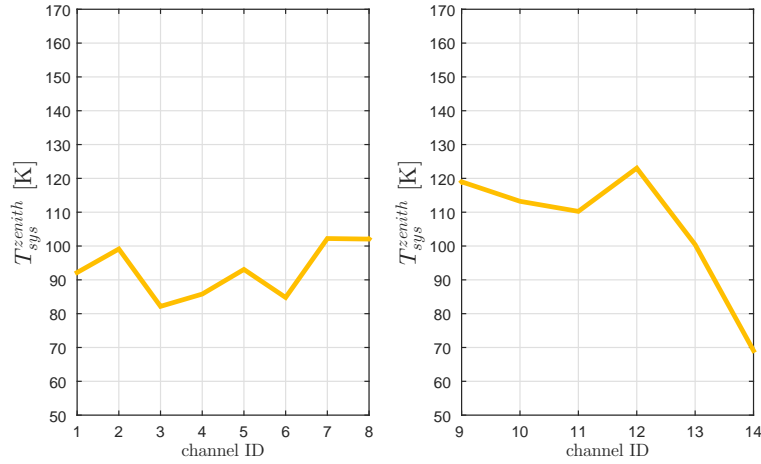

Fig. E.1: Hobart: Due to the high loss of scans in the channels x13 and x14, the estimated T_{sys}^{zenith} for these channels is not representative. Channels x1 to x8 show a similar mean T_{sys}^{zenith} and they are scattered around 95 K. Neglecting the channels x13 and x14, the mean of channels x9 to x12 is about 115 K
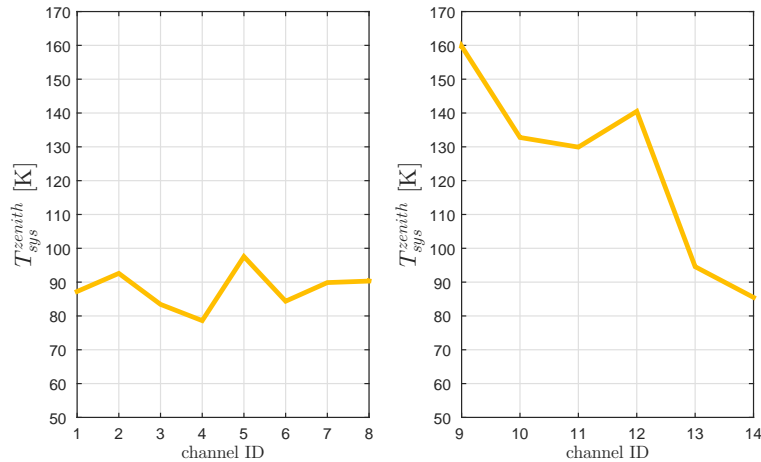

Fig. E.2: Katherine: The X-band is similar to Hobart's X-band (T_{sys}^{zenith} is around 95 K). Channels x9 to x12 are elevated (T_{sys}^{zenith} is around 145 K). Channels x13 and x14 are in the same range than the X-band channels.
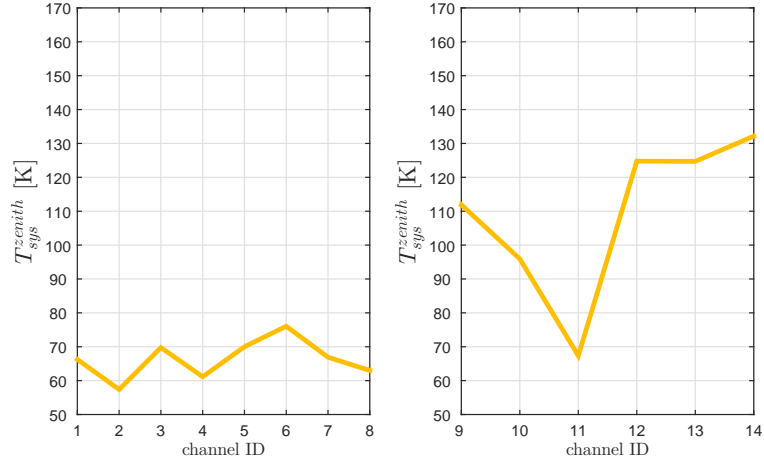
Fig. E.3: Yarragadee: Yarragadee's X-band and channel x11 lies around 65 K. The S-band is elevated (around 110 K) with x11.

F   Average b per channel estimated over all sessions

The elevation dependency of the T_{sys} doesn't show a big difference between the channels.
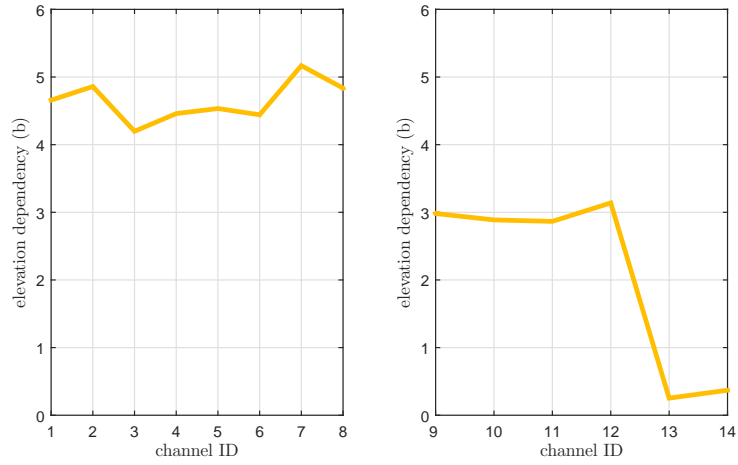

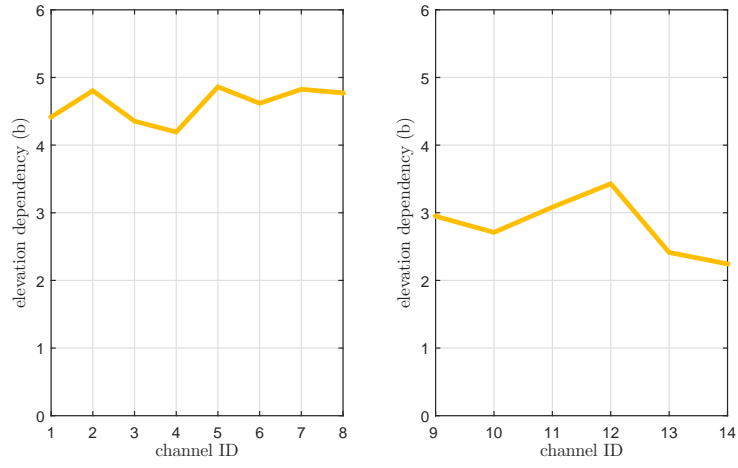**Fig. F.1:** Hobart: mean elevation dependency of each channel.

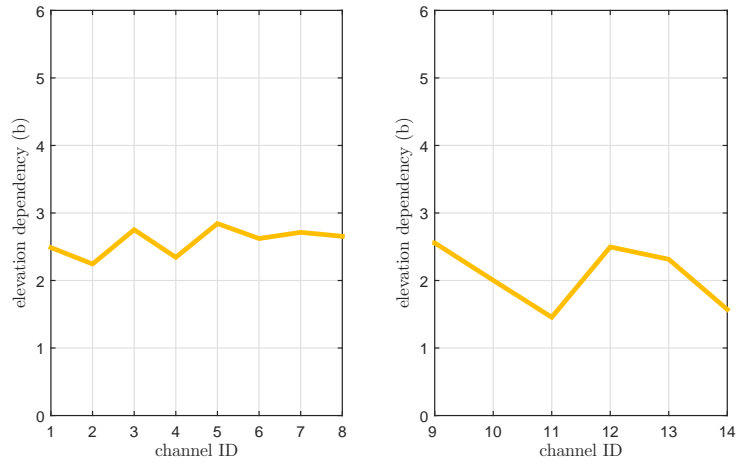**Fig. F.2:** Katherine: mean elevation dependency of each channel.

Fig. F.3: Yarragadee: mean elevation dependency of each channel.

References

Australian earth infrastructure programm (2007). URL: `http://www.auscope.org.au/`, accessed 30.12.2015.

Balser, D. S., Bignell, C., Braatz, J., Clark, M., Condon, J., Harnett, J., O'Neil, K., Maddalena, R., Marganian, P., McCarty, M., Sessoms, E., & Shelton, A. (2009): GBT Dynamic Scheduling System: Algorithms, Metrics, and Simulations. Astronomical Data Analysis Software and Systems XVIII. ASP Conference Series, Vol. 411, 2009.

Böhm, J., Böhm, S., Nilsson, T., Pany, A., Plank, L., Spicakova, H., Teke, K. and Schuh, H. (2012). The new Vienna VLBI Software VieVS. In Proceedings of the 2009 IAG Symposium, Buenos Aires, Argentina, Vol. 136, International Association of Geodesy Symposia, 31 August - 4 September 2009.

Cannon W. (1999): Overview of VLBI. In: Vandenberg, N., Baver, K. (Eds.), International VLBI Service for Geodesy and Astrometry 1999 Annual Report. NASA/TP-1999-209243. pp. 13–17.

Chandrasekhar S. (1960): Radiative Transfer. Dover Publications Inc. p. 393. ISBN 0-486-60590-6.

Crane, P., Napier, P. (1988): Sensitivity. Astronomical Society of the Pacific Conference Series.

Feldman, N. E. (1964): Estimates of communication satellite system degreadation due to rain. Rand Corp., p. 15 (October 1964).

Gipson, J. (2012): Sked. VLBI Scheduling Software. NASA Goddard Spaceflight Center.

Gipson, J. (2013): Scheduling a VLBI Session. NVI,INC/NASA GSFC. 7th IVS TOW Meeting. Haystack, MA. May, 2013.

Grypstra, K. and Keller, R. (2009): The frequency coverage and RFI observations at Effelsberg. Max-Planck-Institut für Radioastronomie, Wettzell, March 18-20, 2009.

Ilin, G. (2008): Radio frequency interference at QUASAR Network Observatories. EVGA Meeting, Bonn 2011.

IEEE (1984). frequency letter bands. URL: `http://www.microwaves101.com/encyclopedias/frequency-letter-bands`, accessed 15.10.2015.

IVS (2016). International VLBI Service. URL: `http://ivscc.gsfc.nasa.gov/`, accessed 14.01.2016.

Langley, R.B. (1997): GPS Receiver System Noise. GPS World.

Lopez-Perez, J. A. (2010): Detected Interferences at S-band from the 40-m Radiotelescope Servo Systems, Observatorio de Yebes, Instituto Geografico Nacional, Spain, VLBI 2010/FRFF2009.

Lovell, J. E J, McCallum, J. N., Reid, P. B., McCulloch, P. M., Baynes, B. E., Dickey, J. M., Shabala, S. S., Watson, C. S., Titov, O., Ruddick, R., Twilley, R., Reynolds, C., Tingay, S. J., Shield, P., Adada, R., Ellingsen, S. P., Morgan, J. S., Bignall, H. E. (2013): The AuScope geodetic VLBI array. Journal of Geodesy. Vol. 87. Pages 527-538.

Lovell, J. E J, McCallum, J. N., Plank, L., Böhm, J., Sun, J., Mayer, D. (2014): Dynamic Observing in the VGOS Era. Proceedings of the 8th IVS General Meeting. August 2014. Beijing, China.

Lovell, J. E J, Shabala, S. S., McCallum, J. N., Dickey, J. M., Plank, L., Reynolds, C., Gulyaev, S., Natusch, T., Weston, S., Quick, J., Böhm, J., Sun, J., Titov, O., Lovell, P., Lovell, S. (2014): Southern Hemisphere Geodesy ans Astrometry with AUSTRAL. Proceedings of the 8th IVS General Meeting. August 2014. Beijing, China.

Lovell, J. E J (2015). AuScope VLBI Operations Wiki. URL: `http://auscope.phys.utas.edu.au/opswiki`, accessed 11.10.2015.

Ma, C., Arias, E.F., Bianco, G., Boboltz, D.A., Bolotin, S.L., Charlot, P., Engelhardt, G., Fey, A.L., Gaume, R.A., Gontier, A.-M., Heinkelmann, R., Jacobs, C.S., Kurdubov, S., Lambert, S.B., Malkin, Z.M., Nothnagel, A., Petrov, L., Skurikhina, E., Sokolova, J.R., Souchay, J., Sovers, O.J., Tesmer, V., Titov, O.A., Wang, G., Zharov, V.E., Barache, C., Boeckmann, S., Collioud, A., Gipson, J.M., Gordon, D., Lytvyn, S.O., MacMillan, D.S., Ojha, R. (2009): The Second Realization of the International Celestial Reference Frame by Very Long Baseline Interferometry. IERS Tech. Note 35.

Marr J. M., Snell R. L., Kurtz S. E. (2015): Fundamentals of Radio Astronomy, Series in Astronomy and Astrophysics, 2015.

Mayer, D., Böhm, J., Lovell, J., Plank, L., Sun, J., Titov, O. (2015): Scheduling Strategies for the AuScope VLBI network. Austrian contribution to he XXBVI General Assembly of the International Union of Geodesy and Geophysics (IUGG). June 22-July 2, 2015, Prague, Czech Republic.

Millenaar, R. P. & Stiepel H. J. (2003): On self-generated RFI at Radio Astronomy Sites, Committee on Radio Astronomy frequencies, CRAF-04-1 , 2003.

Niell, A., Whitney, A., Petrachenko, B., Schlüter, W., Vandenberg, N., Hase, H., Koyama, Y., Ma, C., Schuh, H., Tuccari, G. (2006): VLBI2010: Current and future requirements for geodetic VLBI systems. In: Behrend D, Karen B (eds) International VLBI Service for Geodesy and Astrometry 2005 Annual Report, NASA/TP-2006-214136:13–40.

Nyquist H. (1928): Thermal Agitation of Electric Charge in Conductors, Phys. Rev. 32, 110, 1928.

Pany A, Böhm J, MacMillan DS, Schuh H, Nilsson T, Wresnik J (2010): Monte Carlo simulations of the impact of troposphere, clock and measurement errors on the repeatability of VLBI positions. J Geod 85:1:39–50.

Penzias, A., Wilson, R. (1965): A measurement of excess antenna temperature at 4080 Mc/s. The Astrophysical Journal, Volume 142.

Petrachenko, B. (2009): Broadband Delay Tutorial. FRFF workshop, Wettzell, Germany, March 18, 2009.

Petrachenko, B., Niell, A., Behrend, D., Corey, B., Boehm, J., Charlot, P., Collioud, A., Gipson, J., Haas, R., Hobiger, T., Koyama, Y., MacMillan, D., Malkin, Z., Nilsson, T., Pany, A., Tuccari, G., Whitney, A., Wresnik, J. (2009): Design Aspects of the VLBI2010 System. Progress Report of the IVS VLBI2010 Committee, June 2009., Tech. rep.

Petrachenko, B. (2013): Radio Antennas, Feed Horn and Front-End Receivers. EGU und IVS Training School on VLBI for Geodesy and Astrometry. March 2-5, 2013. Aalto University, Espoo, Finland.

Plag, H.-P., Pearlman, M., (2009): Global Geodetic Observing System: Meeting the Requirements of a Global Society on a Changing Planet in 2020. Springer- Verlag, Berlin, Heidelberg, ISBN: 978-3-642-02686-7, 332 pp.

Plank, L., Lovell, J. E J, McCallum, J., Rastorgueva-Foi, E., Shabala, S., Böhm, J., Mayer, D., Sun, J., Titov, O., Weston, S., Gulyaev, S., Natusch, T., Quick, J. (2015). Results from the Regional AUSTRAL VLBI Sessions for Southern Hemisphere Reference Frames. In: Proceedings of the IAG Commission 1 Symposium 2014: Reference Frames for Applications in Geosciences (REFAG2014) 13-17 October 2014, Kirchberg, Luxembourg.

Porcas, R. (2010): VLBI2010: The Astro-Geo Connection, IVS 2010 General Meeting Proceedings, p. 8–17.

Schuh H, Behrend D (2012): VLBI: A fascinating technique for geodesy and astrometry. J of Geodynamics 61:68–80.

Shabala, S., Rogers, J., McCallum, J., Titov, O., Blanchard, J., Lovell, J., Watson C. (2014): The effect of frequency-dependent quasar variability on the celestial reference frame. Journal of Geodesy (2014). 88:575–586. DOI 10.1007/s00190-014-0706-z.

Sun, J. (2012): VLBI scheduling strategies with respect to VLBI2010. Vienna University of Technology.

Schlüter, W., Behrend, D. (2007): The international VLBI service for geodesy and astrometry (IVS): current capabilities and future prospects. J Geodyn 81(6-8):379–387. doi:10.1007/ s00190-006-0131-z.

Taylor, G., Carilli, C., & Perely, R. (1999): Synthesis Imaging in Radio Astronomy II. A collection of Lectures from the Sixth NRAO/NMIMT Synthesis Imaging Summer School. Held in Socorro NM 1998 June 17-23.

Wilson, T.L., Rohlfs, K., & Hüttenmeister, S. (2009): Tools of Radio Astronomy. Springer-Verlag, Berlin, Heidelberg.